

ENERGY BASED SEISMIC ASSESSMENT AND DESIGN

A THESIS SUBMITTED TO
THE GRADUATE SCHOOL OF NATURAL AND APPLIED SCIENCES
OF
MIDDLE EAST TECHNICAL UNIVERSITY

BY

FIRAT SONER ALICI

IN PARTIAL FULFILLMENT OF THE REQUIREMENTS
FOR
THE DEGREE OF DOCTOR OF PHILOSOPHY
IN
CIVIL ENGINEERING

FEBRUARY 2019

Approval of the thesis:

ENERGY BASED SEISMIC ASSESSMENT AND DESIGN

submitted by **FIRAT SONER ALICI** in partial fulfillment of the requirements for the degree of **Doctor of Philosophy in Civil Engineering Department, Middle East Technical University** by,

Prof. Dr. Halil Kalıpçılar
Dean, Graduate School of **Natural and Applied Sciences**

Prof. Dr. Ahmet Türer
Head of Department, **Civil Engineering**

Prof. Dr. Haluk Sucuoğlu
Supervisor, **Civil Engineering, METU**

Prof. Dr. Murat Altuğ Erberik
Co-Supervisor, **Civil Engineering, METU**

Examining Committee Members:

Prof. Dr. Polat Gülkan
Department of Architecture, Bilkent University

Prof. Dr. Haluk Sucuoğlu
Civil Engineering, METU

Prof. Dr. Murat Dicleli
Department of Engineering Sciences, METU

Prof. Dr. Dede Sinan Akkar
Kandilli Earthquake Eng. Research Institute, Boğaziçi University

Prof. Dr. Ayşegül Askan Gündoğan
Civil Engineering, METU

Date: 07.02.2019

I hereby declare that all information in this document has been obtained and presented in accordance with academic rules and ethical conduct. I also declare that, as required by these rules and conduct, I have fully cited and referenced all material and results that are not original to this work.

Name, Surname: Firat Soner Alici

Signature:

ABSTRACT

ENERGY BASED SEISMIC ASSESSMENT AND DESIGN

Alici, Firat Soner
Doctor of Philosophy, Civil Engineering
Supervisor: Prof. Dr. Haluk Sucuođlu
Co-Supervisor: Prof. Dr. Murat Altuđ Erberik

February 2019, 143 pages

The need to improve the reliability of current earthquake resistant design procedures has promoted energy-based concepts that employ seismic input energy and energy dissipation capacity of structures as the main design tools. Energy based approaches provide effective tools at both design and assessment stages for a comprehensive interpretation of the seismic behavior of structural systems during an earthquake excitation. Energy based assessment and design procedure includes two crucial aspects. The first one is the prediction of input energy spectra, considering both the structural and ground motion related parameters. The second concern is the evaluation of the actual energy absorption and dissipation capacity of structural systems during seismic response. In this regard, the aim of this study is first to introduce a procedure for the prediction of earthquake input energy spectra considering the effects of structural properties (damping ratio ξ and lateral strength ratio R_μ) and ground motion characteristics (moment magnitude M_w , soil type S , fault type F , distance to fault R). Furthermore, the effects of inelastic behavior and near-fault ground motions on input energy are also considered, and presented in this study. Then the energy dissipation characteristics of SDOF and MDOF systems are studied, respectively. In this sense, the relation between input energy and dissipated energy is obtained, and sensitivity of energy dissipation efficiency of SDOF systems is assessed. In this scope, two different

$R_{\mu-\xi-T}$ spectra, as an improvement to equal displacement rule, are derived for estimating the maximum displacement of inelastic SDOF systems from the maximum displacement of equivalent linear SDOF systems. In the application stage, the predicted input energy and displacement spectra are integrated to attain the energy dissipation mechanisms of MDOF systems. Accordingly, it is aimed that a sufficient number of plastic hinges required to dissipate the imparted energy are detected from response spectrum analysis, by using the modal energy formulation of MDOF systems and estimated modal inelastic displacements. Thus, it is ensured that unlike the capacity design in which all beam-column connections are designated and designed as potential plastic hinge locations, a limited number of plastic hinges at the predefined locations can dissipate the imparted energy during seismic response efficiently. Based on the obtained results in this study, the suggested method improves the capacity based seismic design procedures in improving the seismic performance of structural systems.

Keywords: Energy Based Design, Seismic Input Energy, Input Energy Prediction, Seismic Energy Dissipation, Equivalent Damping Ratio, Damping Spectra

ÖZ

ENERJİ ESASLI SİSMİK DEĞERLENDİRME VE TASARIM

Alicı, Fırat Soner
Doktora, İnşaat Mühendisliği
Tez Danışmanı: Prof. Dr. Haluk Sucuoğlu
Ortak Tez Danışmanı: Prof. Dr. Murat Altuğ Erberik

Şubat 2019, 143 sayfa

Günümüz depreme dayanıklı tasarım yöntemlerinin güvenilirliğini geliştirme ihtiyacı, deprem sırasında yapı sistemine yüklenen sismik enerji ve yapının bu enerjiyi sönmüleme kapasitesine dayanan “enerji esaslı deprem tasarımı” kavramının ortaya çıkmasına sebep olmuştur. Enerji esaslı yaklaşımlar, deprem etkisi altındaki yapıların davranışlarının kapsamlı olarak yorumlanması için hem tasarım, hem de değerlendirme aşamasında etkili araçlar sağlamaktadır. Enerji esaslı tasarım yöntemi iki önemli temel hususu içermektedir. Bunlardan ilki hem yapısal hem de yer hareketi ile ilgili parametreleri göz önünde bulundurarak sismik enerji spektrumlarının tahminidir. İkinci konu ise sismik davranış sırasında yapısal sistemlerin gerçek enerji soğurma ve dağıtma kapasitelerinin değerlendirilmesidir. Bu bağlamda, bu çalışmanın amacı ilk olarak yapısal özelliklerin (sönüm oranı ξ , ve dayanım azaltma katsayısı R_μ) ve yer hareketi özelliklerinin (moment büyüklüğü M_w , zemin tipi S, fay tipi F ve faya olan uzaklık R) etkilerini dikkate alarak sismik enerji spektrumlarının tahminine yönelik bir prosedürün ortaya konulmasını kapsamaktadır. Bu parametrelere ek olarak elastik ötesi davranışın ve faya yakın yer hareketlerinin sismik enerji üzerindeki etkileri de incelenmiş ve bu çalışmada detaylı bir şekilde yer verilmiştir. İkinci olarak, sırasıyla tek dereceli ve çok dereceli sistemlerin enerji dağıtım özelliklerinin irdelenmesine yer verilecektir. Bu amaçla, toplam yüklenen sismik enerji ve dağıtılan

enerji arasındaki ilişki elde edilmiş ve tek dereceli sistemlerin enerji dağıtım verimliliğinin duyarlılığını etkileyen parametrelere bakılmıştır. Daha sonra, tek dereceli inelastik sistemlerin maksimum yer değiştirme taleplerini tahmin etmek için eşit yer değiştirme kurulana göre daha iyi sonuçlar ortaya koyan iki farklı $R_{\mu}-\xi-T$ spektrumu türetilmiştir. Uygulama aşamasında, tahmin edilen sismik enerji ve yer değiştirme spektrumları birbirlerine entegreli olarak çok dereceli sistemlerin enerji dağıtım mekanizmalarının ortaya çıkartılmasında kullanılmıştır. Buna uygun olarak sisteme yüklenen enerjinin dağıtılması için yeterli sayıda plastik mafsalın, çok dereceli sistemlerin modal enerji formülasyonu ve tahmini modal elastik yer değiştirme spektrumu kullanılarak tespit edilmesi amaçlanmıştır. Böylece tüm kiriş-kolon birleşim yerlerinin potansiyel plastik mafsal yerleri olarak tasarlandığı kapasite tasarımından farklı olarak, sismik davranış sırasında sisteme yüklenen enerjinin önceden tanımlanmış bölgelerde belirli sayıdaki plastik mafsal ile verimli bir şekilde dağıtılması sağlanmış olacaktır. Bu çalışmadan elde edilen sonuçlar, bu yöntemin yapısal sistemlerin sismik performansının iyileştirilmesinde kapasite esaslı sismik tasarım yaklaşımlarına önemli bir iyileştirme sağladığını ortaya koymaktadır.

Anahtar Kelimeler: Enerji Esaslı Tasarım, Sismik Enerji, Sismik Enerji Tahmini, Sismik Enerji Dağıtımı, Eşdeğer Sönümlenme Oranı, Sönümlenme Spektrumu

Dedicated to my wife and to my father

ACKNOWLEDGMENTS

I would like to express my sincere gratitude to my advisor Prof. Dr. Haluk Sucuođlu for the continuous support of my Ph.D. study and related research, for his patience, motivation and immense knowledge. His guidance helped me in all the time of research and writing of this thesis. I could not have imagined having a better advisor and mentor for my Ph.D. thesis. I also want to thank my co-advisor Prof. Dr. Murat Altuđ Erberik for his continuous support and sound advices.

Besides my advisor and co-advisor, I would like to thank the rest of my thesis committee: Prof. Dr. Polat Gůlkan, Prof. Dr. Murat Dicleli, Prof. Dr. Sinan Akkar, and Prof. Dr. Ayşegůl Askan Gůndođan for their insightful comments and encouragement.

My special thanks go to my beloved wife Nilgůn for her positive support and endless patience, and for helping me get through difficult times. Her endless courage and conviction will always inspire me.

I would like to thank sincerely my father and my beloved family. Their constant love and supports are great encouragement in all my life. Their support and patience are thankfully acknowledged.

I would like to thank my colleague Kaan Kaatsız for his friendship and support. I will always remember with pleasure. I would like also to thank my friends Gůkhan Atay and Murat Pazarbaş for their friendship and support.

I also want to thank TŐBŐTAK for providing scholarship support during my thesis study. The support of TŐBŐTAK to science and scientists is respectable and admirable.

TABLE OF CONTENTS

ABSTRACT	v
ÖZ	vii
ACKNOWLEDGMENTS	x
TABLE OF CONTENTS	xi
LIST OF TABLES	xiv
LIST OF FIGURES	xvi
1. INTRODUCTION	1
1.1. Problem Statement	1
1.2. Objective and Scope	2
2. REVIEW OF PAST STUDIES.....	5
2.1. Concept of Energy in Seismic Design, and Prediction of Input Energy	5
2.2. Near-Fault Effects On Elastic and Inelastic Input Energy Spectra	8
3. PREDICTION OF ELASTIC INPUT ENERGY SPECTRUM.....	13
3.1. Strong Ground Motion Database.....	14
3.2. Elastic Input Energy	21
3.3. Input Energy Prediction by Prediction Equations	22
3.4. Input Energy Prediction By Developing Scaling Relations Between PS_V and V_{eq}	36
4. ELASTIC AND INELASTIC NEAR-FAULT INPUT ENERGY SPECTRA ..	47
4.1. Near-Fault Ground Motions	47
4.2. Near-Fault Prediction Model for Elastic and Inelastic Input Energy	52
4.3. Near-Fault Elastic Input Energy Prediction	58

4.4. The Effect of Damping on Near-Fault Elastic and Inelastic Input Energy Spectra	63
4.5. The Effect of Lateral Strength Ratio on Near-Fault Inelastic Input Energy Spectra.....	65
5. EQUIVALENT DAMPING SPECTRA FOR EQUAL DISPLACEMENT	73
5.1. Concept of Equal Displacement Rule	73
5.2. Damping Efficiency	76
5.2.1. Strong Ground Motions.....	78
5.2.2. Earthquake Magnitude	78
5.2.3. Fault Distance.....	79
5.2.4. Fault Type.....	79
5.2.5. Soil Type	80
5.2.6. Remarks on Damping Efficiency	81
5.2.7. Classification of Strong Ground Motions	81
5.3. Computation of $R_{\mu-\zeta}-T$ Spectra	82
5.3.1. $R_{\mu-\zeta}-T$ Spectra for Equal Displacement Rule.....	83
5.3.2. $R_{\mu-\zeta}-T$ Spectra for Equivalent Linearization with Period Shift	86
5.4. Comparative Evaluation of Equivalent Linearization Procedures	89
5.5. Implementation of Equivalent Linearization Procedures for the Response Prediction of a 5 Story Frame	93
6. AN ENERGY BASED ASSESSMENT AND DESIGN PROCEDURE	99
6.1. Energy Equations for MDOF Systems.....	99
6.2. Energy Dissipation at the Maximum Displacement Cycle	102
6.3. Energy-Based Seismic Assessment	106
6.3.1. Verification of Energy-Based Seismic Assessment	108

6.4. Energy-Based Seismic Design	118
6.4.1. Implementation of Energy-Based Seismic Design	121
7. SUMMARY AND CONCLUSIONS	129
7.1. Summary	129
7.2. Conclusions	130
REFERENCES.....	133
CURRICULUM VITAE.....	141

LIST OF TABLES

TABLES

Table 3.1. Earthquakes used in the study	16
Table 3.2. Regression coefficients calculated for the prediction model.....	24
Table 3.3. Slope of the best fit lines in the scatter plots of residuals with respect to M and R_{epi}	25
Table 3.4. Coefficients for the model equation of V_{eq}/PS_V versus T for different damping ratios	42
Table 4.1. Distribution of ground motions with respect to V_{S30}	48
Table 4.2. The list of earthquake ground motions	49
Table 4.3. Regression coefficients calculated for linear elastic systems ($R_{\mu}=1$) with $\xi=5\%$	55
Table 4.4. Regression coefficients calculated for yielding systems with $R_{\mu}=2$ and $\xi=5\%$	55
Table 4.5. Regression coefficients calculated for yielding systems with $R_{\mu}=4$ and $\xi=5\%$	56
Table 4.6. Regression coefficients calculated for yielding systems with $R_{\mu}=6$ and $\xi=5\%$	56
Table 5.1. Free vibration properties of the first three modes of five story R/C frame	94
Table 6.1. Modal properties and modal energies of the first three modes.....	110
Table 6.2. Computed $E_{0,j}$ for member-ends j.....	111
Table 6.3. E_j values of plastic hinges at member-ends j.....	112
Table 6.4. Modal properties and modal energies of the first three modes of the modified frame.....	116
Table 6.5. E_j values of plastic hinges at member-ends of the modified frame	116
Table 6.6. Plastic rotations $\theta_{p,j}$ of member ends from RSA under GM46	123
Table 6.7. Plastic rotations $\theta_{p,j}$ of member ends from RSA under GM52	123

Table 6.8. Earthquake design moments obtained from energy-based procedure for GM46 and GM52	124
Table 6.9. Earthquake design moments obtained from force-based design for GM46 and GM52	125

LIST OF FIGURES

FIGURES

Figure 2.1. Different schemes for converting input energy spectra for a linear elastic system to the energy spectra for a yielding system	10
Figure 3.1. Magnitude-distance distribution of ground motions in the study	14
Figure 3.2. Distribution of ground motions with respect to V_{S30}	15
Figure 3.3. Residual plots of observed and estimated V_{eq} spectral values	25
Figure 3.4. Comparison of the computed V_{eq} with the mean and mean \pm one standard deviations of the prediction model for $M_w=7.62$ Chi-Chi (1999) earthquake, for stiff and soft soil types	27
Figure 3.5. Comparison of the computed V_{eq} with the mean and mean \pm one standard deviations of the prediction model for $M_w=7.13$ Hector Mine (1999) and Düzce (1999) earthquakes, for stiff and soft soil types	28
Figure 3.6. Comparison of the computed V_{eq} with the mean and mean \pm one standard deviations of the prediction model for $M_w=6.93$ Loma Prieta (1989) earthquake, for stiff and soft soil types.....	29
Figure 3.7. Comparison of the computed V_{eq} with the mean and mean \pm one standard deviations of the prediction model for $M_w=6.69$ Northridge-01 (1994) earthquake, for stiff and soft soil types.....	30
Figure 3.8. Comparison of the computed V_{eq} with the mean and mean \pm one standard deviations of the prediction model for $M_w=5.99$ Whittier Narrows-01 (1987) earthquake, for stiff and soft soil types.....	31
Figure 3.9. V_{eq} spectra of ground motions selected from Northridge-01 (1994) earthquake and the comparison of their mean spectra with the estimated mean from Equation 3.6.....	32
Figure 3.10. V_{eq} spectra of ground motions selected from Chi-Chi (1999) earthquake and the comparison of their mean spectra with the estimated mean from Equation 3.6	32

Figure 3.11. Comparison of the estimated mean spectra from several studies with the mean spectra of ground motion records selected from the Northridge-01 (1994) earthquake	34
Figure 3.12. Comparison of the estimated mean spectra from several studies with the mean spectra of ground motion records selected from the Chi-Chi (1999) earthquake	35
Figure 3.13. Variation of input energy spectra V_{eq} with earthquake magnitude obtained from the prediction model for different soil types and fault mechanisms at $R_{epi}=20$ km.	36
Figure 3.14. Variation of input energy spectra V_{eq} with epicentral distance obtained from the prediction model for different soil types and fault mechanisms, $M_w=6.5$...	36
Figure 3.15. Variation of input energy spectra V_{eq} with epicentral distance obtained from the prediction model for different soil types and fault mechanisms, $M_w=7.5$...	36
Figure 3.16. Spectral variations of 5 percent damped V_{eq}/PS_V ratio for GM's from Chi-Chi (1999), Hector Mine (1999), Loma Prieta (1989), Northridge-01 (1994) and Whittier Narrows-01 (1987) earthquakes on stiff and soft sites, along with their mean (solid) and mean \pm sigma (dashed) spectra	38
Figure 3.17. Comparison of the mean 5 percent damped V_{eq}/PS_V ratios of ground motions from the selected earthquakes for stiff and soft soil types.	40
Figure 3.18. Comparison of the mean 5 percent damped V_{eq}/PS_V spectra with the mean 2 and 10 percent damped spectra for the ground motions in the database	41
Figure 3.19. Variation of the coefficients of model equation with period for different damping ratios	41
Figure 3.20. (a) Comparison of the estimated mean with the computed mean, and mean \pm sigma V_{eq}/PS_V spectra of all ground motions in the database for 5 percent damping. (b) Comparison of the estimated and computed mean V_{eq}/PS_V spectra for 2, 5 and 10 percent damping	42
Figure 3.21. Comparison of the V_{eq}/PS_V spectra obtained from the 5 percent damped V_{eq}/PS_V spectrum according to EC8 and FEMA440 damping scaling, with the spectra obtained from this study for 2 and 10 percent damping.....	43

Figure 3.22. 5 percent damped design acceleration spectra based on NEHRP provisions, and acceleration spectra of the selected ground motions along with their mean spectrum	44
Figure 3.23. Scaled V_{eq} spectra based on NEHRP design acceleration spectra, and its comparison with the mean spectra of the selected (spectrum compatible) ground motions	45
Figure 4.1. Magnitude - distance distribution of the near-fault ground motions used in this chapter.....	48
Figure 4.2. Residual of observed and estimated V_{eq} values for elastic systems ($R_{\mu}=1$)	57
Figure 4.3. Residuals of observed and estimated V_{eq} values for inelastic systems ($R_{\mu}=4$).....	57
Figure 4.4. Comparison of the computed V_{eq} with the mean and mean \pm one sigma of NF prediction model for $M_w=7.62$ Chi-Chi (1999) earthquake, stiff soil type	59
Figure 4.5. Comparison of the computed V_{eq} with the mean and mean \pm 1 sigma of NF prediction model for $M_w=6.69$ Northridge-01 (1994) earthquake, stiff soil type	59
Figure 4.6. Comparison of the computed V_{eq} with the mean and mean \pm 1 sigma of NF prediction model for $M_w=6.69$ Northridge-01 (1994) earthquake, soft soil type	60
Figure 4.7. Comparison of the computed V_{eq} with the mean and mean \pm 1 sigma of NF prediction model for $M_w=6.53$ Imperial Valley-06 (1979) earthquake, soft soil type	60
Figure 4.8. The comparison of the computed mean elastic V_{eq} spectra of ground motions selected from $M_w=6.69$ Northridge-01 (1994) and $M_w=6.53$ Imperial Valley (1979) earthquakes with the estimated mean spectra from the two prediction equations.....	62
Figure 4.9. Variation of elastic input energy spectra V_{eq} with earthquake magnitude, obtained from NF prediction model for different soil types and fault mechanisms, $R_{epi}=15$ km	62

Figure 4.10. Variation of elastic input energy spectra V_{eq} with epicentral distance, obtained from NF prediction model for different soil types and fault mechanisms, $M_w=6.0$	63
Figure 4.11. Variation of elastic input energy spectra V_{eq} with epicentral distance, obtained from NF prediction model for different soil types and fault mechanisms, $M_w=7.0$	63
Figure 4.12. Comparison of elastic input energy spectra ($R_\mu=1$) of three near fault ground motions for 2, 5 and 10 percent damping ratios	64
Figure 4.13. Comparison of inelastic input energy spectra ($R_\mu=4$) of three near fault ground motions for 2, 5 and 10 percent damping ratios.	64
Figure 4.14. Comparison of input energy spectra of three near fault ground motions for four different R_μ values	65
Figure 4.15. Comparison of the ratios of inelastic energy spectral ordinates ($R_\mu= 2, 4$ and 6) to the elastic energy spectral ordinates ($R_\mu=1$) for the three near fault ground motions.....	66
Figure 4.16. Comparison of the computed inelastic V_{eq} with the mean and mean ± 1 sigma of NF prediction model for $M_w=7.62$ Chi-Chi (1999) earthquake, $R_\mu=4$, stiff soil type.	67
Figure 4.17. Comparison of the computed inelastic V_{eq} with the mean and mean ± 1 sigma of NF prediction model for $M_w=6.53$ Imperial Valley (1979) earthquake, $R_\mu=4$, soft soil type.....	67
Figure 4.18. Inelastic V_{eq} spectra ($R_\mu=4$) of ground motions selected from Chi-Chi (1999), Northridge-01 (1994), Imperial Valley (1979) earthquakes, and the comparison of their mean spectra with the estimated mean spectra from the developed prediction model for $R_\mu=4$ and $R_\mu=1$	68
Figure 4.19. Predicted input energy spectra from the prediction model (Equation 4.2) for reverse faulting and stiff soil condition cases considering $M_w= 6.0$ and 7.0 and $R_{epi} = 10$ km and 20 km	69
Figure 4.20. Ratios of inelastic energy spectral ordinates ($R_\mu=2, 4$ and 6) to the elastic energy spectral ordinates ($R=1$) predicted from the prediction model (Equation 4.2)	

for reverse faulting and stiff soil conditions considering $M_w= 6.0$ and 7.0 and $R_{epi} = 10$ km and 20 km	70
Figure 4.21. Variation of inelastic input energy spectra $V_{eq} (R_{\mu}=4)$ with earthquake magnitude obtained from NF prediction model for different soil types and fault mechanisms, $R_{epi}=15$ km.....	71
Figure 4.22. Variation of inelastic input energy spectra $V_{eq} (R_{\mu}=4)$ with epicentral distance obtained from NF prediction model for different soil types and fault mechanisms, $M_w= 6.0$	71
Figure 4.23. Variation of inelastic input energy spectra $V_{eq} (R_{\mu}=4)$ with epicentral distance obtained from NF prediction model for different soil types and fault mechanisms, $M_w= 7.0$	71
Figure 5.1. Typical equivalent linear systems, (a) with period shift, (b) without period shift	74
Figure 5.2. (a) Energy, (b) displacement time histories. $T=1$ sec., 5% damping	77
Figure 5.3. The effect of M_w on e_{ξ} for both soil types and two R_{epi} groups	78
Figure 5.4. The effect of R_{epi} on e_{ξ} for both soil types and two M_w groups	79
Figure 5.5. The effect of fault type on e_{ξ} for both soil types and two R_{epi} groups	80
Figure 5.6. The effect of soil type on e_{ξ} for two magnitude and R_{epi} groups, respectively	80
Figure 5.7. Five percent damped mean acceleration response spectra of ordinary and near fault ground motions for four M_w Groups.	82
Figure 5.8. Mean $R_{\mu}-\xi-T$ spectra for equal displacement rule: Ordinary ground motions	85
Figure 5.9. Mean $R_{\mu}-\xi-T$ spectra for equal displacement rule: Near fault ground motions	85
Figure 5.10. Mean $R_{\mu}-\xi-T$ spectra for equivalent linearization with period shift: Ordinary ground motions.....	88
Figure 5.11. Mean $R_{\mu}-\xi-T$ spectra for equivalent linearization with period shift: Near fault ground motions.....	88

Figure 5.12. Comparison of median and standard deviation of maximum displacement ratios of elastic to inelastic SDOF systems: Ordinary ground motions	91
Figure 5.13. Comparison of median and standard deviation of maximum displacement ratios of elastic to inelastic SDOF systems: Near fault ground motions	92
Figure 5.14. Elevation and plan views of the 5-story frame, and capacity curve from first mode pushover analysis	94
Figure 5.15. Cross-section details of columns and beams of five story building	94
Figure 5.16. Mean maximum story displacements, interstory drift ratios, column bottom-end and beam-end chord rotations and plastic end rotations of the 5-story frame under ordinary ground motions.....	97
Figure 5.17. Mean maximum story displacements, interstory drift ratios, column bottom-end and beam-end chord rotations and plastic end rotations of the 5-story frame under near fault ground motions.....	98
Figure 6.1. Force-deformation response of an elastoplastic SDOF system	103
Figure 6.2. E_0/ E_I spectra (2% damping) for three different R_μ values with the corresponding mean and mean \pm standard deviation curves: NF ground motions ..	104
Figure 6.3. Comparison of mean E_0/ E_I spectra (2% damping) obtained for three different R_μ values: NF ground motions	105
Figure 6.4. Comparison of mean E_0/ E_I ratio spectra (2% damping) of four different M_w groups for $R_\mu=4$: NF ground motions	106
Figure 6.5. a) 5% damped PSa spectrum of GM46, b) Elastic equivalent velocity spectrum of GM46, c) E_0/E_I ratio spectrum of GM46 for $R_\mu=3$	110
Figure 6.6. Original frame: a) Comparison of maximum story displacements from NRHA and RSA under GM46, b) Comparison of maximum story drifts from NRHA and RSA under GM46.....	113
Figure 6.7. Comparison of maximum column end chord rotations from NRHA and RSA with modified EDR at the first story level	114
Figure 6.8. Comparison of maximum beam end chord rotations from NRHA and RSA with modified EDR at the first, second and third story levels, respectively	115

Figure 6.9. Modified frame: a) Comparison of maximum story displacement responses from NRHA and RSA under GM46, b) Comparison of maximum story drift responses from NRHA and RSA under GM46 117

Figure 6.10. Comparison of maximum column end chord rotations from NRHA and RSA with modified EDR at the first story level of the modified frame 118

Figure 6.11. Comparison of maximum beam end chord rotations from NRHA and RSA with modified EDR at the first, second and third story levels, respectively... 118

Figure 6.12. a) 5% damped PSa spectra of GM46 and GM52, b) Elastic equivalent velocity spectra of GM46 and GM52, c) E_0/E_I ratio spectra of GM46 and GM52 for $R_\mu=3$ 122

Figure 6.13. Member end moments from RSA w. modified EDR considering earthquake loads only from a) GM46, b) GM52 125

Figure 6.14. a) Comparison of maximum story displacements from NRHA of force-based design, NRHA of energy-based-based design and RSA with modified EDR under GM46, b) Comparison of maximum story drifts from NRHA of force-based design, NRHA of energy-based-based design and RSA with modified EDR under GM46..... 127

Figure 6.15. a) Comparison of maximum story displacements from NRHA of force-based design, NRHA of energy-based-based design and RSA with modified EDR under GM52, b) Comparison of maximum story drifts from NRHA of force-based design, NRHA of energy-based-based design and RSA with modified EDR under GM52..... 127

Figure 6.16. Plastic hinge distributions under GM46 record a) from NRHA of the frame with energy-based design, b) from NRHA of the frame with force-based design 128

Figure 6.17. Plastic hinge distributions under GM52 record a) from NRHA of the frame with energy-based design, b) from NRHA of the frame with force-based design 128

CHAPTER 1

INTRODUCTION

1.1. Problem Statement

Recent improvements in performance-based earthquake engineering require realistic description of seismic demands, and accurate estimation of supplied capacities in terms of both forces and deformations. Energy based approaches have a significant advantage in performance assessment because excitation and response durations, accordingly energy absorption and dissipation characteristics are directly considered whereas force and displacement-based procedures are based only on the maximum response parameters.

In conventional earthquake design practice, the effect of earthquake ground motion excitation on structural systems is taken into account by equivalent static inertial forces obtained from an acceleration design spectrum. Then, these inertial forces are applied to the system through response spectrum analysis procedures in order to obtain the maximum force and deformation demands for design purposes. Although this design procedure is generally considered appropriate under design like ground motions, the actual inelastic response under different ground motions is never prescribed during the design stage. To eliminate this shortcoming, performance or displacement-based design procedures have been developed to obtain the actual inelastic response more realistically, where the main design parameters are the maximum member deformations for evaluating the structural seismic performance. This approach improves the capacity design approaches up to some extent by considering maximum deformations instead of maximum forces. Structural components accumulate damage when dissipating the energy imposed by the ground motion excitation. Thus, maximum deformations as well as the response history

characteristics affect the level of damage on structural components during seismic response, and this joint effect complicates the nonlinear response problem. The present seismic design approaches are not capable of considering the seismic response history effects on structural component performances, and thus, there is a need for a new improvement in seismic design. At this stage, energy based design procedures can offer more comprehensive solutions for the response history effects.

Energy based procedures firstly require the prediction of earthquake input energy imposed on a structural system during an earthquake, and energy dissipation performance of the structure. Thus, such procedure requires predicting the energy dissipation mechanism both at the member and structural levels by considering energy balance during seismic response. Recent studies in this field have suggested several approaches, either by employing the part of input energy dissipated by hysteretic response of structural members as a performance parameter for structural members, or by using seismic energy as a supplementary design tool for improving the conventional procedures. Main part of these studies are complicated and far from being practical. Therefore, new developments and approaches are necessary in this field for making the seismic energy concept an important tool for seismic assessment and design in the near future.

1.2. Objective and Scope

Energy based design approaches include several levels, from SDOF to MDOF. At a broader context, energy based design are based on firstly the prediction of total input energy imposed by ground shaking, then estimating what portion of this energy can be dissipated by hysteretic response of structural components, and finally checking whether the structural components have sufficient hysteretic energy dissipation capacity for maintaining the design performance objectives during seismic response.

In this regard, a procedure for the prediction of earthquake input energy spectra considering the structural and ground motion related parameters is first introduced in this study. Moreover, inelastic structural response and near-fault effects are also

considered for input energy prediction. Then, energy dissipation characteristics at the SDOF and MDOF levels are studied. At this stage, the relation between input energy and dissipated energy is constructed, and a sensitivity analysis is conducted for energy dissipation efficiency of SDOF systems. For representing the inelastic system with a linear elastic system through equal deformation response, two different $R_{\mu-\zeta}-T$ spectra are derived for estimating the maximum displacement of inelastic SDOF systems from the maximum displacement of equivalent linear SDOF systems. At the final stage of the developed procedure, the predicted input energy and displacement spectra are employed integrally in order to estimate the energy dissipation mechanism of MDOF structural systems.

Main objective of this study is to ensure that, unlike the other conventional design approaches which induce all beam column connections as potential plastic hinge locations, seismic energy imparted to the system during seismic response can be dissipated effectively by a limited number plastic hinges at proper locations determined with the energy based design procedure developed in this study. The applicability and success of this energy-based procedure is tested, and improvements are suggested based on the comprehensive results obtained.

CHAPTER 2

REVIEW OF PAST STUDIES

2.1. Concept of Energy in Seismic Design, and Prediction of Input Energy

In conventional earthquake resistant design, the effect of earthquake ground shaking on structures is expressed by equivalent static inertial forces that are obtained from the acceleration design spectrum through response spectrum analysis. Although this approach is considered appropriate under design ground shaking when it is accompanied with the capacity design principles, the actual inelastic response is never assessed. Performance based design procedures offer a more realistic approach where maximum member deformations are employed as the basic structural response parameters in evaluating structural performance. However the level of damage on structural components during seismic response do not only depend on maximum deformations, but also on the response history characteristics. A structural component accumulates more damage as its energy dissipation capacity is exhausted, whereas this capacity is not independent of the excitation as assumed in the force and displacement-based design approaches, but strongly depends on the loading history (Erberik and Sucuoğlu 2004, Benavent-Climent 2007, Acun and Sucuoğlu 2010). Therefore, this is a complicated nonlinear problem.

Energy-based procedures may offer more comprehensive solutions. Housner (1956, 1959) suggested that if the energy loaded on a structure under a design earthquake is predicted, a rational design can be achieved by providing the capacity to dissipate the imposed input energy. Total seismic energy imposed by an earthquake ground motion on linear and nonlinear systems are almost equal to each other (Sucuoğlu and Nurtuğ 1995, Fajfar et al. 1989, Uang and Bertero 1988, Zahrah and Hall 1984). Moreover, Akiyama (1988) has shown that input energy calculated for a single degree of freedom

(SDOF) system can be used as a reliable estimate of the input energy for multi-story buildings. Therefore, the first task in developing an energy based-seismic design approach is the consistent prediction of input energy.

Input energy imposed by an earthquake ground motion on a SDOF system can be calculated by integrating the equation of motion over time (Sucuoğlu and Nurtuğ 1995, Zahrah and Hall 1984, Uang and Bertero 1990). Input energy can be defined in either absolute or relative terms (Uang and Bertero 1990) where both energy terms yield almost similar results in the period range of practical interest. Input energy-equivalent velocity (V_{eq}) spectra of damped elastic SDOF systems can also be predicted quite accurately by using smoothed Fourier amplitude spectrum of the input acceleration record (Kuwamura et al. 1994, Ordaz et al 2003).

Input energy design spectra can be estimated from the basic strong motion intensity and hazard parameters, which inherently depend on the source and site characteristics. Peak ground acceleration (PGA), peak ground velocity (PGV), PGV to PGA ratio (V/A ratio), effective duration, predominant period of ground motions, distance to fault, fault type, local soil condition, and earthquake magnitude were identified as the distinctive parameters for determining the input energy spectra of earthquake ground motions (Sucuoğlu and Nurtuğ 1995, Fajfar et al. 1989, Uang and Bertero 1988, Zahrah and Hall 1984, Akiyama 1988, Uang and Bertero 1990). These studies have further been extended to formulate input energy spectra in terms of ground motion intensity characteristics, as well as structural system properties (Benavent-Climent et al. 2002, 2010; Okur and Erberik 2012; Decanini and Mollaioli 1998, 2001; Amiri et al. 2008; Chou and Uang 2000, 2003; Chapman 1999; McKevitt et al. 1960; Fajfar and Fischinger 1990; Fajfar et al. 1992; Fajfar and Vidic 1994a, 1994b; Bruneau and Wang 1996; Nurtuğ and Sucuoğlu 1995; Manfredi 2001).

There are two basic approaches for defining input energy spectra in the current literature. In the first approach, design input energy is practically expressed in a piece-wise form as an envelope spectrum for the earthquakes recorded in the corresponding

seismic region. A bi-linear form is adopted in Akiyama (1988), Benavent-Climent et al. (2002), Benavent-Climent et al. (2010), and Okur and Erberik (2012) by assuming a linear variation of V_{eq} from zero to the corner period of ground motions. A constant velocity region start after this period. The constant maximum value is obtained statistically to envelope a certain percentile of the calculated maxima from the ground motions representing a hazard level on a given soil site. A three-piece form is employed in Fajfar et al. (1989), Decanini and Mollaioli (1998, 2001), Amiri et al. (2008), and Fajfar and Fischinger (1990) where a second corner period is utilized, which define the boundary of medium to long period region. In the longer period region after the second corner, the third segment of the spectra is defined as a decaying curve expressed as an inverse function of the period. Generally, the main purpose of these studies was to construct a demanding (enveloping) design spectrum in the corresponding seismic regions.

Design input energy spectra are obtained from prediction equations in the second approach. Chou and Uang (2000, 2003) conducted studies for predicting absorbed energy for an inelastic system by using a prediction equation, and showed that the absorbed energy converges to total input energy when the system responds elastically. They used the prediction equations developed by Boore et al. (1993, 1997) and calculated energy spectra for a given site class, earthquake magnitude, source to site distance, and ductility by conducting nonlinear regression analysis. Chapman (1999) and Ordaz et al. (2003) have presented the theoretical background for calculating elastic input energy spectra from prediction equations. Chapman (1999) also compared pseudo velocity (PS_V) spectrum with equivalent velocity (V_{eq}) spectrum, and obtained the ratio V_{eq}/PS_V for different earthquake magnitudes, source to site distances, and soil types. Cheng et al. (2014) developed prediction equations based on Boore et al. (1993, 1997) prediction model in order to predict the absolute and relative input energy spectra by using a large number of strong ground motion records.

The concept of input energy computation was extended to obtain the ratio of energy contributing to damage on the system to the total input energy (McKevitt et al. 1960,

Decanini and Mollaioli 2001, Fajfar and Fischinger 1990). Damping ratio, damping model, ductility, and hysteresis model were the basic parameters considered in determining the hysteretic to input energy ratio in spectral form. Fajfar et al. (1992) and Fajfar and Vidic (1994a, 1994b) presented extensive parametric studies for the seismic response of elastic and inelastic SDOF systems by means of basic structural and ground motion parameters. Similarly, other researchers proposed methods to obtain hysteretic energy dissipation in spectral form, by employing basic system and ground motion characteristics (Bruneau and Wang 1996, Nurtuğ and Sucuoğlu 1995, Manfredi 2001).

2.2. Near-Fault Effects On Elastic and Inelastic Input Energy Spectra

Input energy is also slightly different for linear elastic and inelastic systems. Moreover, strong ground motions from near-fault (NF) earthquakes impose higher energy dissipation demands compared to the ordinary far-fault (FF) ground motions from all distances. Understanding the basic characteristics of energy dissipation demands of earthquake ground motions is essential for establishing the energy dissipation capacity of structures, and accordingly for developing a comprehensive energy based design approach that accounts for the complex interaction between internal dynamic forces and deformations throughout the entire earthquake response duration.

Since 1950s, several researchers (Housner 1956; 1959, Zahrah and Hall 1984, Akiyama 1988, Fajfar et al. 1989, Uang and Bertero 1990, Sucuoğlu and Nurtuğ 1995) have presented pioneering studies for employing input energy in seismic design. They have suggested that a rational design might be possible by providing the capacity for a structural system necessary to dissipate the imposed input energy during seismic excitation. New technologies offer advanced energy dissipation devices for dissipating input seismic energy and accordingly reducing the heavy burden of inelastic energy dissipation on structural framing components (Soong and Spencer, 2002, Symans et

al 2008). Therefore, the first task in developing an energy-based design approach is the consistent prediction of seismic input energy.

Exact description of elastic and inelastic input energy spectra for recorded earthquake ground motions can be theoretically obtained by integrating the equation of motion over time for a class of SDOF systems (Zahrah and Hall 1984, Uang and Bertero 1990, Sucuoğlu and Nurtuğ 1995). Design input energy spectra for elastic or inelastic systems on the other hand can be estimated by two procedures: A) By employing prediction equations based on the site and source characteristics of ground motions recorded in the past (Chapman 1999, Chou and Uang 2000, Chou and Uang 2003, Cheng et al. 2014, Alıcı and Sucuoğlu 2016). B) By developing practical scaling rules relating the elastic or inelastic system and energy response parameters with the intensity parameters of recorded ground motions (Akiyama 1988, Benavent-Climent et al. 2002; 2010, Okur and Erberik 2012, McKevitt et al. 1960, Fajfar and Fischinger 1990, Fajfar et al. 1992; 1994, Vidic et al. 1994, Amiri et al. 2008, Decanini and Mollaioli 1998; 2001, Quinde et al. 2016). In fact, the most practical approach for obtaining input energy spectra for inelastic systems with different damping values (ξ) and lateral strength ratios (R_μ), which defines the ratio of the lateral elastic strength demand to the lateral strength capacity of the system, is applying scaling factors to a reference elastic input energy spectra derived for 5 percent damping. These approaches are schematized in Figure 2.1, where E_{ie} is the input energy for a linear elastic system (elastic input energy), E_{iy} is the input energy for a yielding system (inelastic input energy), and T , ξ , R_μ are the period, damping ratio and lateral strength ratio, respectively.

Operation paths (1) - (2), or (3) - (4) can be followed for converting the reference 5% damped elastic input energy spectrum into the inelastic input energy spectra for different ξ and R_μ . F_R and F'_R are the elastic to inelastic scaling functions for constant damping, and $F_{\xi e}$ and $F_{\xi y}$ are the damping scaling functions for elastic and inelastic systems respectively in Figure 2.1. The scaling operations summarized in Figure 2.1 are quite well established for the acceleration response spectra or design spectra.

However, the effect of ζ and R_μ on input energy spectra is not as distinct as in the acceleration response spectra (Quinde et al. 2016, Decanini and Mollaioli 2001). It will be investigated whether such scaling relations can be defined for near fault elastic and inelastic input energy spectra in this study.

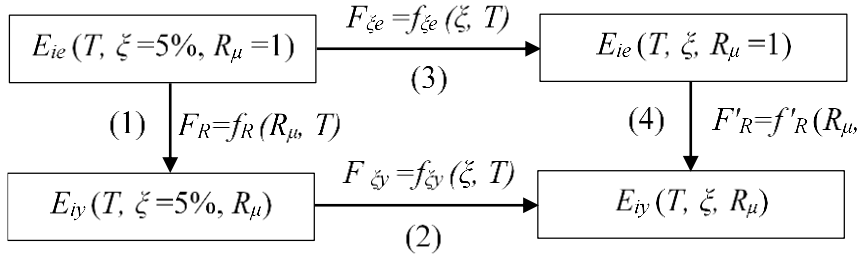


Figure 2.1. Different schemes for converting input energy spectra for a linear elastic system to the energy spectra for a yielding system

Ground motions recorded at close distances to the fault may possess special features that significantly affect seismic energy demand on structural systems when compared to ground motions with broad distance characteristics. Housner (1965) pointed out earlier that at near source locations, the relation between ground motion intensity and earthquake magnitude is not apparent as has been sometimes supposed, especially for moderate to larger magnitudes. Ground motions close to a fault are significantly affected by the faulting mechanism, direction of rupture propagation relative to the site (forward directivity effect), and the permanent ground displacement at the site (fling step effect). Depending on these effects, ground motions in the near-fault region may exhibit impulsive characteristics (Baker 2007, Bray and Rodriguez-Marek 2004, Kalkan and Kunnath 2006, Mollaioli et al. 2006). Near-fault ground motions do not necessarily exhibit impulsive characteristics in all orientations. Depending on the fault mechanism, fault normal or fault parallel components may display impulsive character due to directivity or fling-step effects (Baker 2007, Bray and Rodriguez-Marek 2004, Kalkan and Kunnath 2006, Mollaioli et al. 2006). Thus, seismic response of structures in the near fault of rupture has to be evaluated differently from those in the far fault due to possible impulsive characteristics. Near-fault earthquake ground motions lead

to extensively higher demands in structures when a pulse is observed in the velocity or displacement response histories where the severity of demands is related to the interaction between the pulse and system periods (Alavi and Krawinkler 2004, Chopra and Chintanapakdee 2001, Chioccarelli and Iervolino 2010; 2013, Iervolino et al. 2012, Iervolino and Cornell 2008, Kalkan and Kunnath 2006, Mavroeidis et al. 2004, Tothong et al. 2007, Wang et al. 2002, Zhang and Wang 2013).

Nonlinear response of degrading systems have been further investigated under near-fault ground motions with emphasis on inelastic displacement demands for seismic performance evaluation (Ruiz-García 2011, Iervolino et al. 2012, Zhang and Wang 2013, Liossatos and Fardis 2016). The principles of probabilistic seismic hazard analysis (PSHA) have also been extended to integrate the near-fault effects in expressing seismic hazard (Somerville et al. 1997, Tothong et al. 2007, Shahi and Baker 2011, Chioccarelli and Iervolino 2010; 2013).

CHAPTER 3

PREDICTION OF ELASTIC INPUT ENERGY SPECTRUM

Recent improvements in performance-based earthquake engineering require realistic description of seismic demands and accurate estimation of supplied capacities in terms of both forces and deformations. Energy based approaches have a significant advantage in performance assessment because excitation and response durations, accordingly energy absorption and dissipation characteristics are directly considered, whereas force and displacement-based procedures are based only on the maximum response parameters. Energy based procedures mainly consist of the prediction of earthquake input energy imposed on a structural system during an earthquake and energy dissipation performance of the structure.

The presented chapter focuses on the prediction of earthquake input energy. A large number of strong ground motions have been collected from the Next Generation Attenuation (NGA) project database, and parametric studies have been conducted for considering the effects of soil type, epicentral distance, moment magnitude, and the fault type on input energy. Then prediction equations for input energy spectra, which are expressed in terms of the equivalent velocity (V_{eq}) spectra, are derived in terms of these parameters. Moreover, a scaling operation has been developed based on consistent relations between pseudo velocity (PSV) and input energy spectra. When acceleration and accordingly velocity spectrum is available for a site from probabilistic seismic hazard analysis, it is possible to estimate the input energy spectrum by applying velocity scaling. Both of these approaches are found successful in predicting the V_{eq} spectrum at a site, either from prediction models for the considered earthquake source or from the results of probabilistic seismic hazard analysis conducted for the site.

3.1. Strong Ground Motion Database

The influence of earthquake ground motion characteristics on input energy is investigated by employing a large number of strong ground motion records selected from the NGA database. The ground motion records in the data set, each one containing accelerograms of two horizontal components representing a free field motion, were selected from 104 earthquakes which occurred in different regions in the world. The selection criteria for the ground motions were that the moment magnitudes (M_w) are larger than 5.5, and peak ground acceleration values (PGA) of the records are larger than $0.05g$ where g is the acceleration of gravity. Thus, the generated data ($M_w \geq 5.5$ and $PGA \geq 0.05g$) is composed of 1,442 pairs of ground motion records or 2,884 horizontal components. Figure 3.1 shows the scatter diagram of M_w versus R_{epi} for the ground motions used in the database. Additionally, Figure 3.2 shows the distribution of records in the database with V_{S30} (shear wave velocity of the upper 30 meters of soil profile). The limiting velocity value dividing soft and stiff soil classes in this study is 360 m/s. Ground motion sites in the database with V_{S30} values larger than the limiting value (NEHRP A, B, and C) are designated as stiff soil type, and those with lower V_{S30} values than the limiting value (NEHRP D and E) are specified as soft soil type.

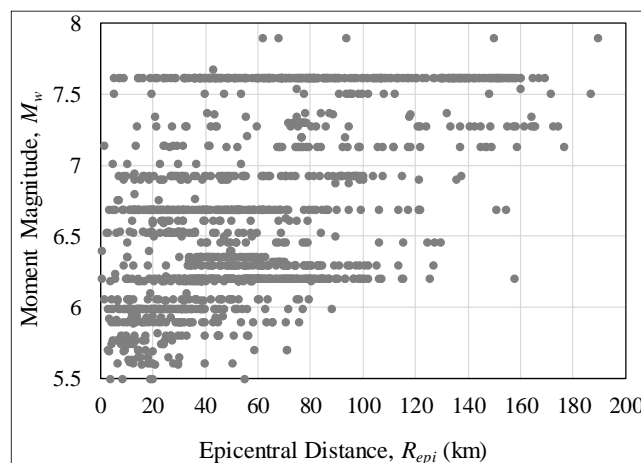


Figure 3.1. Magnitude-distance distribution of ground motions in the study

Soil class (S), distance to epicenter (R_{epi}), moment magnitude (M_w), and fault mechanism type are selected as the basic parameters in order to characterize source and site properties in input energy computations. The properties of the earthquakes in the database are summarized in Table 3.1 . It should be also noted that 93 ground motions are identified as pulse-like ground motions in the NGA database, and 22 ground motions with epicentral distances less than 5 km can be identified as near-fault. The fault directivity and pulse effects are not included in the prediction equation of input energy spectra, considering that few ground motions have these effects, and the additional terms in the prediction equation create additional complexity in the prediction model and affects the reliability of the results obtained from regression analysis.

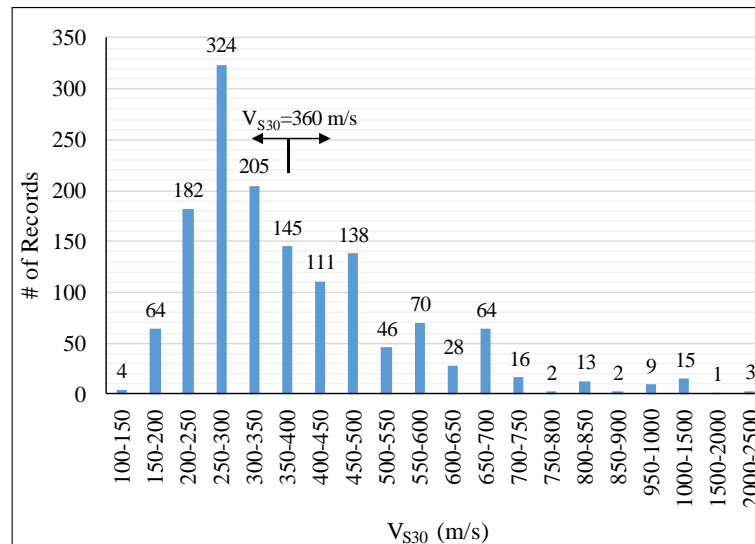


Figure 3.2. Distribution of ground motions with respect to V_{s30}

Table 3.1. Earthquakes used in the study

Earthquake	Year	M_w	Fault Mechanism Based on Rake Angle*	Depth, h (km)	R_{epi} (km)		V_{S30} (m/s)		Number of Records					Total Number of Records
					Min.	Max.	Min.	Max.	A	B	C	D	E	
Baja California	1987	5.50	0	6.0	3.7	3.7	659.6	659.6	0	0	1	0	0	1
Big Bear-01	1992	6.46	0	13.0	10.2	129.8	207.5	684.9	0	0	5	17	0	22
Bishop (Rnd Val)	1984	5.82	0	9.0	21.9	21.9	359.2	359.2	0	0	0	1	0	1
Borah Peak, ID-01	1983	6.88	1	16.0	89.5	94.3	424.8	659.6	0	0	2	0	0	2
Borrego	1942	6.50	0	8.0	57.8	57.8	213.4	213.4	0	0	0	1	0	1
Borrego Mtn	1968	6.63	0	8.0	70.8	70.8	213.4	213.4	0	0	0	1	0	1
Caldiran, Turkey	1976	7.21	2	10.0	55.7	55.7	274.5	274.5	0	0	0	1	0	1
Cape Mendocino	1992	7.01	2	9.6	4.5	53.3	311.8	712.8	0	0	4	2	0	6
Chalfant Valley-01	1986	5.77	0	6.7	10.5	27.0	271.4	345.4	0	0	0	4	0	4
Chalfant Valley-02	1986	6.19	0	10.0	14.3	35.2	271.4	359.2	0	0	0	9	0	9
Chalfant Valley-03	1986	5.65	0	5.0	15.2	25.9	271.4	271.4	0	0	0	2	0	2
Chi-Chi, Taiwan	1999	7.62	3	6.8	5.0	169.4	124.3	1525.9	1	3	148	142	9	303
Chi-Chi, Taiwan-02	1999	5.90	2	8.0	5.5	75.9	212.7	664.4	0	0	12	9	0	21
Chi-Chi, Taiwan-03	1999	6.20	2	8.0	0.5	84.3	172.1	664.4	0	0	26	12	1	39
Chi-Chi, Taiwan-04	1999	6.20	0	18.0	10.1	79.7	193.0	553.4	0	0	20	12	0	32
Chi-Chi, Taiwan-05	1999	6.20	2	10.0	35.6	157.7	169.8	714.3	0	0	55	56	3	114
Chi-Chi, Taiwan-06	1999	6.30	2	16.0	8.8	127.0	169.8	664.4	0	0	34	44	3	81
Coalinga-01	1983	6.36	2	4.6	10.0	62.7	184.8	684.9	0	0	22	21	0	43
Coalinga-05	1983	5.77	2	7.4	4.6	16.2	257.4	617.4	0	0	7	4	0	11
Corinth, Greece	1981	6.60	1	7.2	19.9	19.9	338.6	338.6	0	0	0	1	0	1
Coyote Lake	1979	5.74	0	9.6	4.4	23.9	221.8	1428.0	0	1	5	3	0	9
Denali, Alaska	2002	7.90	0	4.9	61.9	189.7	376.1	963.9	0	2	3	0	0	5
Dinar, Turkey	1995	6.40	1	5.0	0.4	49.7	219.8	338.6	0	0	0	2	0	2
Double Springs	1994	5.90	0	5.0	16.9	16.9	345.4	345.4	0	0	0	1	0	1
Duzce, Turkey	1999	7.14	0	10.0	1.6	41.5	276.0	659.6	0	0	6	3	0	9

Table 3.1. Earthquakes used in the study (continued)

Earthquake	Year	M_w	Fault Mechanism Based on Rake Angle*	Depth, h (km)	R_{epi} (km)		V_{S30} (m/s)		Number of Records					Total Number of Records
					Min.	Max.	Min.	Max.	A	B	C	D	E	
Erzican, Turkey	1992	6.69	0	9.0	274.5	274.5	0	0	0	0	0	1	0	1
Friuli, Italy-01	1976	6.50	2	5.1	20.2	89.6	274.5	424.8	0	0	1	2	0	3
Friuli, Italy-02	1976	5.91	2	3.7	17.1	18.0	338.6	659.6	0	0	2	1	0	3
Friuli, Italy-03	1976	5.50	1	6.0	20.0	20.0	412.4	412.4	0	0	1	0	0	1
Gazli, USSR	1976	6.80	1	18.2	12.8	12.8	659.6	659.6	0	0	1	0	0	1
Georgia, USSR	1991	6.20	2	6.0	40.2	60.2	274.5	274.5	0	0	0	3	0	3
Griya, Greece	1990	6.10	1	9.5	32.9	32.9	424.8	424.8	0	0	1	0	0	1
Gulf of Aqaba	1995	7.20	0	12.5	93.4	93.4	354.9	354.9	0	0	0	1	0	1
Hector Mine	1999	7.13	0	5.0	26.5	176.5	207.5	684.9	0	0	11	24	0	35
Helena, Montana-01	1935	6.00	0	6.0	6.3	6.3	659.6	659.6	0	0	1	0	0	1
Hollister-01	1961	5.60	0	7.4	20.6	20.6	198.8	198.8	0	0	0	1	0	1
Hollister-02	1961	5.50	0	7.4	18.9	18.9	198.8	198.8	0	0	0	1	0	1
Imperial Valley-02	1940	6.95	0	8.8	13.0	13.0	213.4	213.4	0	0	0	1	0	1
Imperial Valley-06	1979	6.53	0	10.0	2.5	83.9	162.9	659.6	0	0	2	30	1	33
Imperial Valley-08	1979	5.62	0	3.3	11.0	11.0	193.7	193.7	0	0	0	1	0	1
Irpinia, Italy-01	1980	6.90	1	9.5	15.0	48.3	350.0	1000.0	0	4	3	1	0	8
Irpinia, Italy-02	1980	6.20	1	7.0	12.0	29.8	530.0	1000.0	0	3	2	0	0	5
Kalamata, Greece-01	1986	6.20	1	5.0	10.0	10.0	338.6	338.6	0	0	0	1	0	1
Kern County	1952	7.36	2	16.0	43.5	118.3	316.5	515.0	0	0	2	1	0	3
Kobe, Japan	1995	6.90	0	17.9	8.7	135.6	256.0	609.0	0	0	4	7	0	11
Kocaeli, Turkey	1999	7.51	0	15.0	5.3	187.0	175.0	811.0	0	2	6	10	1	19
Kozani, Greece-01	1995	6.40	1	12.6	18.3	18.3	659.6	659.6	0	0	1	0	0	1
Landers	1992	7.28	0	7.0	13.7	174.5	207.5	684.9	0	0	7	26	0	33
Lazio-Abruzzo, Italy	1984	5.80	1	14.0	13.0	50.6	200.0	659.6	0	0	1	3	0	4
Little Skull Mtn., NV	1992	5.65	1	12.0	14.1	30.2	274.5	659.6	0	0	1	1	0	2

Table 3.1. Earthquakes used in the study (continued)

Earthquake	Year	M_w	Fault Mechanism Based on Rake Angle*	Depth, h (km)	R_{epi} (km)		V_{S30} (m/s)		Number of Records					Total Number of Records
					Min.	Max.	Min.	Max.	A	B	C	D	E	
					Min.	Max.	Min.	Max.	A	B	C	D	E	
Livermore-01	1980	5.80	0	12.0	17.1	56.1	271.4	517.1	0	0	1	3	0	4
Loma Prieta	1989	6.93	3	17.5	7.2	137.6	116.4	1428.0	0	6	39	29	4	78
Mammoth Lakes-01	1980	6.06	4	9.0	1.4	12.7	338.5	370.8	0	0	1	2	0	3
Mammoth Lakes-02	1980	5.69	0	14.0	3.5	20.1	338.5	370.8	0	0	1	2	0	3
Mammoth Lakes-03	1980	5.91	0	16.0	5.9	11.5	338.5	345.4	0	0	0	4	0	4
Mammoth Lakes-04	1980	5.70	0	5.0	2.8	14.2	338.5	345.4	0	0	0	4	0	4
Mammoth Lakes-05	1980	5.70	0	4.7	9.4	16.9	338.5	345.4	0	0	0	2	0	2
Mammoth Lakes-06	1980	5.94	0	14.0	12.0	46.5	271.4	345.4	0	0	0	5	0	5
Managua, Nicaragua-01	1972	6.24	0	5.0	5.7	5.7	288.8	288.8	0	0	0	1	0	1
Manjil, Iran	1990	7.37	0	19.0	40.4	131.7	274.5	724.0	0	0	1	4	0	5
Morgan Hill	1984	6.19	0	8.5	3.9	80.3	116.4	1428.0	0	1	8	13	1	23
Mt. Lewis	1986	5.60	0	9.2	15.9	15.9	281.6	281.6	0	0	0	1	0	1
N. Palm Springs	1986	6.06	3	11.0	4.2	79.2	207.5	684.9	0	0	11	17	0	28
Nahanni, Canada	1985	6.76	2	8.0	6.5	22.4	659.6	659.6	0	0	3	0	0	3
New Zealand-01	1984	5.50	0	9.0	8.2	8.2	274.5	274.5	0	0	0	1	0	1
New Zealand-02	1987	6.60	1	6.4	24.2	24.2	424.8	424.8	0	0	1	0	0	1
New Zealand-03	1987	5.80	1	11.0	26.9	26.9	424.8	424.8	0	0	1	0	0	1
Norcia, Italy	1979	5.90	1	6.0	4.3	4.3	659.6	659.6	0	0	1	0	0	1
Northern Calif-01	1941	6.40	0	10.0	49.5	49.5	219.3	219.3	0	0	0	1	0	1
Northern Calif-03	1954	6.50	0	10.0	30.8	30.8	219.3	219.3	0	0	0	1	0	1
Northern Calif-04	1960	5.70	0	10.0	58.8	58.8	219.3	219.3	0	0	0	1	0	1
Northern Calif-05	1967	5.60	0	10.0	29.7	29.7	219.3	219.3	0	0	0	1	0	1
Northridge-01	1994	6.69	2	17.5	3.4	154.4	160.6	2016.1	2	11	69	69	1	152
Northridge-02	1994	6.05	2	6.0	6.6	39.2	278.0	508.1	0	0	2	5	0	7
Northridge-04	1994	5.93	3	9.8	17.3	27.0	405.2	450.3	0	0	2	0	0	2

Table 3.1. Earthquakes used in the study (continued)

Earthquake	Year	M_w	Fault Mechanism Based on Rake Angle*	Depth, h (km)	R_{epi} (km)		V_{S30} (m/s)		Number of Records					Total Number of Records
					Min.	Max.	Min.	Max.	A	B	C	D	E	
					Max.	Min.	Max.	Min.	A	B	C	D	E	
Northwest Calif-01	1938	5.50	0	10.0	54.9	54.9	219.3	219.3	0	0	0	1	0	1
Northwest Calif-03	1951	5.80	0	10.0	56.0	56.0	219.3	219.3	0	0	0	1	0	1
Northwest China-01	1997	5.90	0	23.1	13.2	13.2	274.5	274.5	0	0	0	1	0	1
Northwest China-02	1997	5.93	1	31.0	23.1	23.1	274.5	274.5	0	0	0	2	0	2
Northwest China-03	1997	6.10	1	20.0	19.1	19.1	274.5	274.5	0	0	0	1	0	1
Northwest China-04	1997	5.80	4	22.4	25.0	25.0	274.5	274.5	0	0	0	2	0	2
Oroville-01	1975	5.89	1	5.5	12.6	12.6	622.9	622.9	0	0	1	0	0	1
Parkfield	1966	6.19	0	10.0	32.6	40.3	256.8	527.9	0	0	2	2	0	4
Point Mugu	1973	5.65	2	8.0	18.1	18.1	297.9	297.9	0	0	0	1	0	1
San Fernando	1971	6.61	2	13.0	11.9	78.9	235.0	2016.1	1	2	13	4	0	20
San Salvador	1986	5.80	0	10.9	7.9	9.5	350.0	545.0	0	0	1	1	0	2
Santa Barbara	1978	5.92	3	12.7	3.2	3.2	515.0	515.0	0	0	1	0	0	1
Sierra Madre	1991	5.61	2	12.0	6.5	50.3	257.2	996.4	0	2	5	2	0	9
Sitka, Alaska	1972	7.68	0	29.0	42.9	42.9	659.6	659.6	0	0	1	0	0	1
Spitak, Armenia	1988	6.77	3	6.0	36.2	36.2	274.5	274.5	0	0	0	1	0	1
St Elias, Alaska	1979	7.54	2	15.7	74.8	160.0	274.5	274.5	0	0	0	2	0	2
Superstition Hills-01	1987	6.22	0	10.0	24.8	24.8	207.5	207.5	0	0	0	1	0	1
Superstition Hills-02	1987	6.54	0	9.0	7.5	35.8	191.1	362.4	0	0	1	10	0	11
Tabas, Iran	1978	7.35	2	5.8	20.6	164.4	274.5	766.8	0	1	1	3	0	5
Taiwan SMART1(33)	1985	5.80	2	3.3	44.7	45.1	274.5	274.5	0	0	0	5	0	5
Taiwan SMART1(40)	1986	6.32	2	15.8	65.5	70.3	274.5	274.5	0	0	0	8	0	8
Taiwan SMART1(45)	1986	7.30	2	15.0	71.4	78.2	274.5	659.6	0	0	1	14	0	15
Taiwan SMART1(5)	1981	5.90	2	11.1	28.7	32.0	274.5	274.5	0	0	0	7	0	7
Trinidad	1980	7.20	0	15.1	76.8	76.8	311.8	311.8	0	0	0	3	0	3
Trinidad offs hore	1983	5.70	0	11.9	71.2	71.2	311.8	311.8	0	0	0	2	0	2

Table 3.1. Earthquakes used in the study (continued)

Earthquake	Year	M_w	Fault Mechanism Based on Rake Angle*	Depth, h (km)	R_{epi} (km)		V_{S30} (m/s)		Number of Records					Total Number of Records
					Min.	Max.	Min.	Max.	A	B	C	D	E	
Upland	1990	5.63	0	4.5	10.8	12.2	229.8	390.2	0	0	1	1	0	2
Victoria, Mexico	1980	6.33	0	11.0	33.7	58.9	274.5	659.6	0	0	1	2	0	3
Westmorland	1981	5.90	0	2.3	7.0	25.0	191.1	362.4	0	0	1	5	0	6
Whittier Narrows-01	1987	5.99	3	14.6	2.9	88.2	160.6	996.4	0	3	40	52	1	96

* 0, 1, 2, 3 and 4 denote strike-slip, normal, reverse, reverse-oblique, and normal-oblique, respectively.

3.2. Elastic Input Energy

Input energy demand on a linear elastic SDOF system can be obtained by integrating the equation of motion over displacement as shown in Equation 3.1, where m , c and k are mass, viscous damping and stiffness of the SDOF system respectively, u is the relative displacement of the SDOF system with respect to the ground and \ddot{u}_g is the ground acceleration. Equation 3.1 can be rearranged in Equation 3.2, where E_K is the kinetic energy, E_S is the recoverable strain energy and E_D is the energy dissipated by viscous damping. The right hand side of Equation 3.2 expresses the total input energy, as the work done by the equivalent seismic force $-m\ddot{u}_g(t)$ on the relative displacement of SDOF system relative to the ground.

$$\int_0^{u(t)} m \ddot{u}(t) du + \int_0^{u(t)} c \dot{u}(t) du + \int_0^{u(t)} k u du = - \int_0^{u(t)} m \ddot{u}_g(t) du \quad (3.1)$$

$$E_K(t) + E_D(t) + E_S(t) = E_I(t) \quad (3.2)$$

The total input energy E_I , which is calculated at the end of ground motion duration, is entirely dissipated by viscous damping in a linear elastic system. Elastic input energy can be converted into equivalent velocity (V_{eq}) in order to eliminate the dependence on mass by using Equation 3.3.

$$V_{eq} = \sqrt{(2 E_I / m)} \quad (3.3)$$

In the foregoing analysis, the elastic input energy spectrum of each GM is obtained as equivalent velocity V_{eq} spectrum where V_{eq} is calculated as the geometric mean of the two horizontal components of each GM as shown in Equation 3.4. Viscous damping ratio in Equation 3.1 is taken as 5%.

$$V_{eq} = \sqrt{(V_{eq,H1}) (V_{eq,H2})} \quad (3.4)$$

An energy-based approach in seismic design requires an energy dissipation capacity for a structural system which is capable of dissipating the input energy demand while the system satisfies basic performance limit states. Therefore, it is required to describe the design input energy spectrum for the design site. Two approaches have been developed in this chapter for estimating input energy spectrum for a site. In the first approach, V_{eq} spectrum of a strong ground motion from an earthquake source is estimated by using the prediction model based on soil type, distance to fault, earthquake magnitude and fault mechanism. This approach is somewhat similar to a deterministic seismic hazard analysis in terms of input energy (Chou and Uang, 2000). In the second approach, V_{eq} spectrum is obtained from its associated pseudo velocity (PS_V) spectrum by using a scaling operation between them. When design acceleration spectrum, and hence the associated pseudo velocity spectrum PS_V for a site is available from probabilistic seismic hazard analysis, design V_{eq} spectrum can then be obtained by employing the scaling operation proposed herein. Therefore, the two approaches suggested below can be respectively classified as deterministic and probabilistic.

3.3. Input Energy Prediction by Prediction Equations

Prediction equations provide a description for an intensity parameter in terms of the basic source and site parameters, namely, earthquake magnitude, source to site distance, soil type, and fault mechanism. They are obtained by fitting a functional form to an empirical data through regression analyses. The prediction model developed by Akkar and Bommer (2007a, 2007b, 2010) is employed in this study in order to predict the equivalent velocity spectrum at a given location for a given earthquake source, source to site distance, and site conditions. Their prediction equation is given in Equation 3.5.

$$\log(V_{eq}) = b_1 + b_2 M + b_3 M^2 + (b_4 + b_5 M) \log \sqrt{R_{jb}^2 + b_6^2} + b_7 S_S + b_8 S_A + b_9 F_N + b_{10} F_R \quad (3.5)$$

In Equation 3.5, M is the moment magnitude and R_{jb} is the Joyner-Boore distance in kilometers. S_S and S_A are dummy variables representing the influence of site class. S_S is 0 and S_A is 1 for stiff sites, and S_S is 1 and S_A is 0 for soft sites. F_N is zero and F_R is 1 for reverse faulting, and the opposite for normal faulting. They are both 0 for strike-slip faulting. The prediction equation in Equation 3.5 has been modified with respect to the seismic design practices and the parameters related to the earthquake characteristics and fault types associated with the GM records utilized in this study. For this purpose, epicentral distance R_{epi} is used as the distance parameter instead of R_{jb} , and terms b_7S_S and b_8S_A related to the soil type are combined and labeled as b_7S in which S is equal to 1 for soft soil, and 0 for stiff soil. When all these changes are implemented, Equation 3.5 reduces to Equation 3.6.

$$\log(V_{eq}) = b_1 + b_2M + b_3M^2 + (b_4 + b_5M) \log \sqrt{R_{epi}^2 + b_6^2} + b_7S + b_8F_N + b_9F_R \quad (3.6)$$

The undetermined coefficients in Equation 3.6 are determined by a one-stage nonlinear regression analysis at the specified period values for observed (computed) spectral values of linear elastic systems. The regression coefficients in Equation 3.6 and the corresponding standard deviations σ at each period are presented in Table 3.2. Predicted V_{eq} values from Equation (3.6) and Table 3.2 are in the units of m/s. Furthermore, residuals (Res) between observed and estimated V_{eq} values were computed by using the expression given in Equation 3.7. Examples of the scatter plots for these residuals relative to R_{epi} and M are shown in Figure 3.3 along with the best fit lines in order to reveal whether the estimated results from the prediction model are unbiased or biased with respect to the parameters R_{epi} and M . In Table 3.3, the slopes of these lines for all period values are also presented. Accordingly, it is clear that the calculated slopes are almost equal to zero which means that the data are uniformly distributed among the predictor variables M and R_{epi} , and hence the estimated values from the prediction model can be classified as unbiased with respect to the independent variables R_{epi} and M .

$$Res = \log(V_{eq_{est.}}) - \log(V_{eq_{obs.}}) \quad (3.7)$$

Table 3.2. Regression coefficients calculated for the prediction model

T (sec.)	b₁	b₂	b₃	b₄	b₅	b₆	b₇	b₈	b₉	σ
0.04	-6.7311	1.1311	-0.0292	1.4329	-0.3451	5.9923	-0.0132	-0.1766	-0.0675	0.286
0.10	-6.8986	1.5091	-0.0634	1.1510	-0.3019	7.9587	-0.0067	-0.1525	-0.0669	0.266
0.20	-7.8848	1.9630	-0.1034	0.6448	-0.2131	7.4717	0.0278	-0.0506	-0.0332	0.213
0.30	-7.2983	1.7988	-0.0929	0.4769	-0.1745	4.8839	0.0581	-0.0697	0.0055	0.205
0.40	-7.9272	1.9987	-0.1082	0.3038	-0.1461	5.5817	0.0757	-0.0336	0.0225	0.211
0.50	-6.7183	1.6872	-0.0885	0.0349	-0.1050	5.9564	0.0916	-0.0407	0.0339	0.223
0.60	-7.7329	2.0915	-0.1268	-0.5247	-0.0178	5.1838	0.1025	-0.0523	0.0397	0.233
0.70	-8.0485	2.2630	-0.1451	-0.9481	0.0435	4.8084	0.1136	-0.0664	0.0491	0.244
0.80	-7.2850	1.9890	-0.1217	-0.8404	0.0276	5.1292	0.1281	-0.0638	0.0472	0.250
0.90	-7.9541	2.1704	-0.1342	-0.8630	0.0329	5.4492	0.1319	-0.0656	0.0468	0.256
1.00	-8.2500	2.2375	-0.1387	-0.8459	0.0338	5.7942	0.1400	-0.0633	0.0500	0.264
1.20	-8.9064	2.3680	-0.1447	-0.6941	0.0151	5.0968	0.1622	-0.0892	0.0279	0.281
1.40	-9.4288	2.4217	-0.1417	-0.4186	-0.0252	5.1836	0.1762	-0.0987	0.0132	0.289
1.50	-9.9234	2.5239	-0.1462	-0.3064	-0.0420	4.8461	0.1801	-0.1098	0.0135	0.292
1.60	-10.4924	2.6607	-0.1542	-0.2487	-0.0507	4.7773	0.1837	-0.1052	0.0102	0.295
1.80	-10.6677	2.6649	-0.1526	-0.2112	-0.0527	4.3636	0.1980	-0.0924	0.0052	0.302
2.00	-10.6616	2.6143	-0.1461	-0.1138	-0.0662	4.1496	0.1986	-0.0848	0.0046	0.311
2.50	-11.2925	2.7023	-0.1453	0.1255	-0.1057	5.4719	0.1993	-0.1232	0.0059	0.328
3.00	-10.8501	2.4319	-0.1162	0.4613	-0.1543	5.9322	0.2003	-0.1206	-0.0136	0.335
3.50	-9.7835	2.0297	-0.0798	0.5842	-0.1773	7.7649	0.1984	-0.1204	-0.0304	0.332
4.00	-9.1531	1.8696	-0.0699	0.3064	-0.1395	8.8112	0.1958	-0.1442	-0.0476	0.328

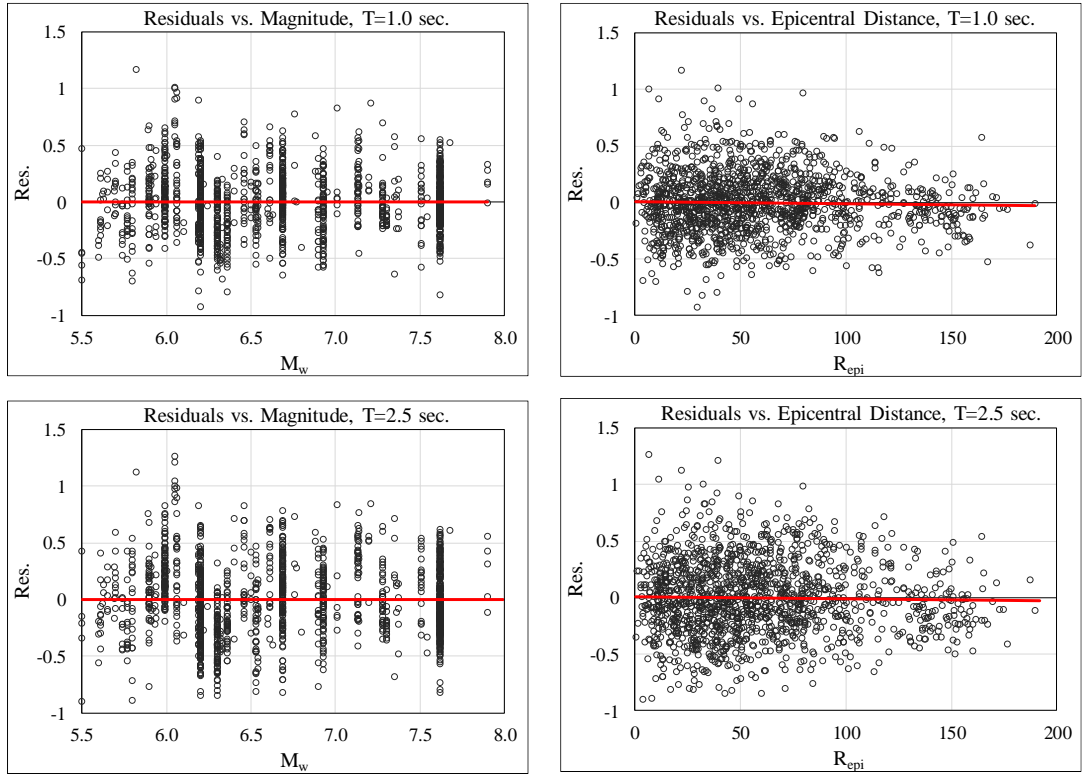


Figure 3.3. Residual plots of observed and estimated V_{eq} spectral values

Table 3.3. Slope of the best fit lines in the scatter plots of residuals with respect to M and R_{epi}

T (sec.)	Residuals vs. M	Residuals vs. R_{epi}
0.04	0.000000043	-0.0000748
0.10	0.000000025	-0.0000269
0.20	0.000000051	-0.0000442
0.30	0.000000023	-0.0000393
0.40	0.000000006	-0.0000653
0.50	0.000000041	-0.0001112
0.60	0.000000013	-0.0001479
0.70	0.000000032	-0.0001851
0.80	0.000000064	-0.0001875
0.90	0.000000043	-0.0002080
1.00	0.000000049	-0.0001987
1.20	0.000000015	-0.0002303
1.40	0.000000004	-0.0001940
1.50	0.000000006	-0.0001914
1.60	0.000000023	-0.0001908
1.80	-0.000000009	-0.0001981
2.00	0.000000124	-0.0002137
2.50	-0.000001559	-0.0001830
3.00	0.000000005	-0.0001542
3.50	0.000000044	-0.0001244
4.00	0.000000173	-0.0001290

In order to evaluate the estimation accuracy of Equation 3.6, the variation of 5% damped V_{eq} with distance R_{epi} is obtained and plotted for selected earthquakes with six different moment magnitudes for the mean and mean \pm one standard deviation at three specified periods of 0.5, 1.0 and 2.0 seconds. Then, the computed (observed) V_{eq} spectral values of the ground motions from the selected earthquakes at these specified periods are plotted on the related graphics in scatter form. Chi-Chi (1999), Hector Mine (1999), Düzce (1999), Loma Prieta (1989), Northridge-01 (1994) and Whittier Narrows-01 (1987) earthquakes with respective moment magnitudes of 7.62, 7.14, 7.13, 6.93, 6.69 and 5.99 were selected for comparative evaluation. Fault rapture mechanisms of these earthquakes can be listed as reverse-oblique, strike-slip, strike-slip, reverse oblique, reverse and reverse-oblique, respectively. Figure 3.4 to Figure 3.8 present the comparisons of the computed V_{eq} spectral ordinates with the mean \pm sigma variations of V_{eq} obtained from the proposed prediction equation (Equation 3.6 and Table 3.2) for stiff and soft soil ground motions recorded during the selected earthquakes. Due to the identical moment magnitude and fault mechanisms, the observed V_{eq} values of the ground motion records from Hector Mine (1999) and Düzce (1999) earthquakes are plotted together in Figure 3.5. It can be inferred from these figures that the observed V_{eq} spectral values generally fall within the range of mean \pm one standard deviation.

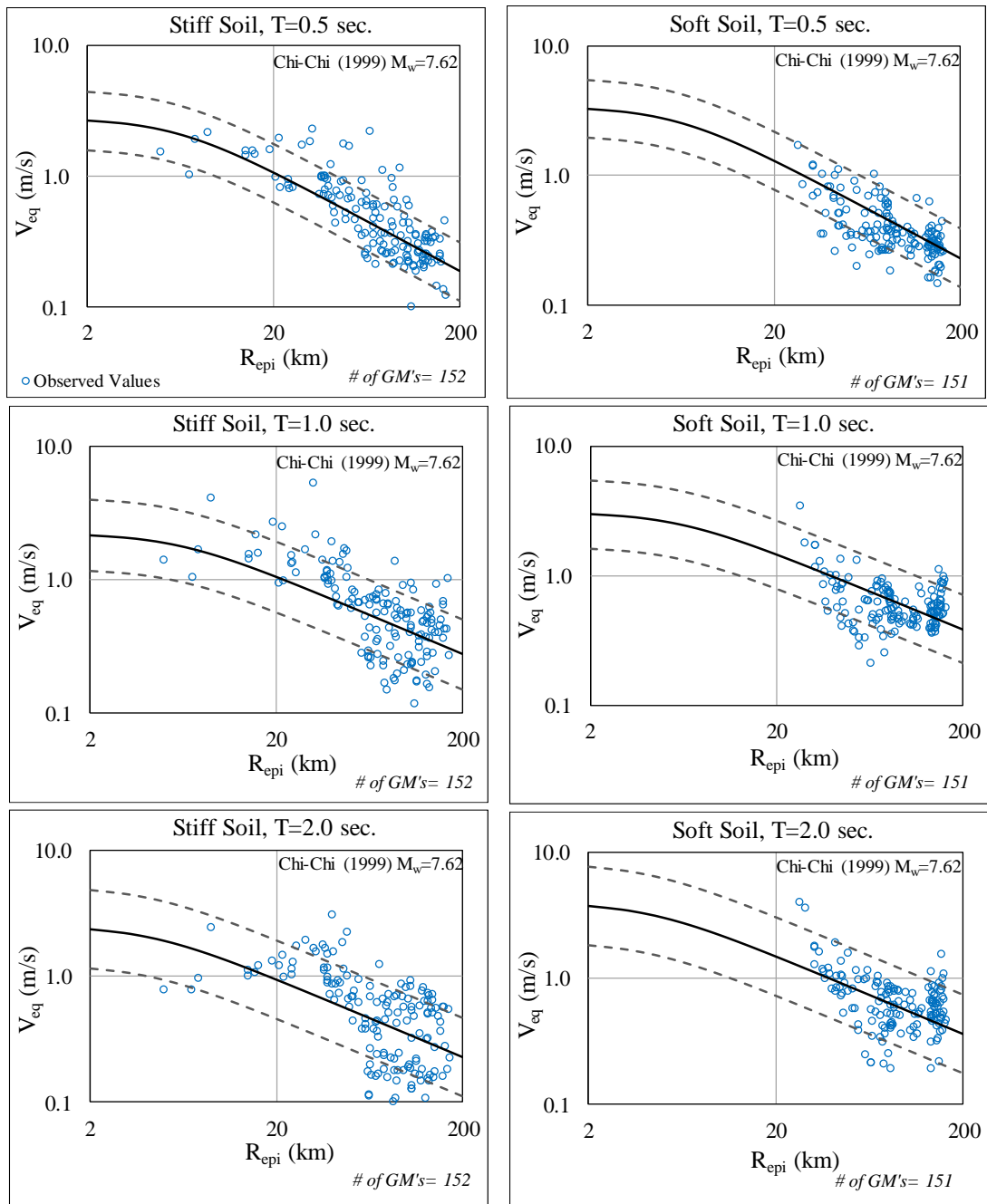


Figure 3.4. Comparison of the computed V_{eq} with the mean and mean \pm one standard deviations of the prediction model for $M_w=7.62$ Chi-Chi (1999) earthquake, for stiff and soft soil types

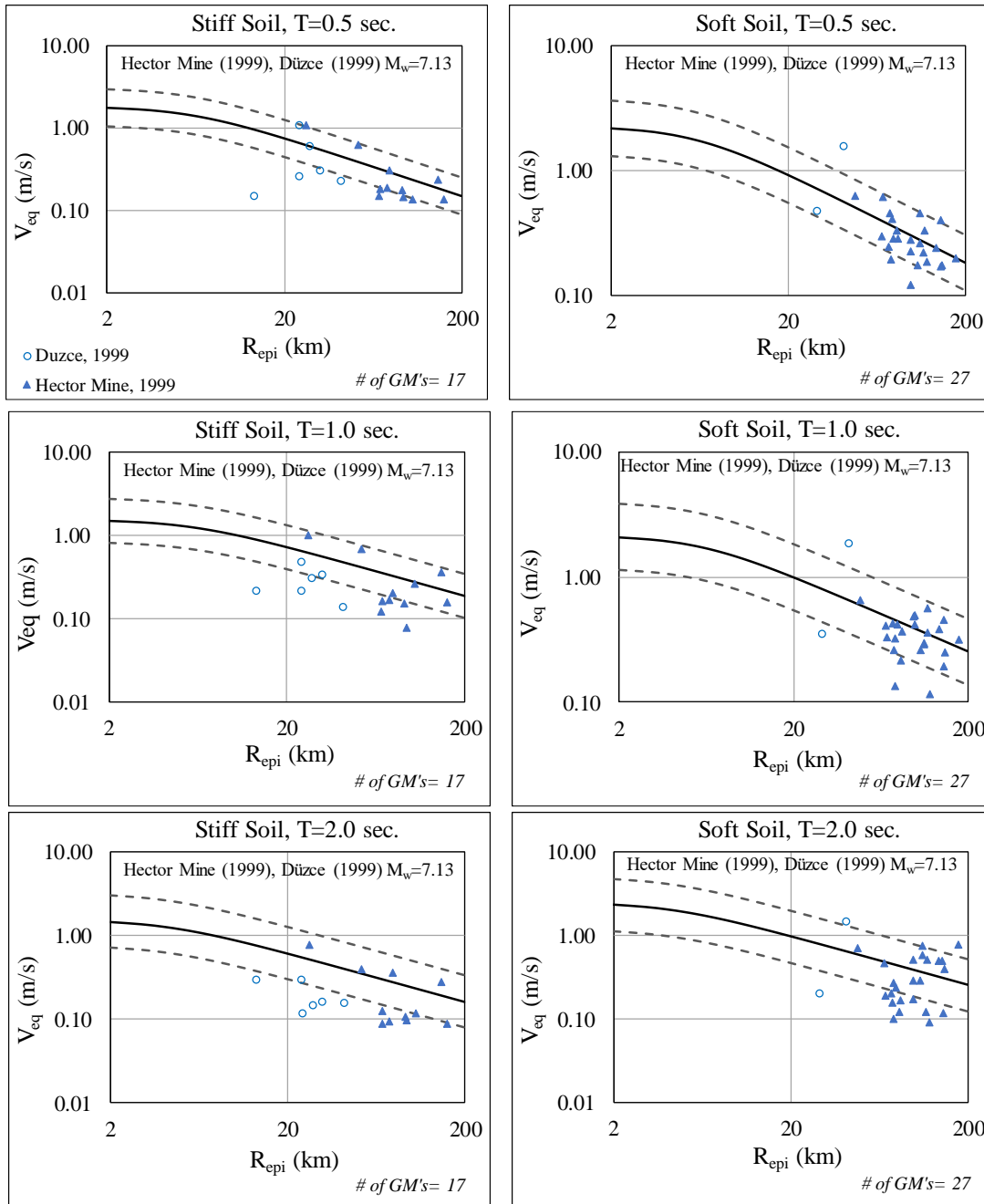


Figure 3.5. Comparison of the computed V_{eq} with the mean and mean \pm one standard deviations of the prediction model for $M_w=7.13$ Hector Mine (1999) and Düzce (1999) earthquakes, for stiff and soft soil types

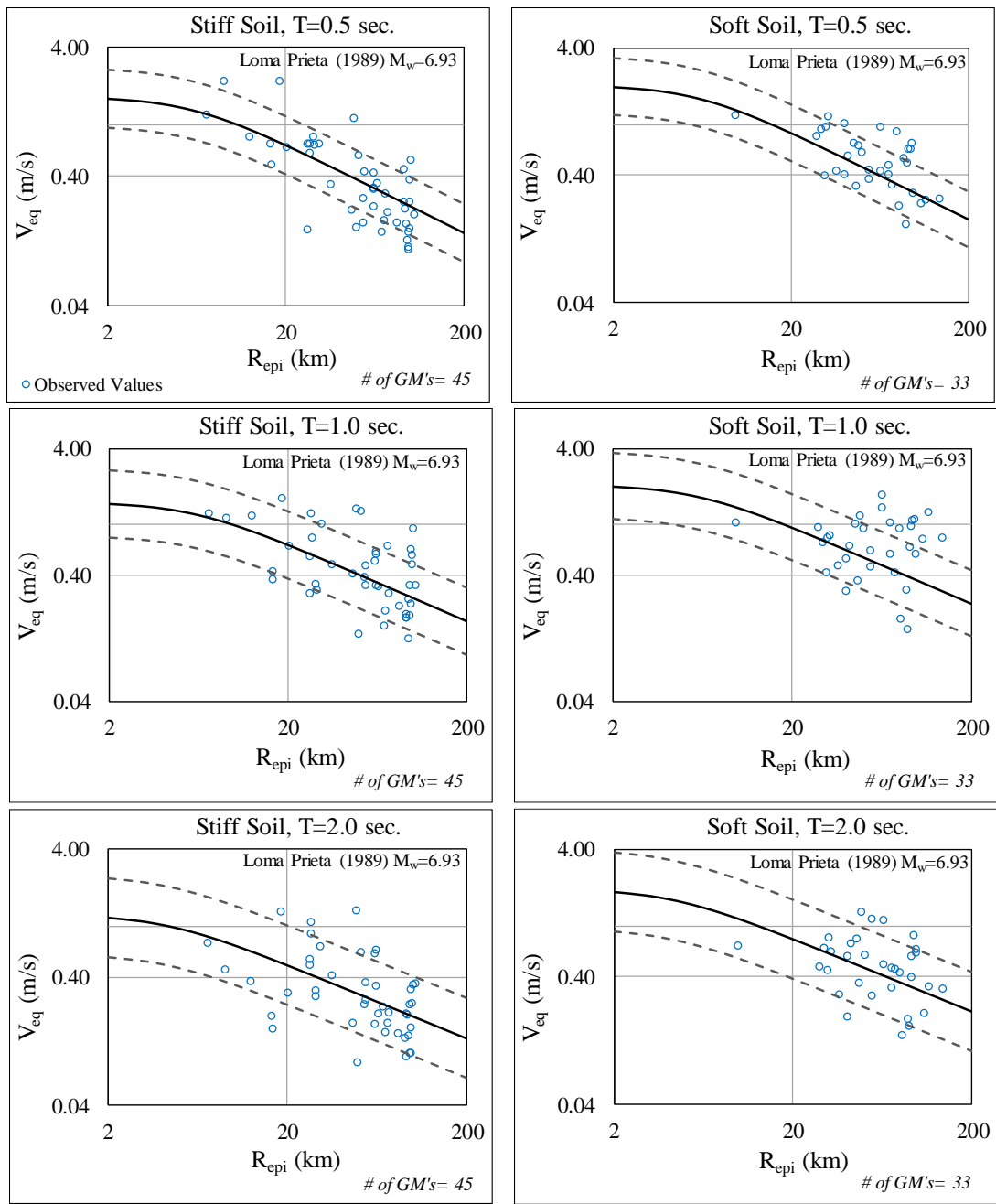


Figure 3.6. Comparison of the computed V_{eq} with the mean and mean \pm one standard deviations of the prediction model for $M_w=6.93$ Loma Prieta (1989) earthquake, for stiff and soft soil types.

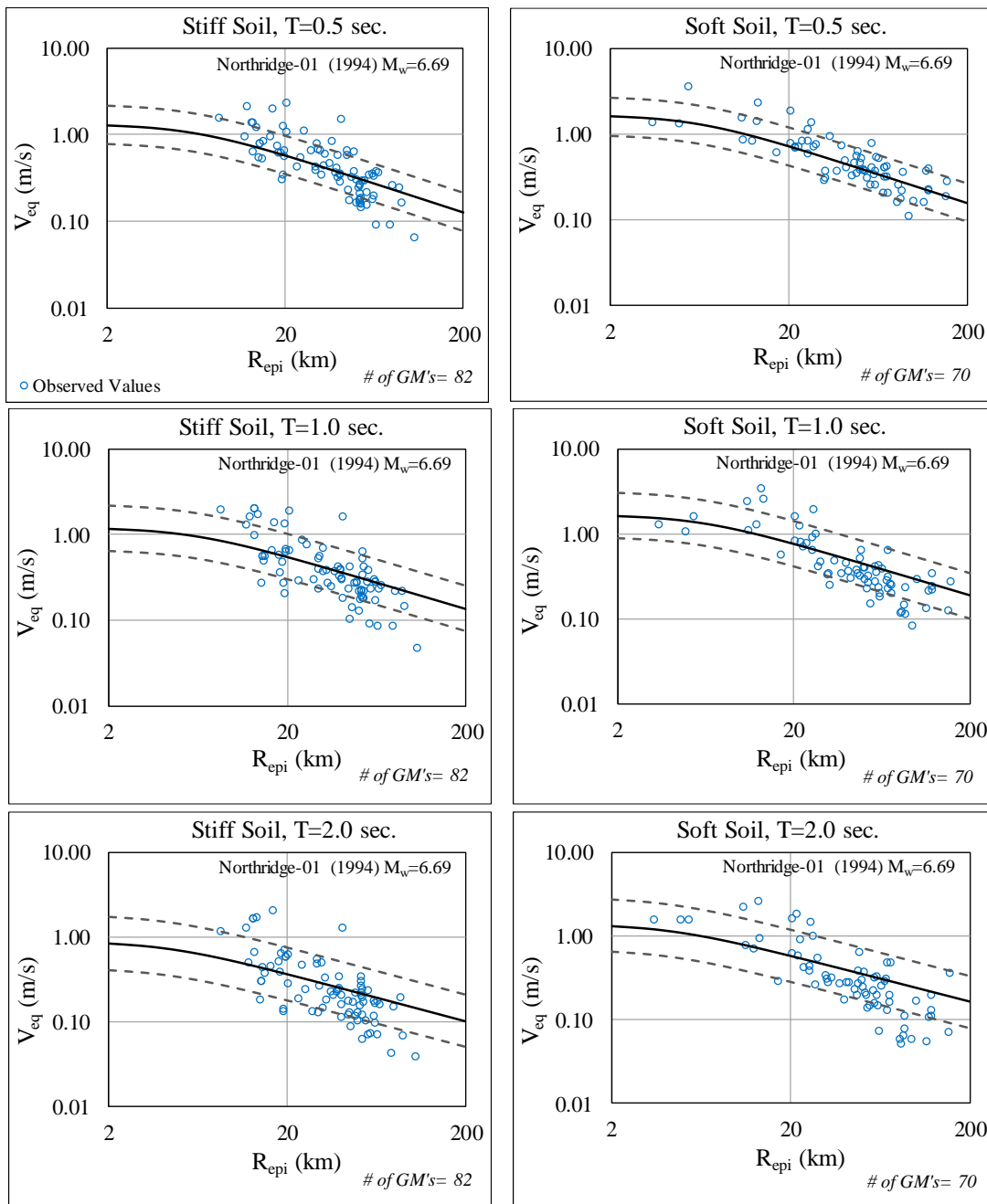


Figure 3.7. Comparison of the computed V_{eq} with the mean and mean \pm one standard deviations of the prediction model for $M_w=6.69$ Northridge-01 (1994) earthquake, for stiff and soft soil types

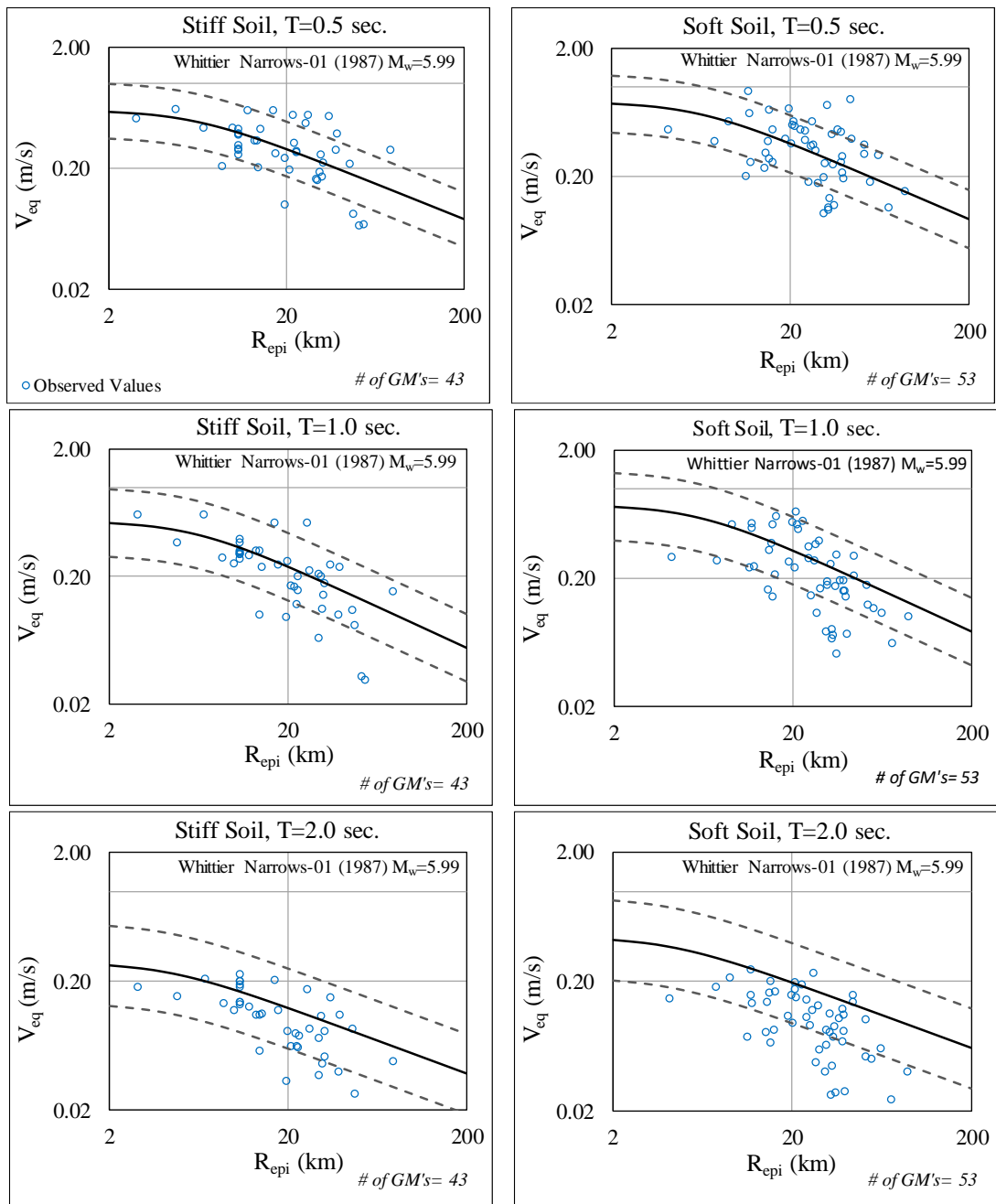


Figure 3.8. Comparison of the computed V_{eq} with the mean and mean \pm one standard deviations of the prediction model for $M_w=5.99$ Whittier Narrows-01 (1987) earthquake, for stiff and soft soil types

Mean V_{eq} spectra of ground motions selected from the Northridge-01 ($M_w=6.69$) and Chi-Chi ($M_w=7.62$) earthquakes are estimated by the prediction equation developed in

this study. The range of distances for the selected records are 17 - 23 km for the Northridge-01 (1994) and 48 - 51 km for the Chi-Chi (1999) earthquakes. The computed V_{eq} spectra of the selected ground motions from these two earthquakes are shown in Figure 3.9 and Figure 3.10 for stiff and soft soil types, along with their mean spectra and the estimated mean spectra from the proposed prediction model. The middle values of the R_{epi} bands of the records for each earthquake and each soil type are used for calculating the estimated mean spectra. It can be observed from these figures that the mean spectra estimated by the proposed prediction model predicts the computed mean spectra with fairly good accuracy.

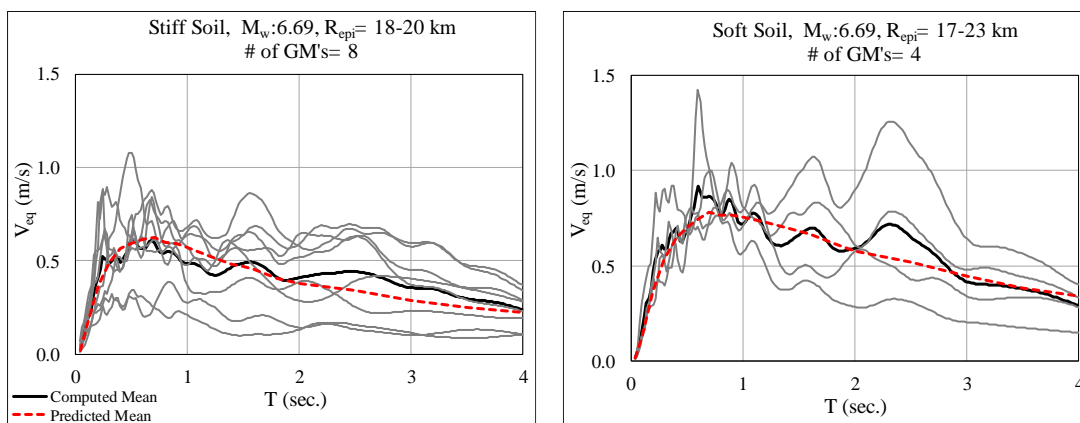


Figure 3.9. V_{eq} spectra of ground motions selected from Northridge-01 (1994) earthquake and the comparison of their mean spectra with the estimated mean from Equation 3.6

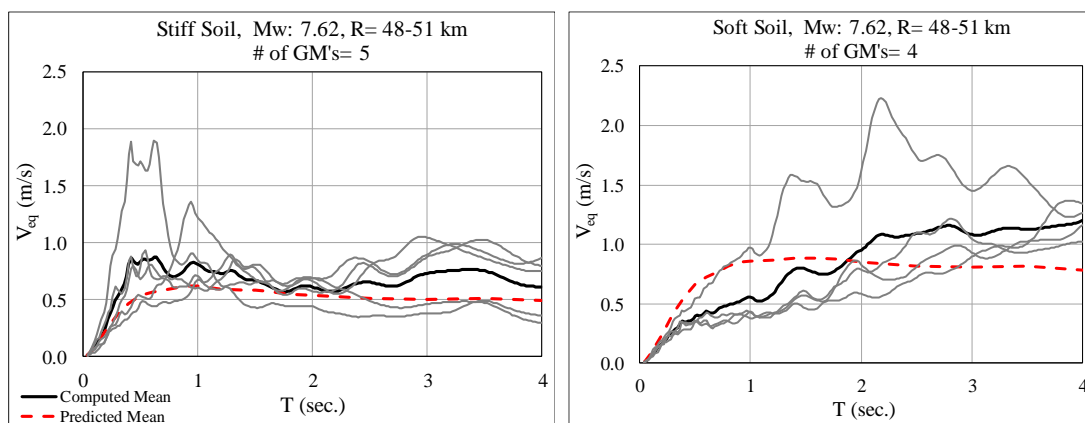


Figure 3.10. V_{eq} spectra of ground motions selected from Chi-Chi (1999) earthquake and the comparison of their mean spectra with the estimated mean from Equation 3.6

The prediction models proposed by Chapman (1999) and Cheng et al. (2014), and the input energy design spectra proposed by Benavent-Climent et al. (2002) are also used to estimate the mean V_{eq} spectra of the selected ground motions, and compared with the results of the model developed herein.

Chapman (1999) investigated the use of elastic input energy in seismic hazard analysis by using 304 ground motion records from 23 earthquakes that occurred in Western North America, and calculated elastic input energy equivalent velocity V_{eq} spectra for periods from 0.1 to 2.0 seconds by using the prediction model developed by Boore et al. (1993, 1997). Chapman's prediction model employed Joyner-Boore distance measure R_{JB} instead of epicentral distance R , and the effect of fault mechanism is not considered.

Cheng et al. (2014) also established an input energy prediction equation based on the prediction model developed by Boore et al. (1993, 1997) by using 1,550 ground motions from 63 earthquakes. They obtained regression parameters for both absolute and relative input energy velocities separately. Their model accounts for the fault mechanism, and considers V_{S30} in order to capture the site response effect more adequately in the prediction of input energy where the distance measure R is the closest distance to the ruptured fault.

Benavent-Climent et al. (2002) derived a 10 percent damped bilinear design input energy spectra for low to moderate seismicity regions by considering 100 ground motions obtained from 48 earthquakes recorded in Spain. The corner periods of the bilinear spectra are 0.24 and 0.40 seconds for stiff and soft soils, respectively. The ordinate of the flat part depends on the 84-percentile PGA of the considered ground motions where the two GM components are combined by SRSS. A scaling factor mentioned in Akkar and Bommer (2007b) is applied for converting the 10 percent damped spectral values to 5 percent damped values, and they are further divided by $\sqrt{2}$ for converting the SRSS combined horizontal components to geometric mean for the comparisons presented below.

The mean V_{eq} spectra of the records from the M_w 6.69 Northridge (1994) and M_w 7.62 Chi-Chi (1999) earthquakes, recorded approximately at 20 km and 50 km fault distances, are estimated by the prediction model proposed in this thesis study. Then the models proposed by Chapman(1999), Cheng et al. (2014), and the design spectra proposed by Benavent-Climent et al. (2002) for stiff and soft soil types separately are employed for estimating V_{eq} spectra. In calculating the bilinear V_{eq} design spectra proposed by Benavent-Climent et al. (2002), the mean PGA values of the selected records for each earthquake and each soil type are employed, which are 0.28g and 0.31g for stiff and soft soil types in Northridge-01 (1994), and 0.22g and 0.08g for the stiff and soft soil types in Chi-Chi (1999) earthquakes, respectively. The comparisons of the estimated mean spectra and the computed mean spectra of ground motions for each earthquake and soil type are shown in Figure 3.11 and Figure 3.12. These figures reveal that different prediction models display similar spectral variations despite some differences for the two earthquakes. Strong dependence of the Benavent-Climent et al. (2002) model on PGA seems to be an over simplification. Chapman (1999) model works quite well for the ground motions from the Western North American earthquake Northridge 1994, which is included in the regression database, whereas the model overestimates the energy of Chi-Chi ground motions in the 0-2 second period range considered in regression analysis.

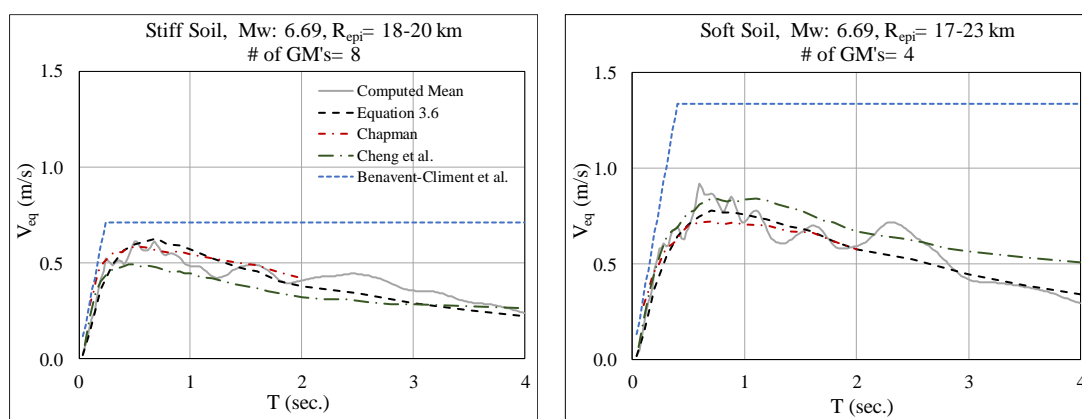


Figure 3.11. Comparison of the estimated mean spectra from several studies with the mean spectra of ground motion records selected from the Northridge-01 (1994) earthquake

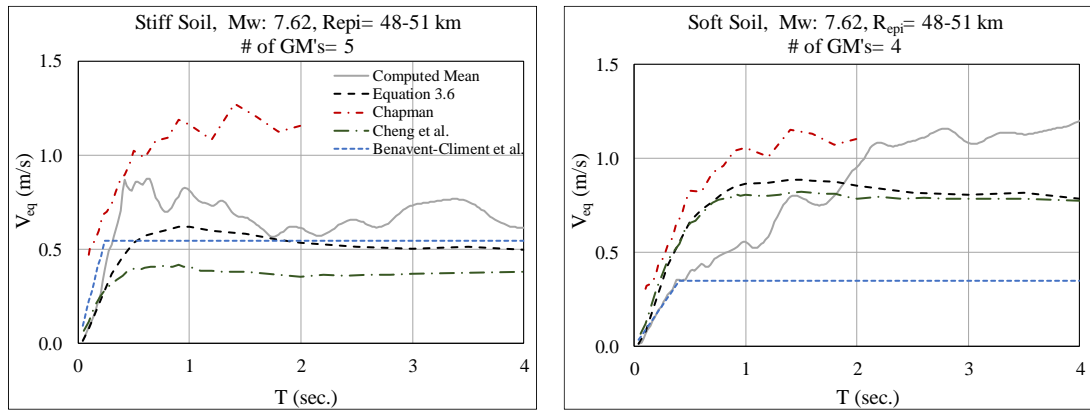


Figure 3.12. Comparison of the estimated mean spectra from several studies with the mean spectra of ground motion records selected from the Chi-Chi (1999) earthquake

The sensitivity of V_{eq} spectra to magnitude, distance and fault type is assessed by utilizing the developed model for three magnitudes, three fault distances and three fault types, which are presented comparatively in Figure 3.13, Figure 3.14 and Figure 3.15.

It can be observed from Figure 3.13, Figure 3.14 and Figure 3.15 that reverse and strike-slip faults impose 50 to 70% higher energy demands (V_{eq}^2) compared to normal faults. The effect of soil type is more prominent at larger magnitudes ($M_w 6.5$ and 7.5) where ground motions on soft soils are significantly more energy demanding than those on stiff sites. The soft-to-stiff V_{eq} ratio is about 1.5 for $M_w 7.5$ and 1.35 for $M_w 6.5$. Furthermore, energy demand from large earthquakes ($M_w 7.5$) do not fall off with period regardless of the fault distances. This is perhaps a crucial observation which reveals that energy-based approaches are primarily worthwhile for longer period structures ($T > 1$ s) where seismicity is dominated by major faults which can produce large magnitude earthquakes. Moderate ($M_w 6.5$) to small magnitude ($M_w 5.5$) earthquakes impose highest energy demands on the short to medium period structures where $T < 1$ s.

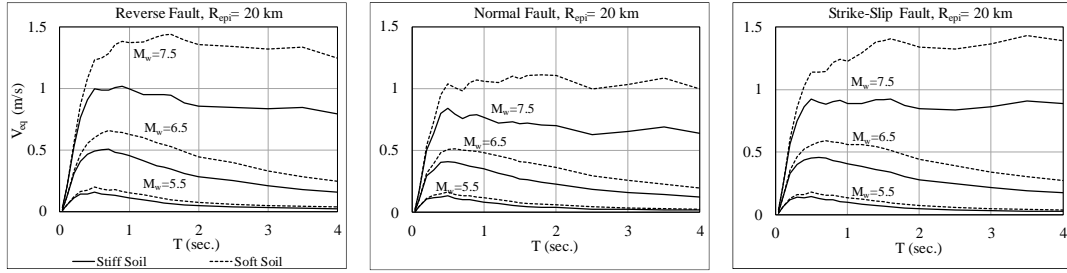


Figure 3.13. Variation of input energy spectra V_{eq} with earthquake magnitude obtained from the prediction model for different soil types and fault mechanisms at $R_{epi}=20$ km.

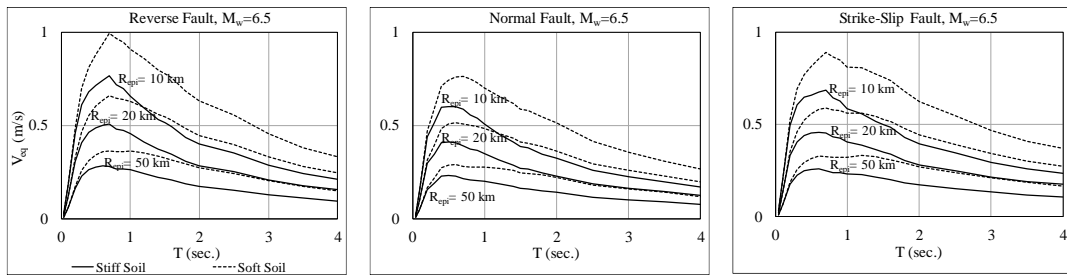


Figure 3.14. Variation of input energy spectra V_{eq} with epicentral distance obtained from the prediction model for different soil types and fault mechanisms, $M_w=6.5$.

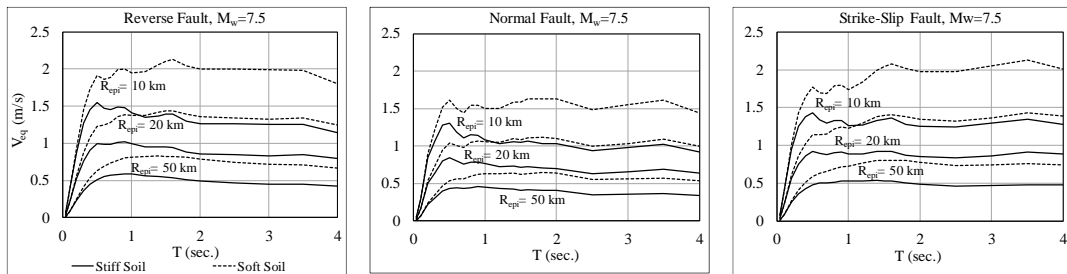


Figure 3.15. Variation of input energy spectra V_{eq} with epicentral distance obtained from the prediction model for different soil types and fault mechanisms, $M_w=7.5$.

3.4. Input Energy Prediction By Developing Scaling Relations Between PS_V and V_{eq}

Housner (1956) suggested in early 1950's that the velocity spectra can be considered as an intensity measure of the ground motion in terms of energy, where the amount of

energy dissipated by the system is equal to the difference between the total input energy and the elastic strain energy. This observation was confirmed by Akiyama (1985), except in the very short period range. Hudson (1956) has also noticed in these years that the velocity spectrum of a ground motion record is a consistent measure of the maximum energy demand from structures. The correlation of elastic input energy spectrum, expressed in terms of V_{eq} , with the pseudo velocity spectrum PS_V is investigated herein. Magnitude, distance, soil type, period and damping ratio dependence of the V_{eq}/PS_V ratio is evaluated. For this purpose, V_{eq}/PS_V spectra for 5% damping are computed for the ground motions from Chi-Chi (1999), Hector Mine (1999), Loma Prieta (1989), Northridge-01 (1994) and Whittier Narrows-01 (1987) earthquakes, for stiff and soft sites separately. The V_{eq}/PS_V spectra computed for the ground motions from five earthquakes are shown in Figure 3.16. It can be observed from each box in Figure 3.16 that the record-to-record variability of the V_{eq}/PS_V ratio for ground motions from the same earthquake on similar soil type, but from different distances are small. Moreover, mean spectra of ground motions in each box are quite similar for the five earthquakes and two soil types, which motivates the consideration of V_{eq}/PS_V spectrum as independent from magnitude, distance and soil type. This is somewhat expected since the effects of these parameters on V_{eq} and PS_V are quite similar. There is a difference for Whittier Narrows-01 (1987) earthquake however, where the V_{eq}/PS_V spectra displays an increasing trend for $T > 2$ seconds.

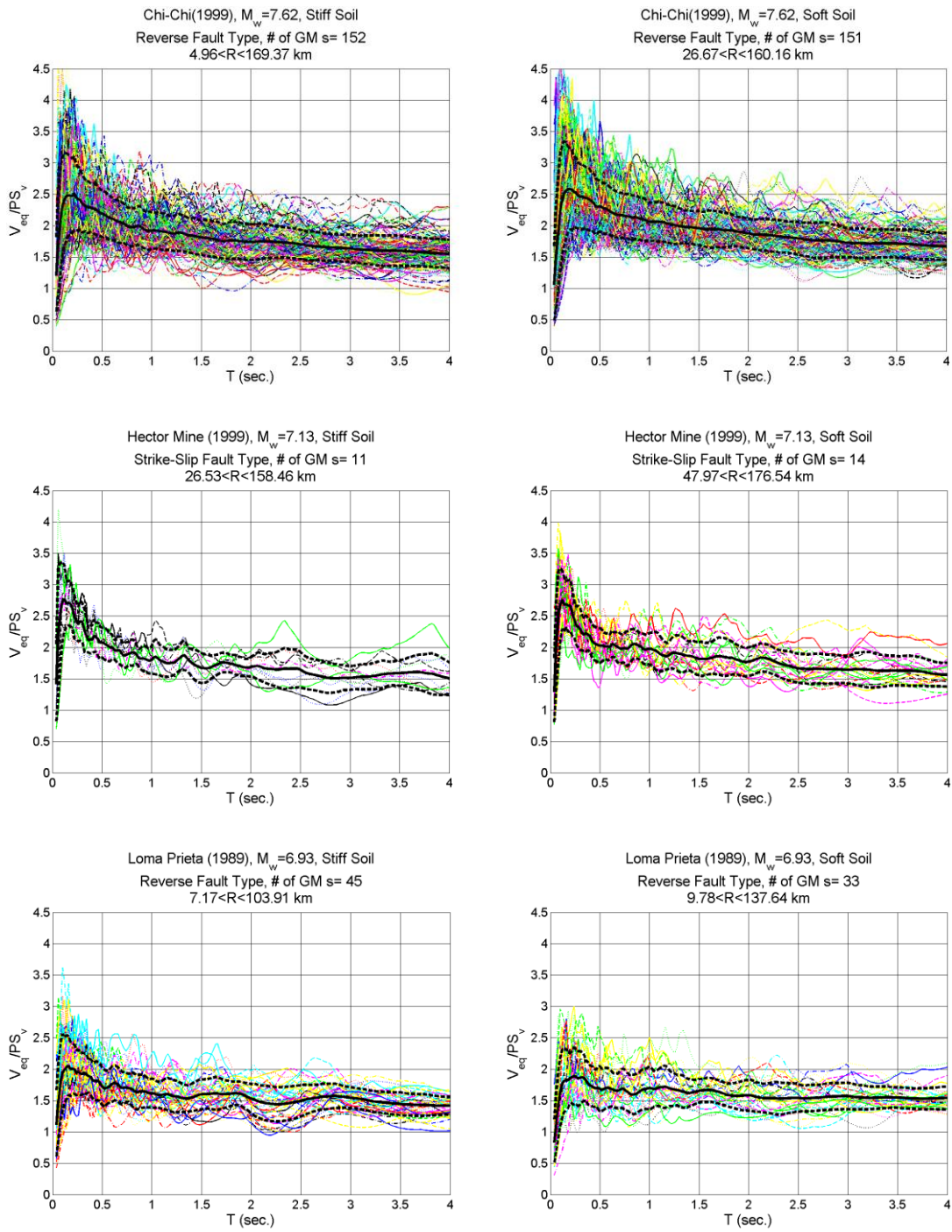


Figure 3.16. Spectral variations of 5 percent damped V_{eq}/PS_V ratio for GM's from Chi-Chi (1999), Hector Mine (1999), Loma Prieta (1989), Northridge-01 (1994) and Whittier Narrows-01 (1987) earthquakes on stiff and soft sites, along with their mean (solid) and mean \pm sigma (dashed) spectra

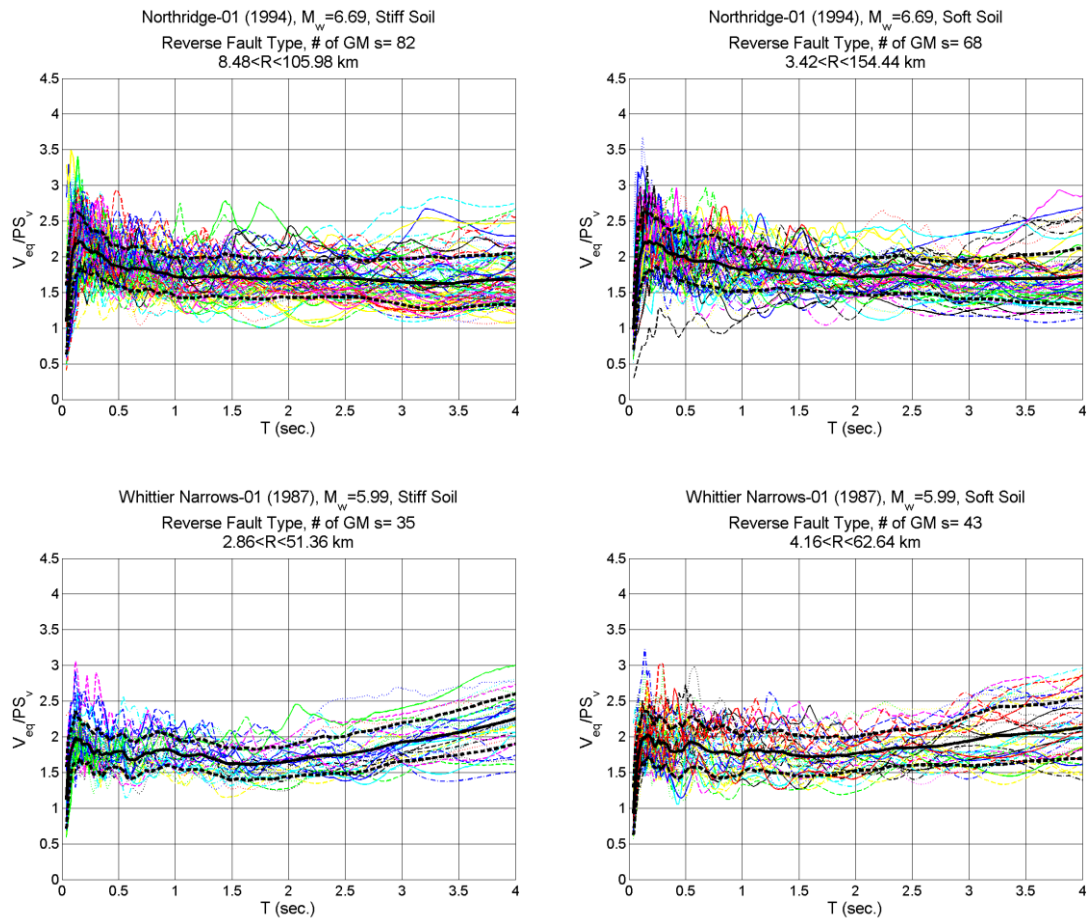


Figure 3.16. (Continued)

For further investigation of the sensitivity of V_{eq}/PS_V spectrum to magnitude and soil type, mean spectral curves of the ground motions from each earthquake and each soil type are compared in Figure 3.17. There is no consistently noticeable effect of magnitude and soil type on V_{eq}/PS_V spectra in Figure 3.17. Past studies have showed that V_{eq}/PS_V is mainly influenced by the fraction of inherent damping of the structure (Chapman 1999, Akiyama 1985). In order evaluate the dependence on damping, the mean V_{eq}/PS_V spectra for 2% and 10% damping ratios of ground motions in the database are computed and compared with the 5% damped spectra in Figure 3.18. As it was expected that with increased damping PS_V values decreases, and the obtained V_{eq}/PS_V ratios increases as in Figure 3.18, since spectral input energy values does not

vary much with the damping ratio, but get smoother for higher damping ratios (Nurtuğ and Sucuoğlu 1995). Hence, V_{eq}/PS_V spectrum can be idealized by a simple function of T only for a selected damping value. The exponential model in Equation 3.8 is used for expressing this idealization where the coefficients a , b and c are all functions of vibration period. The undetermined coefficients in Equation 3.8 were obtained by regression analysis, by employing V_{eq} and PS_V spectra of ground motions in the database for 2%, 5% and 10% damping ratios, separately. They are presented in Table 3.4. Figure 3.19 also shows the variation of these coefficients with period for three damping values.

$$V_{eq}/PS_V = a \cdot e^{-bT} + c \quad (3.8)$$

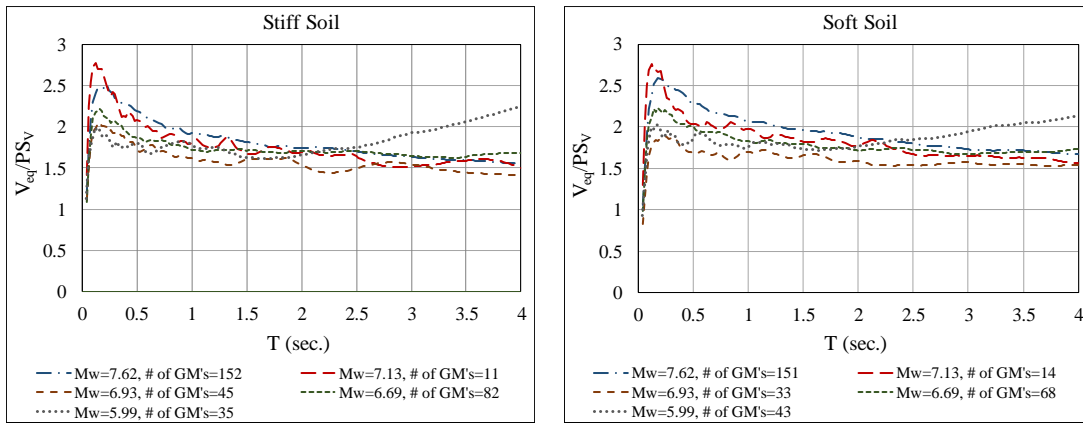


Figure 3.17. Comparison of the mean 5 percent damped V_{eq}/PS_V ratios of ground motions from the selected earthquakes for stiff and soft soil types.

Once the V_{eq}/PS_V spectrum is estimated from Equation 3.8 and Table 3.4 for the selected damping ratio, input energy demand on a SDOF system can be calculated by scaling the corresponding PS_V spectra with the spectral V_{eq}/PS_V ratio. The mean V_{eq}/PS_V spectrum estimated from Equation 3.8 and Table 3.4 for 5% damping is compared with the mean computed V_{eq}/PS_V spectrum of all ground motions in Figure 3.20(a). Mean \pm sigma variation of the computed V_{eq}/PS_V spectra are also presented in Figure 3.20(a). In addition, the mean V_{eq}/PS_V spectra estimated for three damping

ratios are presented in Figure 3.20(b). It is observed that the estimated and the computed mean spectra match almost exactly.

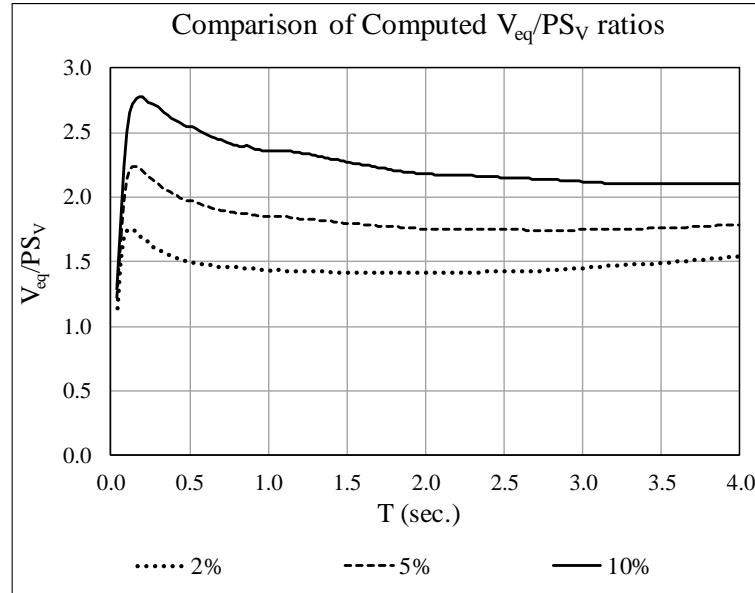


Figure 3.18. Comparison of the mean 5 percent damped V_{eq}/PS_V spectra with the mean 2 and 10 percent damped spectra for the ground motions in the database

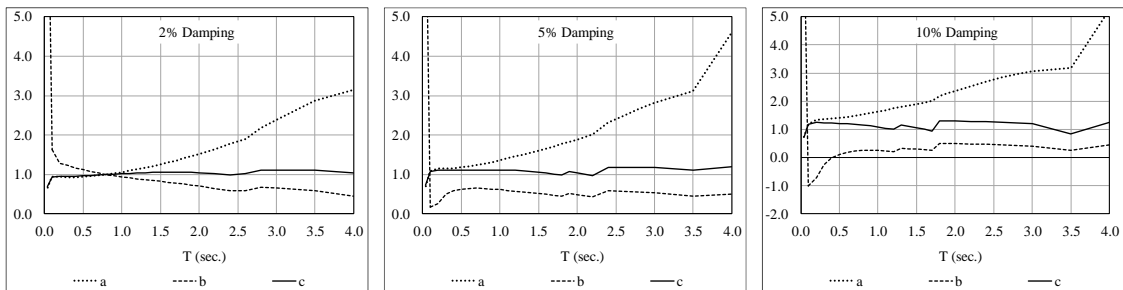


Figure 3.19. Variation of the coefficients of model equation with period for different damping ratios

Table 3.4. Coefficients for the model equation of V_{eq}/PS_V versus T for different damping ratios

T (sec.)	2% Damping			5% Damping			10% Damping		
	a	b	c	a	b	c	a	b	c
0.04	0.6662	9.8456	0.6913	0.7066	8.6722	0.7266	0.7321	7.9524	0.7493
0.1	0.9367	1.6342	0.9429	1.0832	0.1650	1.0750	1.1973	-1.0100	1.1740
0.2	0.9433	1.2842	0.9536	1.1458	0.2638	1.1178	1.3265	-0.7183	1.2435
0.3	0.9300	1.2340	0.9483	1.1501	0.4944	1.1097	1.3555	-0.2593	1.2340
0.4	0.9325	1.1691	0.9549	1.1598	0.5955	1.1055	1.3752	-0.0035	1.2190
0.5	0.9402	1.1199	0.9638	1.1831	0.6280	1.1087	1.4110	0.1088	1.2077
0.6	0.9573	1.0712	0.9766	1.2082	0.6457	1.1110	1.4459	0.1828	1.1932
0.7	0.9710	1.0415	0.9856	1.2369	0.6524	1.1130	1.4837	0.2275	1.1759
0.8	1.0037	0.9954	1.0016	1.2730	0.6464	1.1158	1.5229	0.2559	1.1551
0.9	1.0296	0.9671	1.0120	1.3155	0.6323	1.1178	1.5766	0.2511	1.1257
1.0	1.0552	0.9447	1.0203	1.3565	0.6211	1.1164	1.6276	0.2466	1.0891
1.1	1.0924	0.9157	1.0306	1.4106	0.5953	1.1140	1.6896	0.2214	1.0344
1.2	1.1313	0.8897	1.0391	1.4566	0.5797	1.1065	1.7446	0.2203	1.0020
1.3	1.1674	0.8695	1.0448	1.5068	0.5595	1.0955	1.7956	0.3269	1.1461
1.4	1.2090	0.8475	1.0500	1.5570	0.5395	1.0804	1.8470	0.3170	1.1108
1.5	1.2509	0.8276	1.0534	1.6061	0.5204	1.0613	1.8981	0.3048	1.0685
1.6	1.3005	0.8039	1.0563	1.6614	0.4945	1.0354	1.9527	0.2860	1.0146
1.7	1.3420	0.7872	1.0562	1.7156	0.4697	1.0040	2.0076	0.2650	0.9492
1.8	1.4065	0.7556	1.0563	1.7741	0.4506	0.9811	2.1992	0.4910	1.2982
1.9	1.4579	0.7336	1.0529	1.8255	0.5150	1.0735	2.2743	0.4911	1.2947
2.0	1.5162	0.7071	1.0470	1.8840	0.4908	1.0477	2.3548	0.4890	1.2922
2.2	1.6390	0.6491	1.0246	2.0144	0.4259	0.9634	2.5288	0.4784	1.2888
2.4	1.7752	0.5871	0.9892	2.3087	0.5874	1.1859	2.6919	0.4666	1.2793
2.6	1.9016	0.5966	1.0219	2.4826	0.5719	1.1844	2.8431	0.4501	1.2640
2.8	2.1786	0.6777	1.1070	2.6554	0.5541	1.1805	2.9707	0.4280	1.2383
3.0	2.3907	0.6510	1.1119	2.8201	0.5319	1.1734	3.0649	0.3998	1.1945
3.5	2.8736	0.5813	1.1102	3.1056	0.4451	1.1053	3.1822	0.2616	0.8325
4.0	3.1446	0.4549	1.0317	4.6007	0.5093	1.1877	5.2470	0.4583	1.2609

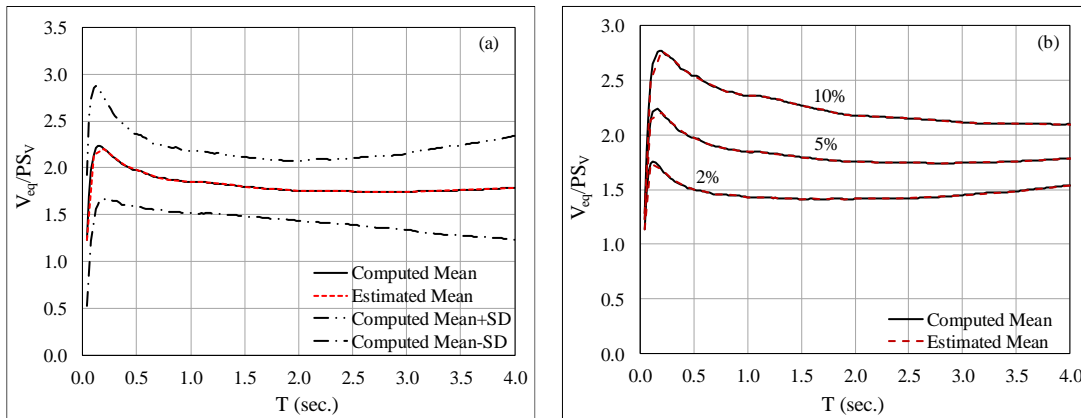


Figure 3.20. (a) Comparison of the estimated mean with the computed mean, and mean \pm sigma V_{eq}/PS_V spectra of all ground motions in the database for 5 percent damping. (b) Comparison of the estimated and computed mean V_{eq}/PS_V spectra for 2, 5 and 10 percent damping

The damping scaling factors given in Eurocode 8 (1994) (Equation 1.5) and FEMA440 (2005) (Equation 6.17) can be employed to obtain the spectral ordinates at damping values different from 5 percent. These factors are applied in order to estimate the V_{eq}/PS_V spectra for 2 and 10 percent damping values from the 5 percent damped spectra obtained from Equation 3.8 and Table 3.4. The 2 and 10 percent damped V_{eq}/PS_V spectra estimated by applying the damping scaling factors are shown in Figure 3.21 and compared with the spectra calculated from the model equation, i.e. Equation 3.8. It is observed that damping scaling is acceptable.

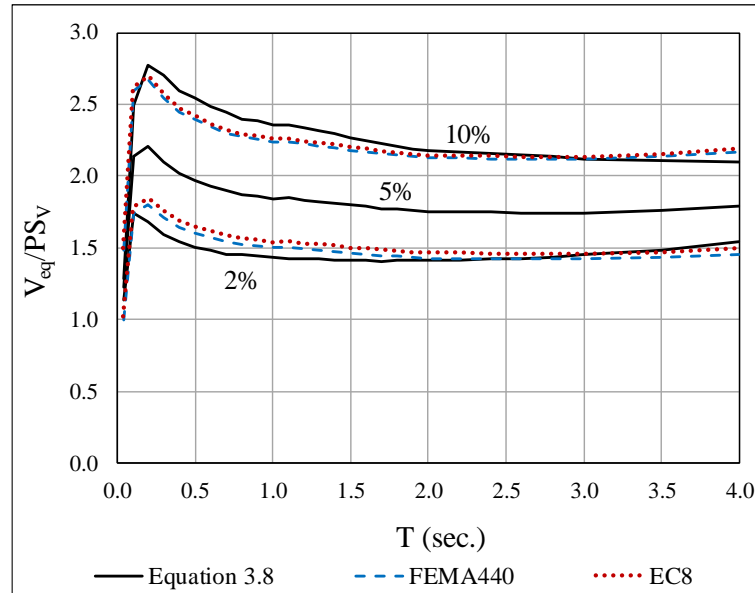


Figure 3.21. Comparison of the V_{eq}/PS_V spectra obtained from the 5 percent damped V_{eq}/PS_V spectrum according to EC8 and FEMA440 damping scaling, with the spectra obtained from this study for 2 and 10 percent damping

Probabilistic seismic hazard maps are now available for many seismic regions in the World, including United States and Turkey. These maps and the associated seismic design guidelines provide linear elastic acceleration design spectra for a geographical location, for several return periods or probabilities of exceeding a given spectral acceleration intensity parameter, which leads to uniform hazard spectrum. Converting a design acceleration spectrum to pseudo velocity spectrum for a given damping ratio

is a standard practice. Then the input energy spectrum in the probabilistic hazard family can be obtained by applying the spectral scaling ratio V_{eq}/PS_V derived above, to the PS_V spectrum.

A high seismic intensity location was selected in the United States, and the 5 percent damped acceleration design spectra based on NEHRP (2015) provisions (2/3 of the 2475-year spectrum) were obtained for stiff (C) and soft (D) soil types, as shown in Figure 22. Then ground motions were selected from the NGA database where 0.2 and 1 second period spectral accelerations were sufficiently close to the NEHRP design spectra for stiff and soft soil types. Figure 3.22 shows the NEHRP design spectra and the acceleration spectra of the selected earthquake ground motions along with their mean spectra for each soil type separately. It is also obvious that the mean spectra of the selected earthquake ground motions for both soil types are very close to the NEHRP acceleration design spectra.

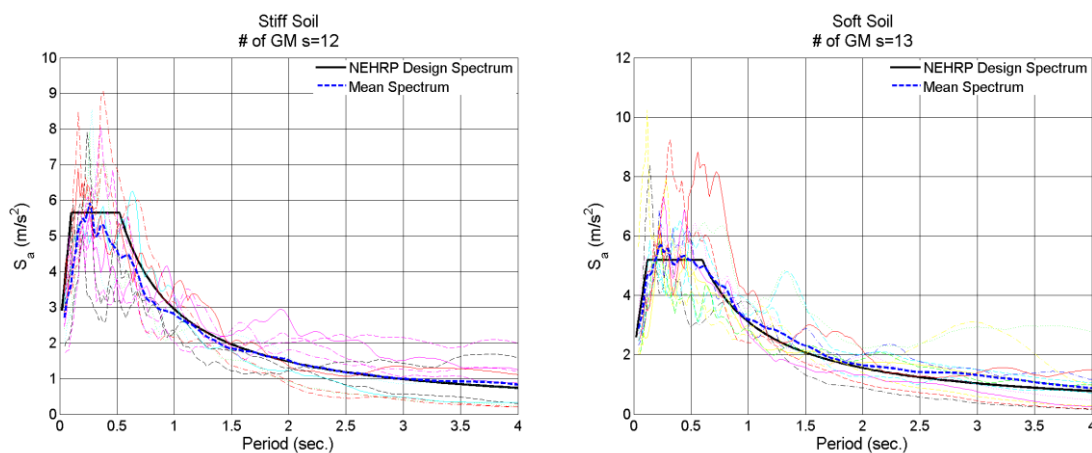


Figure 3.22. 5 percent damped design acceleration spectra based on NEHRP provisions, and acceleration spectra of the selected ground motions along with their mean spectrum

After calculating PS_V spectra from the associated NEHRP 5 percent damped acceleration design spectra given in Figure 3.22 for each soil type, V_{eq} values were obtained by using Equation 3.8 and the coefficients for 5 percent damping given in Table 3.4. The comparison of the V_{eq} design spectra obtained by scaling the NEHRP

design spectra and the mean V_{eq} spectra of the selected (spectrum compatible) GM records are shown in Figure 3.23 . It can be observed that the design V_{eq} spectra based on NEHRP provisions exhibit a good agreement with the mean spectra of the selected GM records along the entire period range.

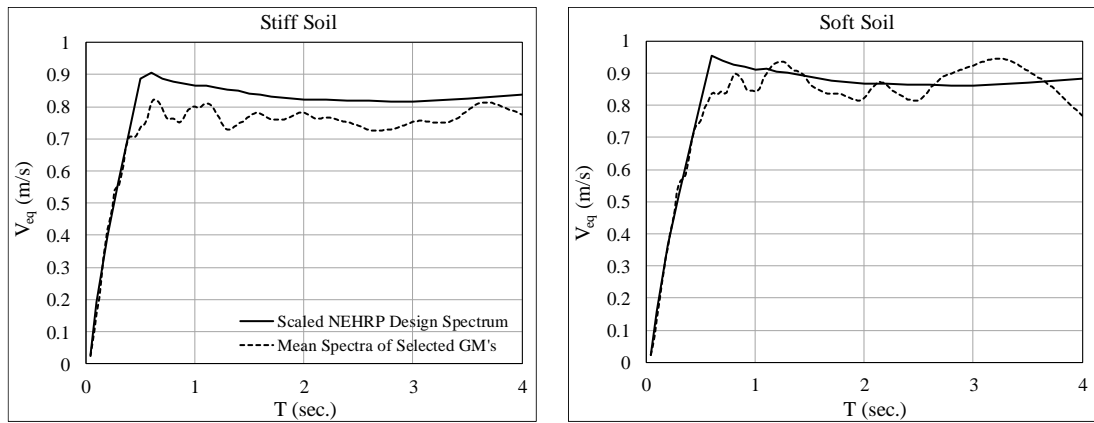


Figure 3.23. Scaled V_{eq} spectra based on NEHRP design acceleration spectra, and its comparison with the mean spectra of the selected (spectrum compatible) ground motions

CHAPTER 4

ELASTIC AND INELASTIC NEAR-FAULT INPUT ENERGY SPECTRA

The main purpose of this chapter is to develop a reliable model for predicting the input energy spectra of near-fault ground motions for linear elastic and inelastic systems, and to evaluate the effect of damping and lateral strength on energy dissipation demands. A prediction model has been developed through one-stage nonlinear regression analysis. Comparative results revealed that near-fault ground motions have significantly larger energy dissipation demands, which are very sensitive to earthquake magnitude and soil type. The effect of damping on elastic and inelastic near fault input energy spectra is insignificant. Near fault input energy spectra for inelastic systems is dependent on lateral strength ratio R_μ for short period systems, however, there is almost no dependency on lateral strength for intermediate and long period systems, recalling an equal energy rule. This is a significant advantage for an energy-based design approach.

4.1. Near-Fault Ground Motions

A batch of 157 near-fault ground motion (GM) accelerograms with two horizontal components, each representing free field motion, is selected in order to study the near-fault effects on seismic input energy. This batch is a subset of the ground motion database employed in Chapter 3 that was compiled from Next Generation Attenuation Project database. The database for this part includes GM records which were recorded at epicentral distances not longer than 30 km, and at distances shorter or equal to the associated rupture lengths. Besides, these GM records were recorded at closest distances not longer than 25 km. The moment magnitudes (M_w) of earthquakes producing these ground motions ranges from 5.69 to 7.62. Figure 4.1 shows the M_w versus R_{epi} scatter diagram for the ground motions in the database. Additionally, Table

4.1 presents the distribution of records in the compiled GM batch with respect to shear wave velocity of the upper 30 meters of soil profile (V_{S30}) according to NEHRP site classification. Similar to the previous chapter, ground motion sites in the database with V_{S30} values larger than the limiting value of 360 m/s (NEHRP A, B and C) are designated as stiff soil type, whereas those with lower V_{S30} values (NEHRP D and E) are specified as soft soil type. The properties of earthquake ground motions are given in Table 4.2. In the foregoing analysis in this part, the input energy spectrum of each ground motion in the database is calculated separately for both horizontal components by integrating the equation of motion over time, defined in relative energy terms for the associated SDOF system. Then the input energy spectrum of ground motion is obtained as the geometric mean of the two horizontal ground motion components (Equation 3.4) where spectral ordinates are obtained either in terms of input energy E_i (Joule, J) for a unit mass, or in terms of energy equivalent velocity V_{eq} (cm/s) where $V_{eq} = \sqrt{2E_i/m}$ (Equation 3.3).

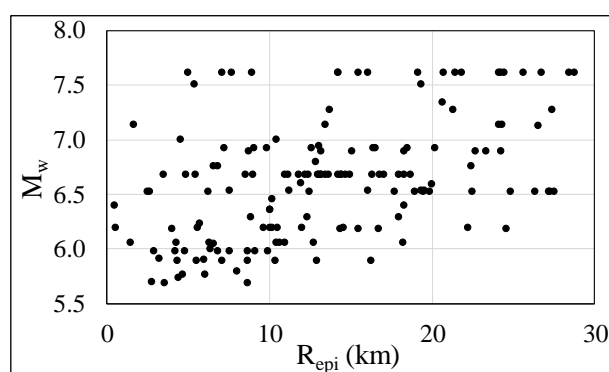


Figure 4.1. Magnitude - distance distribution of the near-fault ground motions used in this chapter

Table 4.1. Distribution of ground motions with respect to V_{S30}

V_{S30} Range (m/s)	NEHRP Classification	# of Records
<180	E	-
180-360	D	65
360-760	C	88
760-1500	B	3
>1500	A	1

Table 4.2. *The list of earthquake ground motions*

Earthquake Name	Year	Station Name	M_w	Fault Mech.*	Depth (km)	Fault Rup. Length (km)	R_{epi} (km)	Soil Type Based on V_{S30}
Big Bear-01	1992	Big Bear Lake - Civic Center	6.46	0	13	17.00	10.15	D
Cape Mendocino	1992	Petrolia	7.01	2	9.6	20.00	4.51	C
Cape Mendocino	1992	Cape Mendocino	7.01	2	9.6	20.00	10.36	C
Chalfant Valley-02	1986	Zack Brothers Ranch	6.19	0	10	15.00	14.33	D
Chalfant Valley-02	1986	Bishop - Paradise Lodge	6.19	0	10	15.00	15.42	D
Chi-Chi, Taiwan	1999	TCU078	7.62	3	6.76	88.00	4.96	C
Chi-Chi, Taiwan	1999	TCU089	7.62	3	6.76	88.00	7.04	C
Chi-Chi, Taiwan	1999	TCU079	7.62	3	6.76	88.00	7.64	C
Chi-Chi, Taiwan	1999	TCU084	7.62	3	6.76	88.00	8.91	C
Chi-Chi, Taiwan	1999	WNT	7.62	3	6.76	88.00	14.16	C
Chi-Chi, Taiwan	1999	TCU129	7.62	3	6.76	88.00	14.16	C
Chi-Chi, Taiwan	1999	TCU071	7.62	3	6.76	88.00	15.42	C
Chi-Chi, Taiwan	1999	TCU076	7.62	3	6.76	88.00	16.03	C
Chi-Chi, Taiwan	1999	TCU074	7.62	3	6.76	88.00	19.08	C
Chi-Chi, Taiwan	1999	TCU075	7.62	3	6.76	88.00	20.67	C
Chi-Chi, Taiwan	1999	TCU072	7.62	3	6.76	88.00	21.42	C
Chi-Chi, Taiwan	1999	TCU122	7.62	3	6.76	88.00	21.80	C
Chi-Chi, Taiwan	1999	CHY024	7.62	3	6.76	88.00	24.10	C
Chi-Chi, Taiwan	1999	TCU138	7.62	3	6.76	88.00	24.22	C
Chi-Chi, Taiwan	1999	TCU116	7.62	3	6.76	88.00	24.41	C
Chi-Chi, Taiwan	1999	TCU120	7.62	3	6.76	88.00	25.57	C
Chi-Chi, Taiwan	1999	TCU065	7.62	3	6.76	88.00	26.67	D
Chi-Chi, Taiwan	1999	TCU110	7.62	3	6.76	88.00	28.38	D
Chi-Chi, Taiwan	1999	TCU067	7.62	3	6.76	88.00	28.70	C
Chi-Chi, Taiwan-02	1999	TCU074	5.90	2	8	19.00	5.49	C
Chi-Chi, Taiwan-02	1999	TCU073	5.90	2	8	19.00	10.30	D
Chi-Chi, Taiwan-02	1999	TCU084	5.90	2	8	19.00	12.88	C
Chi-Chi, Taiwan-02	1999	TCU079	5.90	2	8	19.00	16.24	C
Chi-Chi, Taiwan-03	1999	TCU078	6.20	2	8	10.00	0.51	C
Chi-Chi, Taiwan-03	1999	TCU079	6.20	2	8	10.00	5.57	C
Chi-Chi, Taiwan-03	1999	TCU084	6.20	2	8	10.00	9.57	C
Chi-Chi, Taiwan-03	1999	TCU089	6.20	2	8	10.00	10.45	C
Chi-Chi, Taiwan-04	1999	CHY074	6.20	0	18	21.50	10.10	C
Chi-Chi, Taiwan-04	1999	CHY080	6.20	0	18	21.50	14.51	C
Chi-Chi, Taiwan-04	1999	CHY028	6.20	0	18	21.50	22.19	C
Chi-Chi, Taiwan-06	1999	TCU080	6.30	2	16	29.00	8.80	C
Chi-Chi, Taiwan-06	1999	TCU079	6.30	2	16	29.00	12.26	C
Chi-Chi, Taiwan-06	1999	TCU078	6.30	2	16	29.00	17.94	C
Coalinga-01	1983	Pleasant Valley P.P. - bldg	6.36	2	4.6	16.00	9.98	D
Coalinga-01	1983	Pleasant Valley P.P. - yard	6.36	2	4.6	16.00	9.98	D
Coalinga-05	1983	Oil City	5.77	2	7.4	5.96	4.60	C
Coalinga-05	1983	Transmitter Hill	5.77	2	7.4	5.96	5.99	C
Corinth, Greece	1981	Corinth	6.60	1	7.15	37.00	19.92	D
Coyote Lake	1979	Gilroy Array #6	5.74	0	9.6	6.60	4.37	C
Dinar, Turkey	1995	Dinar	6.40	1	5	12.60	0.44	D

Table 4.2 (Continued)

Earthquake Name	Year	Station Name	M _w	Fault Mech.*	Depth (km)	Fault Rup. Length (km)	R _{epi} (km)	Soil Type Based on V _{S30}
Duzce, Turkey	1999	Duzce	7.14	0	10	46.80	1.61	D
Duzce, Turkey	1999	Lamont 1058	7.14	0	10	46.80	13.41	C
Duzce, Turkey	1999	Lamont 375	7.14	0	10	46.80	24.05	C
Duzce, Turkey	1999	Lamont 1059	7.14	0	10	46.80	24.26	C
Erzican, Turkey	1992	Erzincan	6.69	0	9	29.00	8.97	D
Gazli, USSR	1976	Karakyr	6.80	2	18.2	22.50	12.82	C
Hector Mine	1999	Hector	7.13	0	5	69.00	26.53	C
Helena, Montana-01	1935	Carroll College	6.00	0	6	7.76	6.31	C
Imperial Valley-02	1940	El Centro Array #9	6.95	0	8.8	63.00	12.99	D
Imperial Valley-06	1979	Aeropuerto Mexicali	6.53	0	9.96	50.00	2.47	D
Imperial Valley-06	1979	Agrarias	6.53	0	9.96	50.00	2.62	D
Imperial Valley-06	1979	Bonds Corner	6.53	0	9.96	50.00	6.20	D
Imperial Valley-06	1979	SAHOP Casa Flores	6.53	0	9.96	50.00	12.43	D
Imperial Valley-06	1979	Calexico Fire Station	6.53	0	9.96	50.00	17.65	D
Imperial Valley-06	1979	Chihuahua	6.53	0	9.96	50.00	18.88	D
Imperial Valley-06	1979	EC Meloland Overpass FF	6.53	0	9.96	50.00	19.44	D
Imperial Valley-06	1979	Holtville Post Office	6.53	0	9.96	50.00	19.81	D
Imperial Valley-06	1979	Compuertas	6.53	0	9.96	50.00	22.43	D
Imperial Valley-06	1979	Cerro Prieto	6.53	0	9.96	50.00	24.82	C
Imperial Valley-06	1979	El Centro Array #10	6.53	0	9.96	50.00	26.31	D
Imperial Valley-06	1979	El Centro Array #4	6.53	0	9.96	50.00	27.13	D
Imperial Valley-06	1979	El Centro Differential Array	6.53	0	9.96	50.00	27.23	D
Imperial Valley-06	1979	El Centro Array #6	6.53	0	9.96	50.00	27.47	D
Irpinia, Italy-01	1980	Calitri	6.90	1	9.5	47.00	15.04	C
Irpinia, Italy-01	1980	Bagnoli Irpinio	6.90	1	9.5	47.00	22.65	B
Irpinia, Italy-01	1980	Bisaccia	6.90	1	9.5	47.00	23.26	B
Irpinia, Italy-02	1980	Calitri	6.20	1	7	15.00	11.97	C
Kalamata, Greece-01	1986	Kalamata (bsmt)	6.20	1	5	12.30	9.97	D
Kobe, Japan	1995	Nishi-Akashi	6.90	0	17.9	60.00	8.70	C
Kobe, Japan	1995	Takatori	6.90	0	17.9	60.00	13.12	D
Kobe, Japan	1995	KJMA	6.90	0	17.9	60.00	18.27	D
Kobe, Japan	1995	Kakogawa	6.90	0	17.9	60.00	24.20	D
Kocaeli, Turkey	1999	Izmit	7.51	0	15	137.50	5.31	B
Kocaeli, Turkey	1999	Yarimca	7.51	0	15	137.50	19.30	D
Kozani, Greece-01	1995	Kozani	6.40	1	12.64	27.00	18.27	C
Landers	1992	Joshua Tree	7.28	0	7	71.70	13.67	C
Landers	1992	Morongo Valley	7.28	0	7	71.70	21.29	D
Landers	1992	Desert Hot Springs	7.28	0	7	71.70	27.33	D
Loma Prieta	1989	Corralitos	6.93	3	17.48	40.00	7.17	C
Loma Prieta	1989	BRAN	6.93	3	17.48	40.00	9.01	C
Loma Prieta	1989	Capitola	6.93	3	17.48	40.00	9.78	D
Loma Prieta	1989	WAHO	6.93	3	17.48	40.00	12.56	C
Loma Prieta	1989	UCSC Lick Observatory	6.93	3	17.48	40.00	16.34	C
Loma Prieta	1989	UCSC	6.93	3	17.48	40.00	16.51	C
Loma Prieta	1989	LGPC	6.93	3	17.48	40.00	18.46	C

Table 4.2 (Continued)

Earthquake Name	Year	Station Name	M _w	Fault Mech.*	Depth (km)	Fault Rup. Length (km)	R _{epi} (km)	Soil Type Based on V _{S30}
Loma Prieta	1989	San Jose - Santa Teresa Hills	6.93	3	17.48	40.00	20.13	C
Mammoth Lakes-01	1980	Convict Creek	6.06	4	9	15.00	1.43	D
Mammoth Lakes-01	1980	Mammoth Lakes H. S.	6.06	4	9	15.00	10.91	C
Mammoth Lakes-01	1980	Long Valley Dam (Upr L Abut)	6.06	4	9	15.00	12.65	D
Mammoth Lakes-02	1980	Mammoth Lakes H. S.	5.69	0	14	10.00	3.49	C
Mammoth Lakes-02	1980	Convict Creek	5.69	0	14	10.00	8.60	D
Mammoth Lakes-03	1980	Convict Creek	5.91	0	16	6.66	5.90	D
Mammoth Lakes-04	1980	Convict Creek	5.70	0	5	4.66	2.75	D
Managua, Nicaragua-01	1972	Managua, ESSO	6.24	0	5	11.50	5.68	D
Morgan Hill	1984	Halls Valley	6.19	0	8.5	27.00	3.94	D
Morgan Hill	1984	Anderson Dam (Downstream)	6.19	0	8.5	27.00	16.67	C
Morgan Hill	1984	Coyote Lake Dam (SW Abut)	6.19	0	8.5	27.00	24.55	C
N. Palm Springs	1986	Whitewater Trout Farm	6.06	3	11	20.00	4.24	D
N. Palm Springs	1986	Morong Valley	6.06	3	11	20.00	6.28	D
N. Palm Springs	1986	Desert Hot Springs	6.06	3	11	20.00	10.38	D
N. Palm Springs	1986	North Palm Springs	6.06	3	11	20.00	10.57	D
N. Palm Springs	1986	Cabazon	6.06	3	11	20.00	18.17	D
Nahanni, Canada	1985	Site 2	6.76	2	8	33.60	6.52	C
Nahanni, Canada	1985	Site 1	6.76	2	8	33.60	6.80	C
Nahanni, Canada	1985	Site 3	6.76	2	8	33.60	22.36	C
Norcia, Italy	1979	Cascia	5.90	1	6	8.71	4.29	C
Northridge-01	1994	Northridge - 17645 Saticoy St	6.69	2	17.5	18.00	3.42	D
Northridge-01	1994	Canoga Park - Topanga Can	6.69	2	17.5	18.00	4.85	D
Northridge-01	1994	Tarzana - Cedar Hill A	6.69	2	17.5	18.00	5.41	D
Northridge-01	1994	LA - Sepulveda VA Hospital	6.69	2	17.5	18.00	8.48	C
Northridge-01	1994	Rinaldi Receiving Sta	6.69	2	17.5	18.00	10.91	D
Northridge-01	1994	Arleta - Nordhoff Fire Sta	6.69	2	17.5	18.00	11.10	D
Northridge-01	1994	LA Dam	6.69	2	17.5	18.00	11.79	C
Northridge-01	1994	Simi Valley - Katherine Rd	6.69	2	17.5	18.00	12.18	C
Northridge-01	1994	Sun Valley - Roscoe Blvd	6.69	2	17.5	18.00	12.35	D
Northridge-01	1994	Jensen Filter Plant	6.69	2	17.5	18.00	12.97	C
Northridge-01	1994	Jensen Filter Plant Generator	6.69	2	17.5	18.00	13.00	C
Northridge-01	1994	Sylmar - Converter Sta	6.69	2	17.5	18.00	13.11	D
Northridge-01	1994	N Hollywood - Coldwater Can	6.69	2	17.5	18.00	13.12	C
Northridge-01	1994	Beverly Hills - 14145 Mulhol	6.69	2	17.5	18.00	13.39	D
Northridge-01	1994	Sylmar - Converter Sta East	6.69	2	17.5	18.00	13.60	C
Northridge-01	1994	Topanga - Fire Sta	6.69	2	17.5	18.00	14.19	C
Northridge-01	1994	LA 00	6.69	2	17.5	18.00	14.41	C
Northridge-01	1994	Stone Canyon	6.69	2	17.5	18.00	14.41	C
Northridge-01	1994	Santa Susana Ground	6.69	2	17.5	18.00	14.66	C
Northridge-01	1994	LA - Chalon Rd	6.69	2	17.5	18.00	14.92	C
Northridge-01	1994	Beverly Hills - 12520 Mulhol	6.69	2	17.5	18.00	16.27	C
Northridge-01	1994	Sylmar - Olive View Med FF	6.69	2	17.5	18.00	16.77	C
Northridge-01	1994	LA - N Faring Rd	6.69	2	17.5	18.00	16.99	D
Northridge-01	1994	LA - Brentwood VA Hospital	6.69	2	17.5	18.00	17.95	C

Table 4.2 (Continued)

Earthquake Name	Year	Station Name	M_w	Fault Mech.*	Depth (km)	Fault Rup. Length (km)	R_{epi} (km)	Soil Type Based on V_{S30}
Northridge-01	1994	Pacific Palisades - Sunset	6.69	2	17.5	18.00	18.22	C
Northridge-01	1994	LA - UCLA Grounds	6.69	2	17.5	18.00	18.62	C
Northridge-02	1994	Arleta - Nordhoff Fire Sta	6.05	2	6	8.94	6.55	D
San Fernando	1971	Pacoima Dam (upper left abut)	6.61	2	13	16.00	11.86	A
San Salvador	1986	Geotech Investig Center	5.80	0	10.9	8.00	7.93	C
Santa Barbara	1978	Santa Barbara Courthouse	5.92	3	12.7	10.00	3.20	C
Superstition Hills-02	1987	Superstition Mtn Camera	6.54	0	9	20.00	7.50	C
Superstition Hills-02	1987	Poe Road (temp)	6.54	0	9	20.00	11.20	D
Superstition Hills-02	1987	Parachute Test Site	6.54	0	9	20.00	15.99	D
Superstition Hills-02	1987	Kornbloom Road (temp)	6.54	0	9	20.00	19.28	D
Superstition Hills-02	1987	Westmorland Fire Sta	6.54	0	9	20.00	19.51	D
Tabas, Iran	1978	Dayhook	7.35	2	5.75	90.00	20.63	C
Westmorland	1981	Westmorland Fire Sta	5.90	0	2.3	10.00	7.02	D
Westmorland	1981	Salton Sea Wildlife Refuge	5.90	0	2.3	10.00	8.62	D
Whittier Narrows-01	1987	Garvey Res. - Control Bldg	5.99	3	14.6	10.00	2.86	C
Whittier Narrows-01	1987	Whittier Narrows Dam upstream	5.99	3	14.6	10.00	4.16	D
Whittier Narrows-01	1987	San Gabriel - E Grand Ave	5.99	3	14.6	10.00	4.77	C
Whittier Narrows-01	1987	Alhambra - Fremont School	5.99	3	14.6	10.00	6.77	C
Whittier Narrows-01	1987	El Monte - Fairview Av	5.99	3	14.6	10.00	7.50	D
Whittier Narrows-01	1987	San Marino - SW Academy	5.99	3	14.6	10.00	8.59	C
Whittier Narrows-01	1987	LA - Obregon Park	5.99	3	14.6	10.00	9.05	D
Whittier Narrows-01	1987	Arcadia - Campus Dr	5.99	3	14.6	10.00	9.89	C

*Fault mechanism based on rake angle: 0, 1, 2, 3 and 4 denote strike-slip, normal, reverse, reverse-oblique, and normal-oblique, respectively.

4.2. Near-Fault Prediction Model for Elastic and Inelastic Input Energy

The prediction model developed by Akkar and Bommer (2007a and 2007b) given in Equation 4.1, similar to Section 3.3, is employed for predicting input energy spectra for elastic and inelastic systems in terms of energy equivalent velocity V_{eq} considering near-fault effects.

$$\log(V_{eq}) = b_1 + b_2 M + b_3 M^2 + (b_4 + b_5 M) \log \sqrt{R_{jb}^2 + b_6^2} + b_7 S_S + b_8 S_A + b_9 F_N + b_{10} F_R \quad (4.1)$$

In Equation 4.1, M is the moment magnitude and R_{jb} is the Joyner-Boore distance in kilometers. S_S and S_A are dummy variables representing the influence of site class. S_S

is 0 and S_A is 1 for stiff sites, and S_S is 1 and S_A is 0 for soft sites. F_N is zero and F_R is 1 for reverse faulting, and the opposite for normal faulting. They are both 0 for strike slip. The model given in Equation 4.1 has also been modified by simplifying the geometrical decay term, and replacing the Joyner-Boore distance R_{jb} with the distance to epicenter R_{epi} , because R_{jb} data are missing for some earthquake ground motions in the database. Accordingly, the form of geometrical decay is simplified as $(\log(R_{epi}))$, without using any additional term. This is due to the fact that seismic waves reach the station from many parts of long rupture in the near-fault regions unlike in the far-fault case where the source is idealized as a point, and hence geometric decay of the earthquake is small (Ambraseys and Douglas 2003). After implementing these modifications, the prediction model derived for near-fault ground motions becomes as in Equation (4.2).

$$\log(V_{eq}) = b_1 + b_2M + b_3M^2 + (b_4 + b_5M)\log(R_{epi}) + b_6S_S + b_7S_A + b_8F_N + b_9F_R \quad (4.2)$$

The regression coefficients in Equation 4.2 are determined by a one-stage nonlinear regression analysis at the specified period values for observed (computed) spectral values of linear elastic and inelastic systems in the units of cm/s, separately. The basic reason for this choice is the presence of several single recorded events in the database (Table 4.2), generally in the lower earthquake magnitude ranges. Two-stage nonlinear regression analysis technique gives more weight to these less well-recorded earthquakes in the database, which may lead to the violation of magnitude saturation. Accordingly, two-stage analysis overestimates spectral energy at higher magnitudes and underestimates at lower magnitudes (Ambraseys and Douglas 2003, and Akkar and Bommer 2007a). A mass proportional 5% viscous damping ratio is used in the analysis. Elastic, perfectly plastic force-deformation model (bilinear model with zero strain hardening) is employed for inelastic systems which leads to more conservative responses (Bozorgnia et al. 2010). Three different lateral strength ratios ($R_\mu = 2, 4$ and 6) are employed for defining the level of inelasticity. A near-fault ground motion may possess impulsive characteristics, but certainly it is unpredictable at this state of

knowledge. Hence, it is preferred in this thesis study that ground motions in the database are not classified into separate groups, such as with and without directivity pulses. Some ground motions in the database may possess pulses that are effective on the response of particular SDOF systems with periods close to the pulse periods, however the prediction equations derived herein are based on the mean energy response to all ground motions, hence the effect of pulses are smoothed out on the predicted response spectra. It is also worthwhile to note that a pulse-like ground motion may exhibit impulsive characteristics only within a narrow band of orientations, whereas the components considered in the other orientations are evaluated as rather ordinary (Baker 2007, Chopra and Chintanapakdee 2001). Therefore, including the probability of occurrence of more demanding components exhibiting impulsive features in the design stage may produce overestimation of design energy values. This situation is also valid for the fling effect. Therefore, fault directivity and fling effects are not included explicitly in the prediction model in order to reduce complexity, and to maintain the reliability of results. The regression coefficients computed for elastic ($R_\mu = 1$) and inelastic SDOF systems ($R_\mu = 2, 4, 6$) are presented in Table 4.3 to Table 4.6 respectively, for 5% damping ($\xi = 5\%$).

The residuals (*Res.*) between the observed and estimated V_{eq} values are also computed for elastic and inelastic spectral ordinates by using the expression given in Equation 4.3. Examples of residual scatter plots relative to R_{epi} and M_w with respect to the corresponding best fit lines are shown in Figure 4.2 and Figure 4.3 for elastic ($R_\mu = 1$) and inelastic ($R = 4$) SDOF systems respectively, at 1.0 and 4.0 second periods. It is observed from both figures that the slopes of the best-fit lines are almost equal to zero. Hence, the data are uniformly distributed among the predictor variables M_w and R_{epi} , and the values estimated from the prediction equation can be classified as unbiased with respect to the independent variables.

$$Res = \log(V_{eq_{est.}}) - \log(V_{eq_{obs.}}) \quad (4.3)$$

Table 4.3. Regression coefficients calculated for linear elastic systems ($R_\mu=1$) with $\zeta=5\%$

T (s)	b_1	b_2	b_3	b_4	b_5	b_6	b_7	b_8	b_9	σ
0.05	-3.86717	1.72517	-0.11978	-0.13474	-0.00248	-1.43349	-1.43367	-0.18478	0.09495	0.10722
0.10	-3.92452	1.95671	-0.13888	-0.54618	0.05268	-1.46669	-1.45789	-0.17176	0.06250	0.10889
0.20	-2.60946	1.29791	-0.07547	0.42678	-0.09506	-0.80605	-0.80342	-0.13007	0.08046	0.12117
0.30	-3.94815	1.95047	-0.12226	0.08301	-0.05591	-1.46302	-1.48462	-0.14040	0.04965	0.14376
0.40	-5.14809	2.46343	-0.15863	0.04344	-0.04189	-2.05245	-2.09579	-0.10660	0.04765	0.15697
0.50	-4.92087	2.26516	-0.13617	0.64573	-0.13129	-1.93209	-1.98887	-0.11711	0.05207	0.16388
0.60	-3.99738	1.85825	-0.10590	0.56189	-0.11984	-1.45046	-1.54696	-0.11130	0.05559	0.16747
0.70	-3.75086	1.73623	-0.09482	0.66274	-0.13945	-1.33317	-1.41774	-0.12123	0.04788	0.16950
0.80	-4.00761	1.84628	-0.10368	0.57212	-0.12136	-1.45896	-1.54864	-0.12246	0.05933	0.17594
0.90	-3.83114	1.69087	-0.08744	0.83023	-0.15594	-1.36981	-1.46134	-0.07414	0.07421	0.18769
1.00	-3.11892	1.41902	-0.07220	0.30541	-0.07138	-1.00123	-1.11760	-0.05856	0.06536	0.19494
1.20	-4.15781	1.87973	-0.10514	0.13614	-0.04820	-1.50398	-1.65429	-0.06307	-0.00254	0.21203
1.40	-4.83931	2.23811	-0.13796	-0.42494	0.04397	-1.83746	-2.00186	-0.04299	0.01091	0.22302
1.50	-5.61918	2.62097	-0.16867	-0.76955	0.09343	-2.23079	-2.38841	-0.07361	-0.00394	0.23381
1.60	-5.92567	2.76632	-0.18018	-0.95591	0.12196	-2.38720	-2.53839	-0.09053	-0.02445	0.24394
1.80	-5.53734	2.55463	-0.16241	-0.85339	0.10841	-2.18596	-2.35140	-0.07439	-0.04885	0.25033
2.00	-5.81328	2.61340	-0.16269	-0.54914	0.06421	-2.31629	-2.49722	-0.03741	-0.04690	0.25634
2.50	-7.49101	3.28049	-0.20787	-0.24777	0.02193	-3.15890	-3.33195	-0.06036	-0.02557	0.27026
3.00	-6.73212	2.88424	-0.17566	-0.13989	0.01051	-2.78283	-2.94931	-0.06634	-0.08014	0.28324
3.50	-5.75791	2.34432	-0.12927	0.11848	-0.02527	-2.30465	-2.45355	-0.10109	-0.10550	0.30702
4.00	-5.30220	2.12806	-0.11402	-0.05267	0.00513	-2.07496	-2.22734	-0.13192	-0.11181	0.32126
5.00	-4.21074	1.55995	-0.06755	0.09921	-0.01907	-1.53382	-1.67655	-0.16179	-0.11535	0.33568
6.00	-3.94276	1.47364	-0.06565	-0.39496	0.05858	-1.39866	-1.54408	-0.17840	-0.11574	0.34855

Table 4.4. Regression coefficients calculated for yielding systems with $R_\mu=2$ and $\zeta=5\%$

T (s)	b_1	b_2	b_3	b_4	b_5	b_6	b_7	b_8	b_9	σ
0.05	-2.71007	1.19156	-0.06573	0.49358	-0.09869	-0.82338	-0.88667	-0.04257	0.00659	0.10569
0.10	-3.59249	1.81534	-0.12541	-0.40022	0.03592	-1.27644	-1.31604	-0.10108	0.07182	0.10572
0.20	-3.08666	1.52171	-0.09107	0.41565	-0.09478	-1.03999	-1.04668	-0.13149	0.07122	0.12462
0.30	-3.94789	1.94788	-0.12189	0.10648	-0.05521	-1.45939	-1.48828	-0.14233	0.05283	0.14425
0.40	-5.18662	2.48193	-0.15969	0.05841	-0.04358	-2.06537	-2.11780	-0.10134	0.05028	0.15814
0.50	-4.78182	2.21928	-0.13325	0.58984	-0.12359	-1.85543	-1.92742	-0.11316	0.04690	0.16305
0.60	-4.29185	2.00258	-0.11714	0.50166	-0.11050	-1.60032	-1.69167	-0.11144	0.04707	0.16787
0.70	-4.19264	1.94363	-0.11137	0.54928	-0.11838	-1.55366	-1.63906	-0.11744	0.04539	0.17237
0.80	-4.00433	1.85038	-0.10473	0.47413	-0.10300	-1.45593	-1.54848	-0.10152	0.04985	0.17717
0.90	-3.83965	1.74336	-0.09518	0.47681	-0.09938	-1.36758	-1.47209	-0.07401	0.05159	0.18806
1.00	-3.55471	1.63675	-0.08946	0.18361	-0.05268	-1.21224	-1.34241	-0.07195	0.03405	0.19588
1.20	-4.33515	1.95877	-0.11129	0.14998	-0.04781	-1.59058	-1.74500	-0.06497	-0.00011	0.21231
1.40	-4.97859	2.28535	-0.13963	-0.35496	0.03146	-1.90920	-2.07297	-0.06479	-0.00615	0.22822
1.50	-5.35428	2.47705	-0.15597	-0.61764	0.07150	-2.09582	-2.25845	-0.07648	-0.01538	0.23575
1.60	-5.67592	2.62960	-0.16839	-0.75741	0.09419	-2.25901	-2.41678	-0.08377	-0.02635	0.24126
1.80	-5.78907	2.64631	-0.16787	-0.68100	0.08489	-2.31083	-2.47810	-0.07953	-0.04236	0.24974
2.00	-6.04686	2.71917	-0.17064	-0.53322	0.06265	-2.43701	-2.60972	-0.05922	-0.04221	0.25599
2.50	-6.84334	3.01653	-0.19039	-0.41453	0.04980	-2.83902	-3.00392	-0.07167	-0.03779	0.26972
3.00	-6.34046	2.71408	-0.16353	-0.17878	0.01676	-2.58927	-2.75116	-0.07935	-0.06822	0.28217
3.50	-5.61230	2.30973	-0.12896	-0.00600	-0.00697	-2.23100	-2.38130	-0.09975	-0.08690	0.30030
4.00	-5.26014	2.14777	-0.11822	-0.19314	0.02542	-2.05655	-2.20371	-0.12078	-0.09514	0.31150
5.00	-4.32895	1.67320	-0.08018	-0.13396	0.01581	-1.59303	-1.73618	-0.14897	-0.10636	0.32439
6.00	-3.76734	1.43821	-0.06572	-0.48979	0.07116	-1.31239	-1.45499	-0.16177	-0.10643	0.33410

Table 4.5. Regression coefficients calculated for yielding systems with $R_{\mu}=4$ and $\xi=5\%$

T (s)	b_1	b_2	b_3	b_4	b_5	b_6	b_7	b_8	b_9	σ
0.05	-1.01196	0.39769	0.00376	1.15553	-0.20825	0.01630	-0.02748	-0.02664	-0.01220	0.11599
0.10	-3.60539	1.79488	-0.11626	-0.25049	0.01155	-1.27087	-1.33445	-0.10088	0.06408	0.13614
0.20	-3.67345	1.80613	-0.11214	0.13941	-0.05128	-1.31685	-1.35661	-0.12144	0.06429	0.13960
0.30	-4.29028	2.08903	-0.13159	0.01503	-0.03572	-1.61637	-1.67387	-0.12100	0.05176	0.15460
0.40	-4.78879	2.28293	-0.14343	0.10095	-0.04602	-1.85997	-1.92854	-0.11086	0.03978	0.16421
0.50	-4.56178	2.13786	-0.12891	0.33167	-0.08139	-1.73709	-1.82497	-0.11506	0.03862	0.17073
0.60	-4.48319	2.09222	-0.12476	0.30833	-0.07811	-1.69247	-1.79058	-0.09893	0.04129	0.17605
0.70	-4.21701	1.95612	-0.11359	0.33350	-0.08058	-1.55805	-1.65884	-0.09300	0.03362	0.17982
0.80	-4.16717	1.91668	-0.11001	0.31909	-0.07618	-1.52937	-1.63779	-0.08659	0.03631	0.18652
0.90	-4.03595	1.83552	-0.10296	0.28688	-0.06853	-1.45596	-1.58031	-0.07097	0.02981	0.19646
1.00	-3.94671	1.79129	-0.09989	0.17440	-0.04990	-1.40156	-1.54494	-0.07166	0.02019	0.20503
1.20	-4.58145	2.06597	-0.12008	0.00650	-0.02343	-1.71412	-1.86997	-0.06814	-0.00193	0.22071
1.40	-4.85899	2.20480	-0.13253	-0.29828	0.02515	-1.84911	-2.01084	-0.07223	-0.01372	0.23297
1.50	-5.18340	2.35392	-0.14434	-0.41170	0.04333	-2.01152	-2.17188	-0.07732	-0.01926	0.23848
1.60	-5.45332	2.48353	-0.15500	-0.53444	0.06260	-2.14784	-2.30552	-0.08284	-0.02816	0.24228
1.80	-5.70462	2.57907	-0.16157	-0.57524	0.07023	-2.27095	-2.43368	-0.08005	-0.03857	0.25099
2.00	-5.90251	2.64680	-0.16583	-0.57895	0.07197	-2.36822	-2.53442	-0.06675	-0.03808	0.25772
2.50	-6.25446	2.74552	-0.17055	-0.46241	0.05778	-2.54733	-2.70743	-0.07951	-0.04143	0.27058
3.00	-5.72208	2.43163	-0.14297	-0.23542	0.02556	-2.28294	-2.43938	-0.08358	-0.06057	0.28218
3.50	-5.23207	2.18122	-0.12343	-0.28322	0.03497	-2.04034	-2.19159	-0.09844	-0.07242	0.29400
4.00	-4.91007	2.01745	-0.11108	-0.34613	0.04678	-1.88054	-2.02878	-0.11442	-0.07906	0.30302
5.00	-4.28994	1.68571	-0.08382	-0.26521	0.03386	-1.57181	-1.71811	-0.13390	-0.08780	0.31323
6.00	-3.86651	1.50644	-0.07294	-0.52630	0.07480	-1.36157	-1.50495	-0.14375	-0.08935	0.31899

Table 4.6. Regression coefficients calculated for yielding systems with $R_{\mu}=6$ and $\xi=5\%$

T (s)	b_1	b_2	b_3	b_4	b_5	b_6	b_7	b_8	b_9	σ
0.05	0.21252	-0.20362	0.05404	1.50407	-0.26033	0.62405	0.58840	-0.00261	-0.05554	0.12478
0.10	-3.81960	1.87911	-0.11964	-0.23029	0.00796	-1.37591	-1.44368	-0.10002	0.05321	0.15037
0.20	-3.81907	1.87461	-0.11692	-0.04248	-0.02208	-1.38083	-1.43858	-0.11673	0.05319	0.15222
0.30	-4.20816	2.03882	-0.12718	-0.01944	-0.02649	-1.56809	-1.64000	-0.11436	0.04333	0.16118
0.40	-4.66496	2.21680	-0.13807	0.03908	-0.03438	-1.79120	-1.87305	-0.10954	0.03414	0.17188
0.50	-4.50917	2.12091	-0.12879	0.14282	-0.05047	-1.70578	-1.80225	-0.11073	0.03334	0.17764
0.60	-4.52823	2.11266	-0.12706	0.16058	-0.05276	-1.71039	-1.81746	-0.09028	0.03294	0.18260
0.70	-4.23403	1.95472	-0.11347	0.23830	-0.06439	-1.56143	-1.67199	-0.08815	0.02638	0.18741
0.80	-4.18011	1.92102	-0.11087	0.18795	-0.05483	-1.53027	-1.64998	-0.08421	0.02884	0.19346
0.90	-4.11687	1.86622	-0.10544	0.20410	-0.05481	-1.49280	-1.62391	-0.07454	0.02153	0.20233
1.00	-4.04890	1.82660	-0.10248	0.13227	-0.04203	-1.45204	-1.59708	-0.07118	0.01644	0.20975
1.20	-4.58313	2.05801	-0.11972	-0.04447	-0.01398	-1.71381	-1.86823	-0.07113	-0.00560	0.22449
1.40	-4.84480	2.18473	-0.13075	-0.29596	0.02572	-1.84319	-2.00240	-0.07562	-0.01526	0.23537
1.50	-4.84480	2.18473	-0.13075	-0.29596	0.02572	-1.84319	-2.00240	-0.07562	-0.01526	0.23537
1.60	-5.23645	2.36681	-0.14559	-0.49685	0.05750	-2.04054	-2.19619	-0.08284	-0.02818	0.24404
1.80	-5.44485	2.44716	-0.15134	-0.56253	0.06880	-2.14227	-2.30238	-0.07801	-0.03774	0.25232
2.00	-5.64652	2.51474	-0.15542	-0.53748	0.06614	-2.24166	-2.40487	-0.06956	-0.03803	0.25812
2.50	-5.89003	2.56248	-0.15609	-0.39725	0.04778	-2.36641	-2.52356	-0.08179	-0.04186	0.27004
3.00	-5.43216	2.29908	-0.13358	-0.26579	0.02998	-2.13900	-2.29309	-0.08725	-0.05646	0.28065
3.50	-5.00929	2.08050	-0.11648	-0.29451	0.03616	-1.92875	-2.08026	-0.10051	-0.06499	0.29038
4.00	-4.68283	1.91524	-0.10394	-0.35210	0.04674	-1.76704	-1.91603	-0.11417	-0.07184	0.29886
5.00	-4.21370	1.66016	-0.08310	-0.29732	0.03789	-1.53362	-1.67957	-0.13024	-0.07834	0.30640
6.00	-3.85858	1.50813	-0.07394	-0.51276	0.07186	-1.35770	-1.50087	-0.13822	-0.07936	0.31055

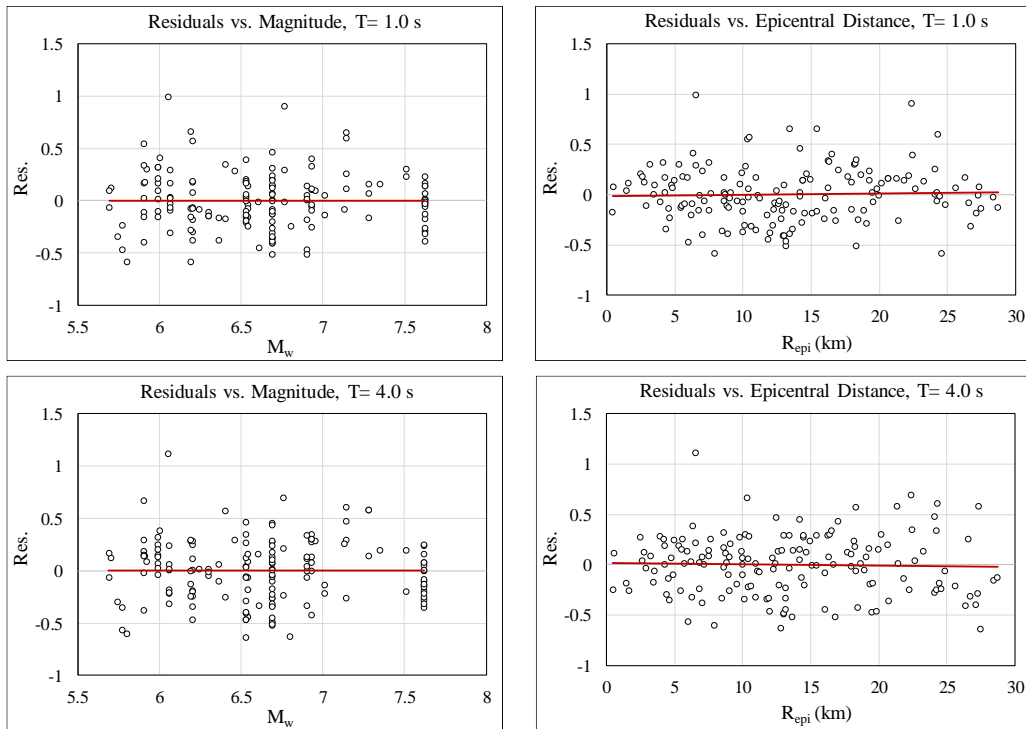


Figure 4.2. Residual of observed and estimated V_{eq} values for elastic systems ($R_{\mu} = 1$)

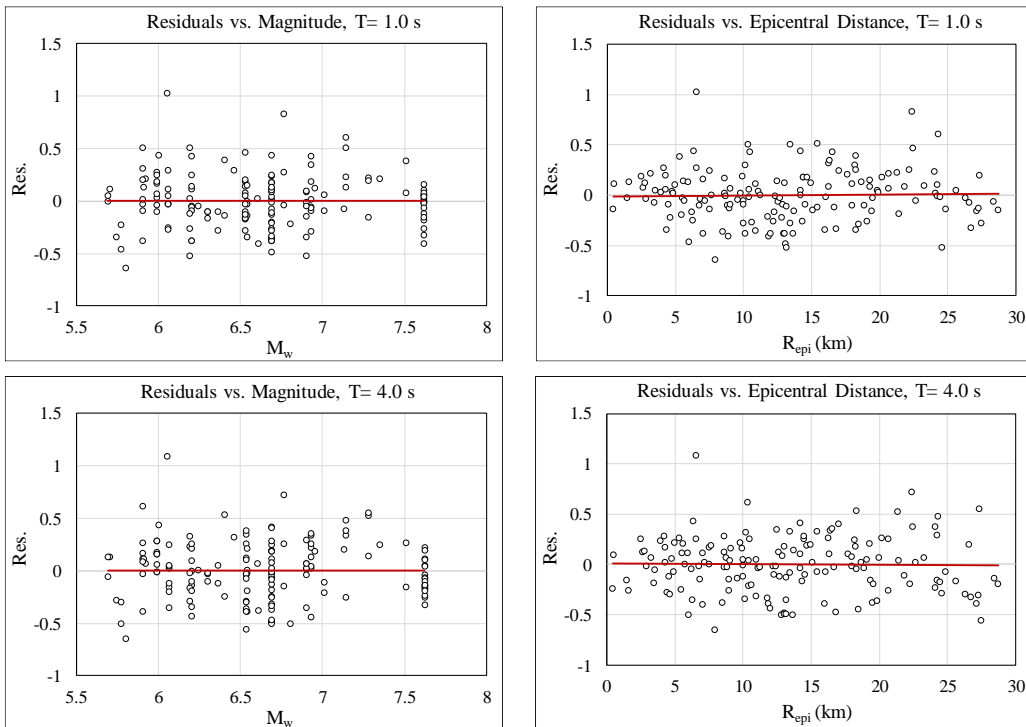


Figure 4.3. Residuals of observed and estimated V_{eq} values for inelastic systems ($R_{\mu} = 4$)

4.3. Near-Fault Elastic Input Energy Prediction

Near-field ground motions may exhibit particular characteristics that affect seismic demand on structures. In order to observe these differences, the variations of 5% damped elastic V_{eq} spectra with distance R_{epi} are obtained from the NF prediction model derived in this chapter (Equation 4.2 and Table 4.3). They are plotted for three earthquakes and two soil types for the mean and mean \pm one sigma at four specified periods of 0.5, 1.0, 2.0 and 4.0 seconds in Figure 4.4 to Figure 4.7. The computed (observed) V_{eq} spectral ordinates of the ground motions from the selected earthquakes at these periods are also plotted on the corresponding graphics in scatter form. Chi-Chi (1999), Northridge-01 (1994) and Imperial Valley-06 (1979) earthquakes with respective moment magnitudes of 7.62, 6.69, and 6.53 are selected for comparative evaluation. Fault rupture mechanisms of these earthquakes are reverse-oblique, reverse, and strike-slip, respectively.

At longer periods, sensitivity of V_{eq} to distance completely vanishes for the model. This is consistent with the NF condition where seismic waves reach the design site from many parts of long rupture synchronously, hence the distance effect is lost. Computed values from the ground motions of selected earthquakes (circular dots) also display a gradual variation with distance in these figures, and get closer to each other at longer periods especially for GM's recorded on stiff soil given in Figure 4.4 and Figure 4.5.

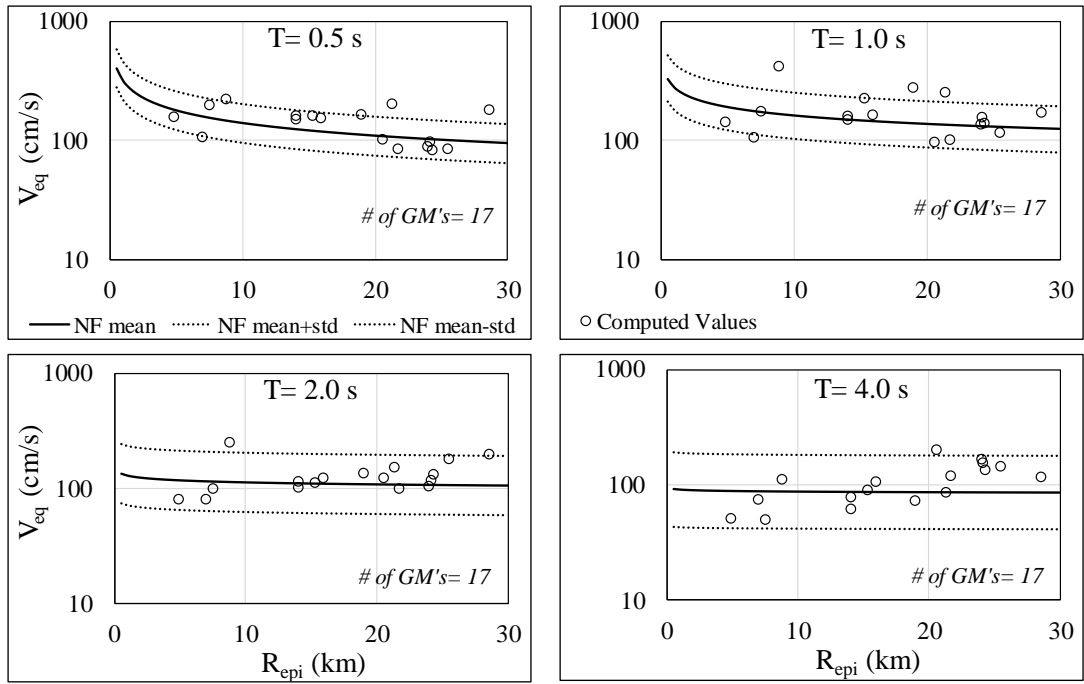


Figure 4.4. Comparison of the computed V_{eq} with the mean and mean \pm one sigma of NF prediction model for $M_w=7.62$ Chi-Chi (1999) earthquake, stiff soil type

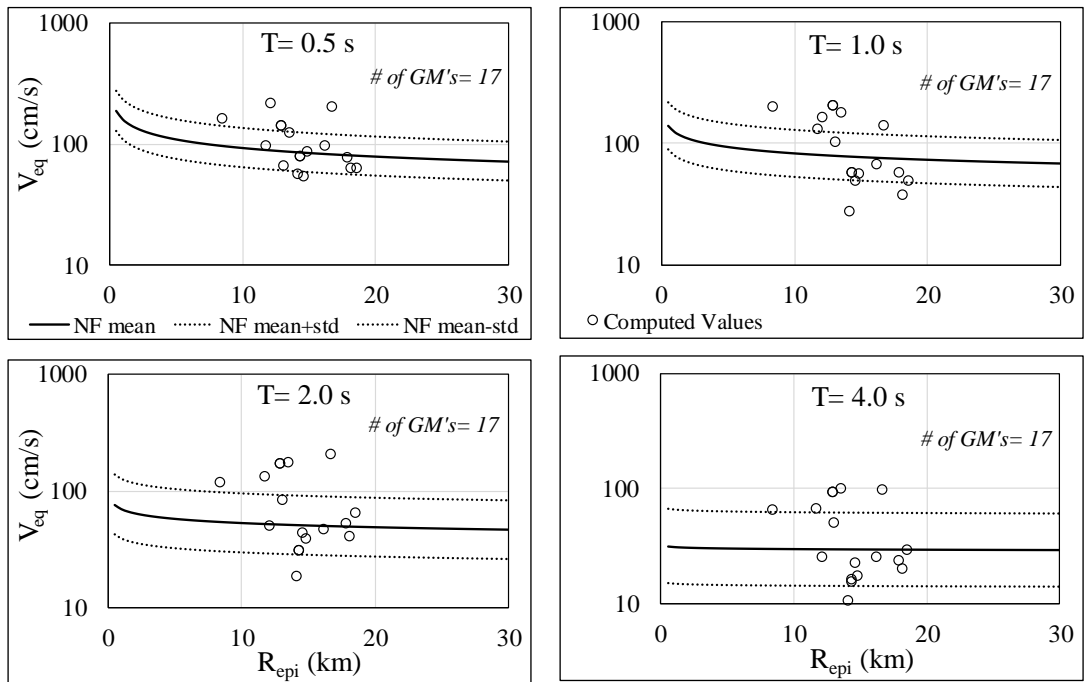


Figure 4.5. Comparison of the computed V_{eq} with the mean and mean \pm 1sigma of NF prediction model for $M_w=6.69$ Northridge-01 (1994) earthquake, stiff soil type

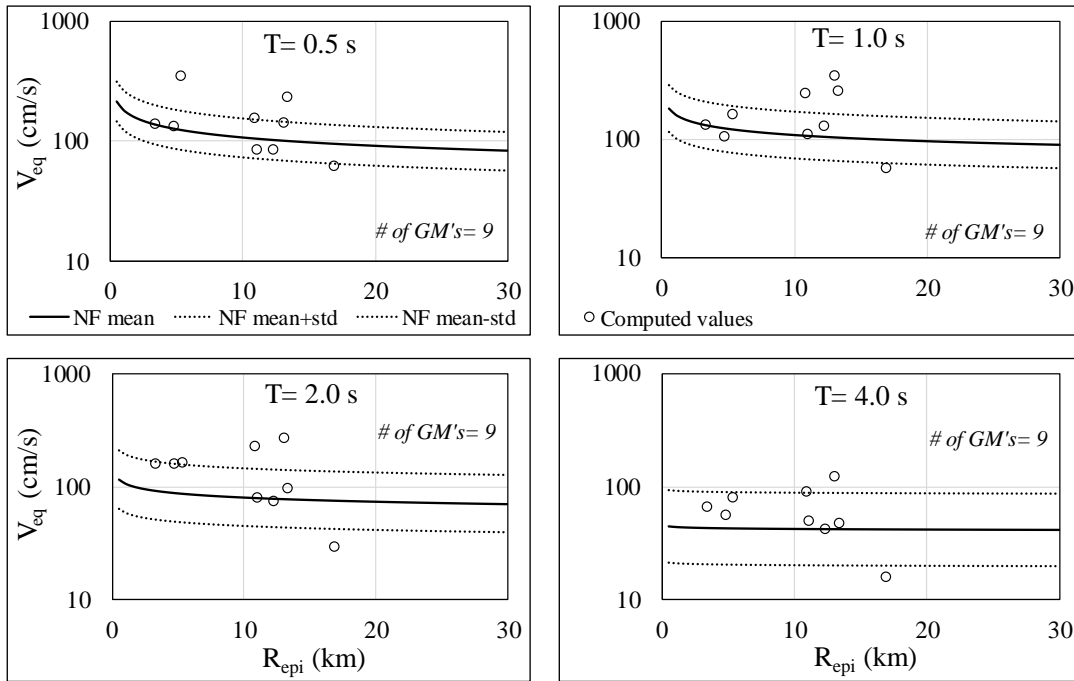


Figure 4.6. Comparison of the computed V_{eq} with the mean and mean ± 1 sigma of NF prediction model for $M_w=6.69$ Northridge-01 (1994) earthquake, soft soil type

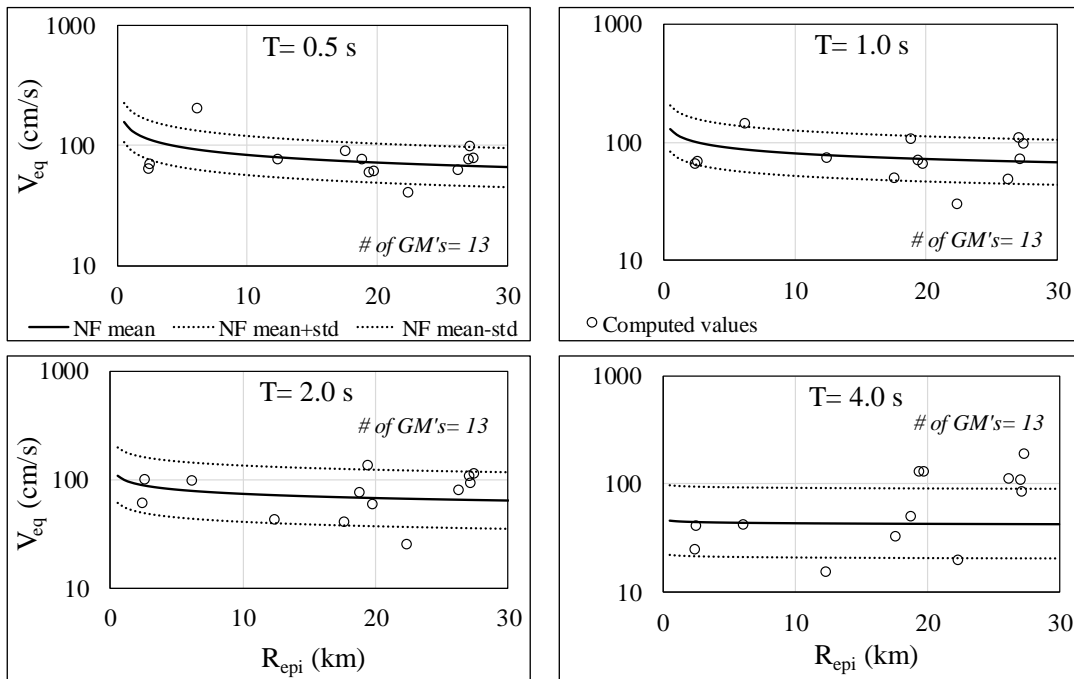


Figure 4.7. Comparison of the computed V_{eq} with the mean and mean ± 1 sigma of NF prediction model for $M_w=6.53$ Imperial Valley-06 (1979) earthquake, soft soil type

Mean elastic input V_{eq} spectra of ground motions selected from Northridge-01 (1994) and Imperial Valley (1979) earthquakes are predicted by the NF prediction equations developed both in this chapter and in Ambraseys and Douglas (2003). The range of epicentral distances for the selected records are 12-16 km for the Northridge-01 (1994) and 17-23 km for the Imperial Valley (1979) earthquakes. The computed elastic input V_{eq} spectra of the selected ground motions from the two earthquakes are shown in Figure 4.8 for two different soil types, along with their mean spectra and the estimated mean spectra from the two prediction models. Epicentral distance is employed in this study whereas it is Joyner-Boore distance in Ambraseys and Douglas. The middle values of the considered distance bands are used in the predictions. It can be observed from Figure 8 that the results of both studies are in fairly good agreement with each other, and match well with the data obtained from the mean of 7 and 5 ground motions for stiff and soft soils, respectively. The differences between the results of two models are perhaps due to different assumptions in these studies. Ambraseys and Douglas (2003) employ the maximum component whereas the geometric mean of two horizontal components are employed in this thesis study. This is the main reason for larger energy predictions by Ambraseys and Douglas in the period range of 0.2-2.0 seconds that they have considered. However, the choices on the distance parameter (epicentral vs. Joyner and Boore) are not expected to play a role on the differences of results because both definitions are consistently accounted for in the associated models.

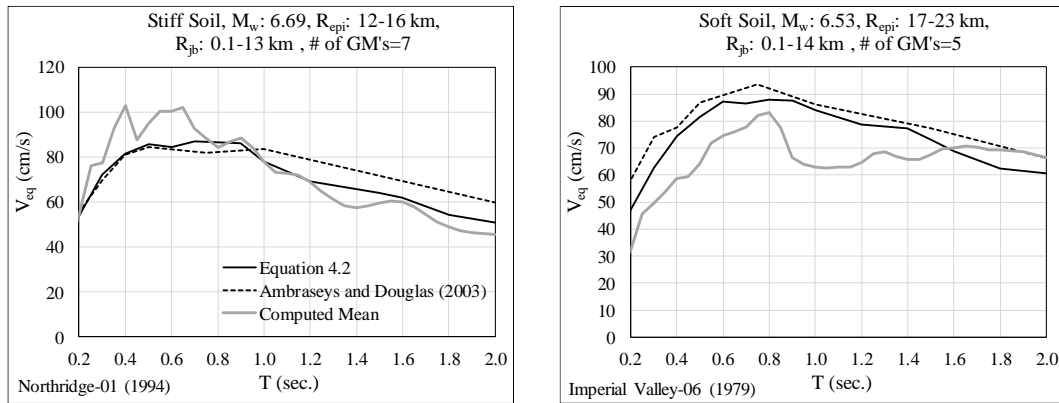


Figure 4.8. The comparison of the computed mean elastic V_{eq} spectra of ground motions selected from $M_w=6.69$ Northridge-01 (1994) and $M_w=6.53$ Imperial Valley (1979) earthquakes with the estimated mean spectra from the two prediction equations.

The sensitivity of mean input V_{eq} spectra to magnitude, distance, fault type and soil type is also evaluated for two magnitudes, three fault distances and three fault types. The mean elastic input energy spectra obtained from the NF model for these parameters are presented in Figure 4.9 to Figure 4.11 comparatively. It can be inferred from the figures that reverse and strike-slip faults impose 15 - 40% higher energy demands compared to the normal faults especially at the medium period region. Moreover, spectral values from strike-slip faults fall slower with period compared to the reverse and normal faults. The effect of soil type is more prominent at large magnitudes where ground motions on soft soils impose considerably higher energy demands than those on stiff soils. The soft-to-stiff V_{eq} ratio is about 1.40 for $M_w 7.0$ and 1.25 for $M_w 6.0$ on average along the period axis. Besides, the effect of epicentral distance on V_{eq} completely disappears at longer periods, that is, $T > 4$ seconds.

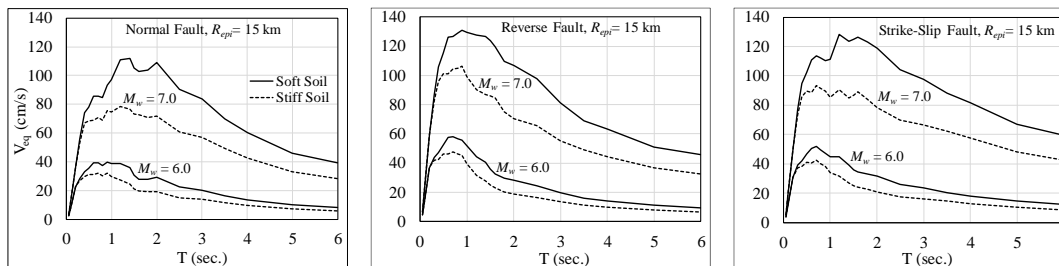


Figure 4.9. Variation of elastic input energy spectra V_{eq} with earthquake magnitude, obtained from NF prediction model for different soil types and fault mechanisms, $R_{epi} = 15 \text{ km}$

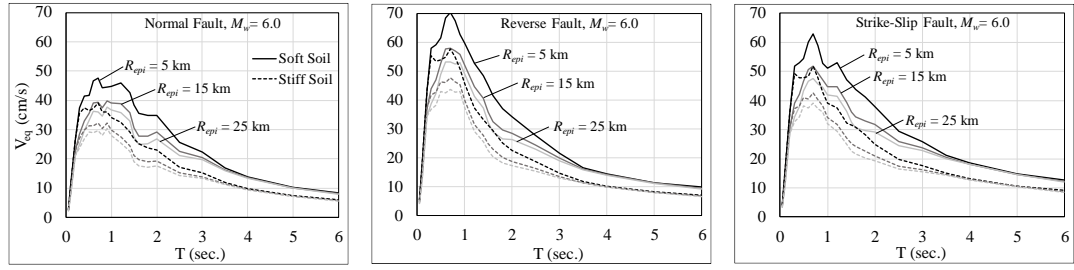


Figure 4.10. Variation of elastic input energy spectra V_{eq} with epicentral distance, obtained from NF prediction model for different soil types and fault mechanisms, $M_w=6.0$

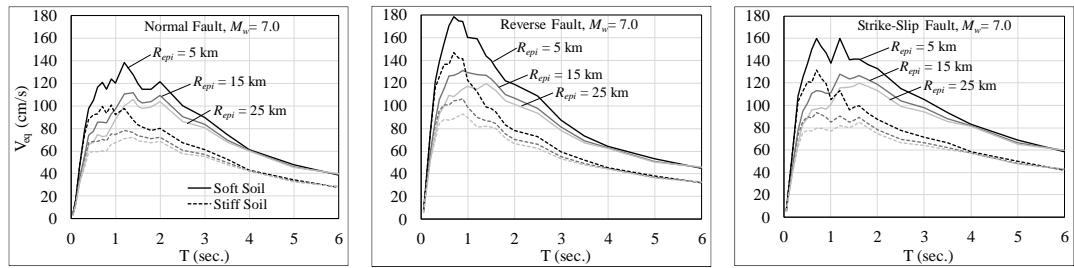


Figure 4.11. Variation of elastic input energy spectra V_{eq} with epicentral distance, obtained from NF prediction model for different soil types and fault mechanisms, $M_w=7.0$

4.4. The Effect of Damping on Near-Fault Elastic and Inelastic Input Energy Spectra

The effect of damping on elastic and inelastic input energy (E_i) spectra of NF ground motions is evaluated by computing the E_i spectra for three GM records from the compiled database presented in Table 4.2: GM111 from Cape Mendocino (1992) Earthquake (M_w 7.01, reverse faulting) recorded at Cape Mendocino Station (stiff soil type, $R_{epi} = 10.36$ km), GM310 from Loma Prieta (1989) Earthquake (M_w 6.93, reverse-oblique faulting) recorded at San Jose-Santa Teresa Hills Station (stiff soil type, $R_{epi} = 20.13$ km), and GM33 from Kocaeli, Turkey (1999) Earthquake (M_w 7.51, strike-slip faulting) recorded at İzmit station (stiff soil type, $R_{epi}=5.31$ km). Geometric mean of the two horizontal components are used in calculating the input energy spectra. Elastic ($R_\mu=1$) and inelastic ($R_\mu=4$) input energy spectra of these ground

motions are compared in Figure 4.12 and Figure 4.13 respectively for three different damping ratios of 2%, 5% and 10%.

It is observed from Figure 4.12 that damping ratio has a slight effect on near fault elastic E_{ie} spectra along the entire period range where higher damping leads to smoother spectral curves. This is also consistent with Nurtuğ and Sucuoğlu (1995). Furthermore, damping ratio has almost no influence on the near fault inelastic input energy spectra E_{iy} due to the reduced effect of damping on inelastic behavior, as inferred from Figure 4.13. The effect of damping on the mean spectra will perhaps be completely diminished, although this is not exercised herein but obvious. Therefore, it can be suggested that $F_{\zeta e} = 1$ and $F_{\zeta y} = 1$ in Figure 2.1 for all damping ratios and all periods. There is no need for scaling the near fault elastic and inelastic input energy spectra for damping. Accordingly, the regression coefficients given in Table 4.3 to Table 4.6 for 5% damping can be employed to predict the near fault input energy spectra of elastic and inelastic systems respectively, for all damping ratios.

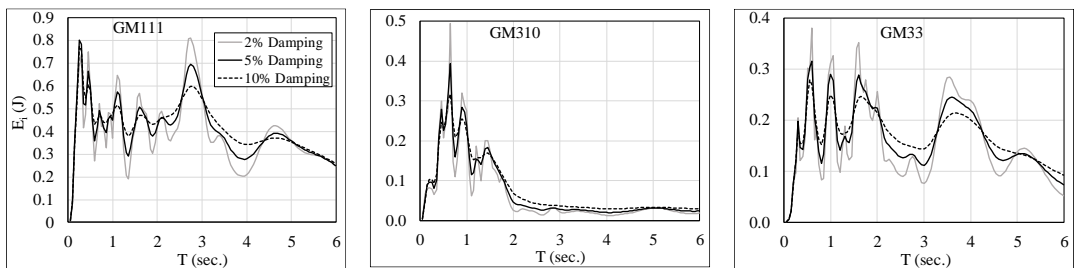


Figure 4.12. Comparison of elastic input energy spectra ($R_{\mu}=1$) of three near fault ground motions for 2, 5 and 10 percent damping ratios

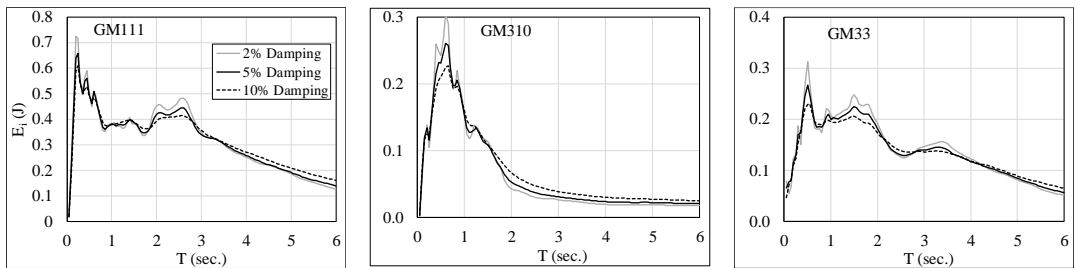


Figure 4.13. Comparison of inelastic input energy spectra ($R_{\mu}=4$) of three near fault ground motions for 2, 5 and 10 percent damping ratios.

4.5. The Effect of Lateral Strength Ratio on Near-Fault Inelastic Input Energy Spectra

Lateral strength ratio R_μ has been identified as one of the most important parameters for characterizing nonlinear behavior of structural systems. Thus, its influence on input energy spectra for yielding systems is further examined in this study. Five percent damped reference elastic ($R_\mu=1$) and inelastic ($R_\mu=2, 4, 6$) input energy spectra are computed for the three near fault GM records selected in the previous section, i.e. GM111, GM310 and GM33. Elastic and inelastic input energy spectra of these records for 5% damping are shown in Figure 4.14. It can be observed that although the variations of E_i with R_μ are somewhat different among the three NF GM's, there are common trends. First, it is clear that E_i for $R_\mu=1$ and $R_\mu=2$ are very close in the average sense where $R_\mu=2$ smoothens the elastic spectra for $R_\mu=1$, but follows almost the same trend along the entire period axis. Second, E_i for $R_\mu=4$ and $R_\mu=6$ fall below E_i for $R_\mu=1$ and $R_\mu=2$ consistently at the long period region ($T > 1$ second) for the considered GM's. However, the differences between $R_\mu=4$ and $R_\mu=6$ are small, and not very sensitive to T .

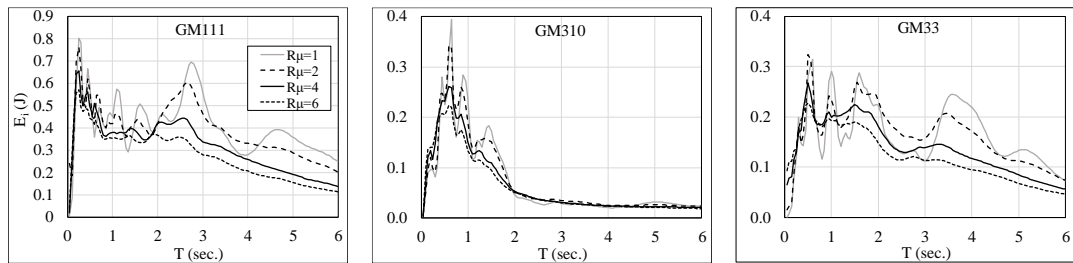


Figure 4.14. Comparison of input energy spectra of three near fault ground motions for four different R_μ values

In order to illustrate the relation between inelastic and elastic input energy spectra, the spectral ratios of inelastic energy spectral ordinates E_i for $R_\mu=2, 4$ and 6 to the elastic spectral ordinates E_i ($R_\mu=1$) are computed for 5% damping and plotted in Figure 4.15. It can be observed from this figure that the inelastic spectra for $R_\mu=2$ fluctuates almost

around 1 however those corresponding to $R_{\mu}=4$ and $R_{\mu}=6$ start falling below 1 after $T > 1$ second. Hence, it is difficult to suggest a simple form for the elastic-to-inelastic scaling functions F_R and F'_R introduced in Figure 2.1, which is reminiscent of an equal energy principle. A healthier conclusion may perhaps be reached on the mean quantities rather than those obtained from individual NF GM's.

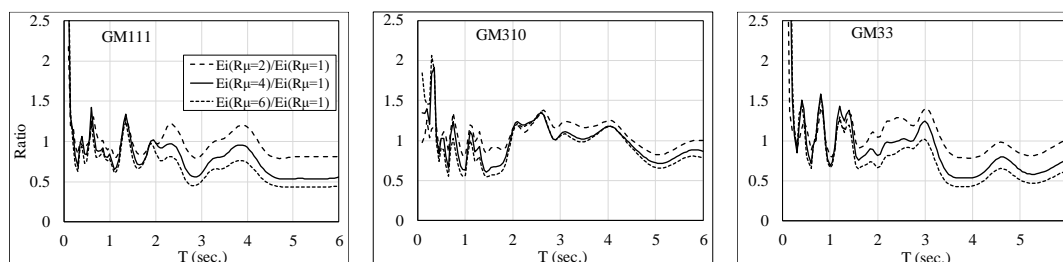


Figure 4.15. Comparison of the ratios of inelastic energy spectral ordinates ($R_{\mu}= 2, 4$ and 6) to the elastic energy spectral ordinates ($R_{\mu}=1$) for the three near fault ground motions

At this stage, the predicted mean values of inelastic input energy spectra will be focused in order to evaluate the estimation accuracy of the derived prediction equation for inelastic input energy demands, and base the decisions attained on the sensitivity of mean inelastic E_i to R_{μ} .

The observed values of 5% damped V_{eq} for $R_{\mu}=4$ for the ground motions from Chi-Chi (1999) and Imperial Valley-06 (1979) earthquakes are plotted on the mean ± 1 sigma variations of V_{eq} with R_{epi} , predicted from Equation 4.2 and Table 4.5 for the source parameters of these earthquakes in Figure 4.16 and Figure 4.17, respectively. Both figures reveal the success of the prediction model in catching the trends of the observed inelastic V_{eq} ordinates. Almost all of the observed (calculated) values fall within the mean ± 1 sigma range.

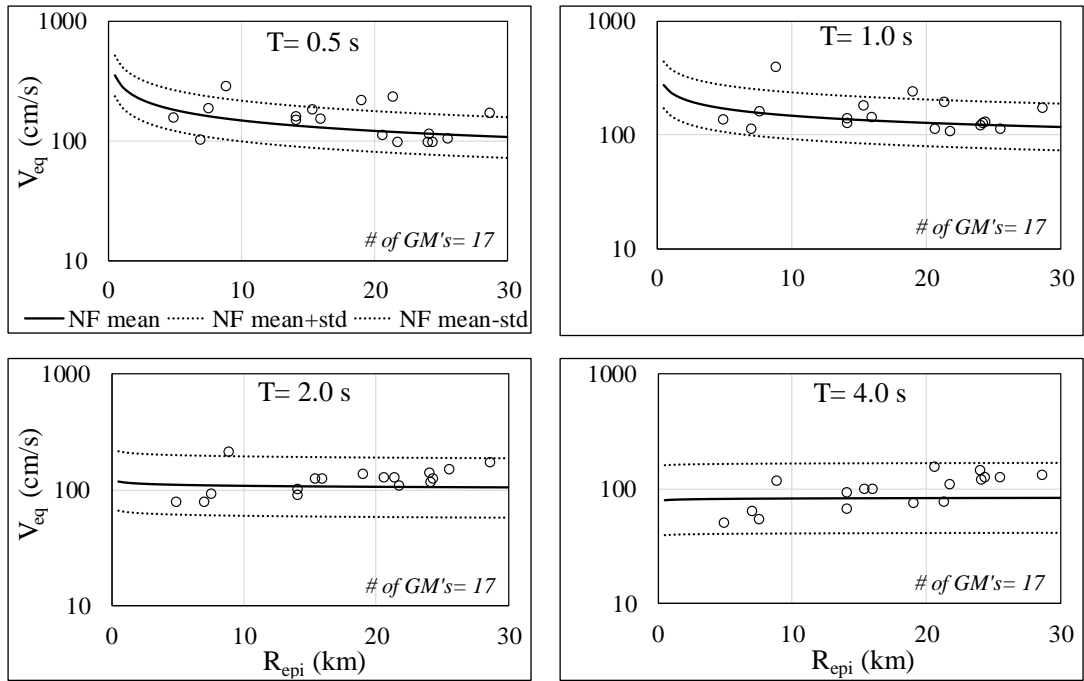


Figure 4.16. Comparison of the computed inelastic V_{eq} with the mean and mean ± 1 sigma of NF prediction model for $M_w=7.62$ Chi-Chi (1999) earthquake, $R_\mu=4$, stiff soil type.

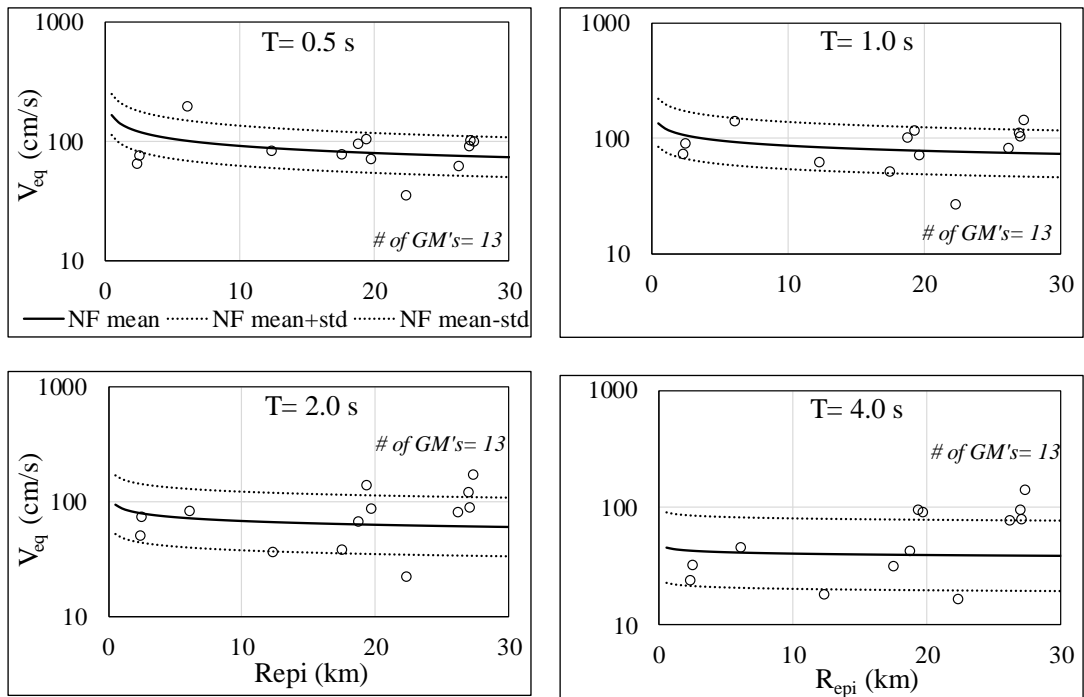


Figure 4.17. Comparison of the computed inelastic V_{eq} with the mean and mean ± 1 sigma of NF prediction model for $M_w=6.53$ Imperial Valley (1979) earthquake, $R_\mu=4$, soft soil type

Inelastic V_{eq} spectra of ground motions selected from the Chi-Chi (1999), Northridge-01 (1994) and Imperial Valley (1979) earthquakes recorded at fairly similar distances, and their mean spectra are calculated for $R_{\mu}=4$ and plotted in Figure 4.18 along with the mean spectra estimated from Equation 4.2, and Table 4.3 and Table 4.5 for $R_{\mu}=1$ and $R_{\mu}=4$, respectively. The ranges of distances for the selected GM records are 19-25 km for the Chi-Chi (1999), 11-17 km for the Northridge-01 (1994) and 17-23 km for the Imperial Valley (1979) earthquakes. Their central values are employed in Equation 4.2 as R_{epi} . The estimated inelastic mean spectra from the proposed prediction model with the regression coefficients for $R_{\mu}=4$ predicts the computed mean spectra with good accuracy. It can also be observed that the estimated mean spectra for $R_{\mu}=4$ and $R_{\mu}=1$ from the developed model display similar spectral variations despite slight differences in short periods.

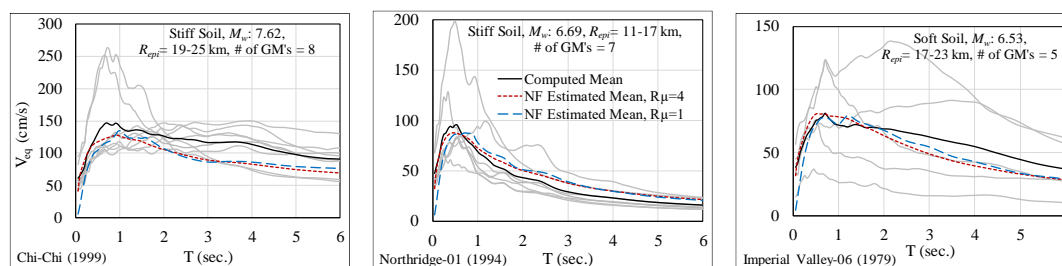


Figure 4.18. Inelastic V_{eq} spectra ($R_{\mu}=4$) of ground motions selected from Chi-Chi (1999), Northridge-01 (1994), Imperial Valley (1979) earthquakes, and the comparison of their mean spectra with the estimated mean spectra from the developed prediction model for $R_{\mu}=4$ and $R_{\mu}=1$

An additional comparison of predicted near fault input energy spectra for four different R_{μ} values ($R_{\mu}=1, 2, 4, 6$) is presented in Figure 4.19. Reverse faulting and stiff soil condition are considered for two earthquake magnitudes of 6.0 and 7.0, and two epicentral distances of 10 km and 20 km. It can be clearly observed from Figure 4.19 that at intermediate and long periods ($T > 0.5$ s), reducing the lateral strength of the system by increasing R_{μ} reduces the near fault input energy demand only slightly, regardless of the earthquake magnitude and distance to epicenter. However, for short period systems with $T < 0.5$ seconds, reduced lateral strength increases input energy demand. Lateral load reduction factor R_{μ} reverses its effect on input energy at

approximately $T=0.5$ s for the cases studied in Figure 4.19. The ratios of predicted inelastic to elastic spectral energy ordinates are given in Figure 4.20. It is clear that at intermediate and long periods ($T > 0.5$ s), the strength factor R_μ has no effect on input energy. However, input energy demand of inelastic systems increase rapidly with R_μ for short period systems ($T < 0.5$ s).

The effects of earthquake magnitude and distance on the input energy spectra estimated from the NF prediction model derived in this section (Equation 4.2) can be observed from Figure 4.19. Magnitude is more prominent on input energy spectral ordinates for elastic and inelastic (yielding) systems when compared to the distance parameter. Increasing magnitude from 6.0 to 7.0 increases spectral ordinates almost 2.5 times whereas increasing distance from 10 to 20 km reduces spectral ordinates by only 15% on average.

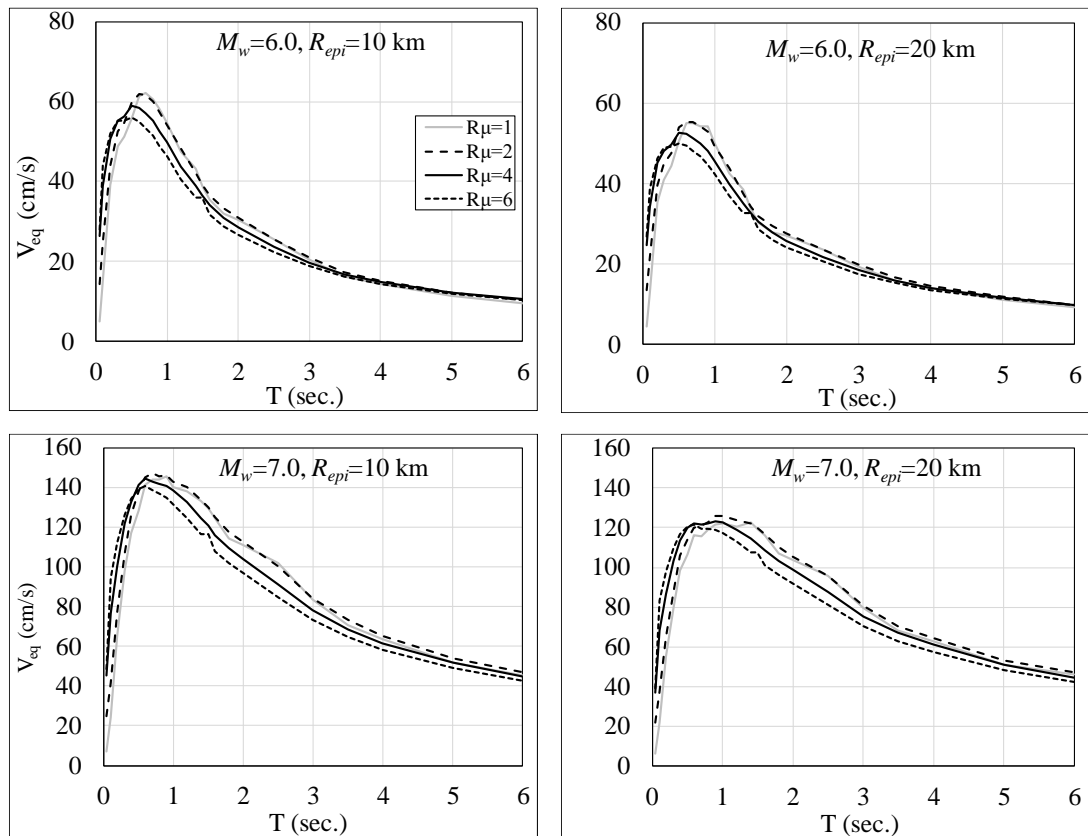


Figure 4.19. Predicted input energy spectra from the prediction model (Equation 4.2) for reverse faulting and stiff soil condition cases considering $M_w= 6.0$ and 7.0 and $R_{epi} = 10$ km and 20 km

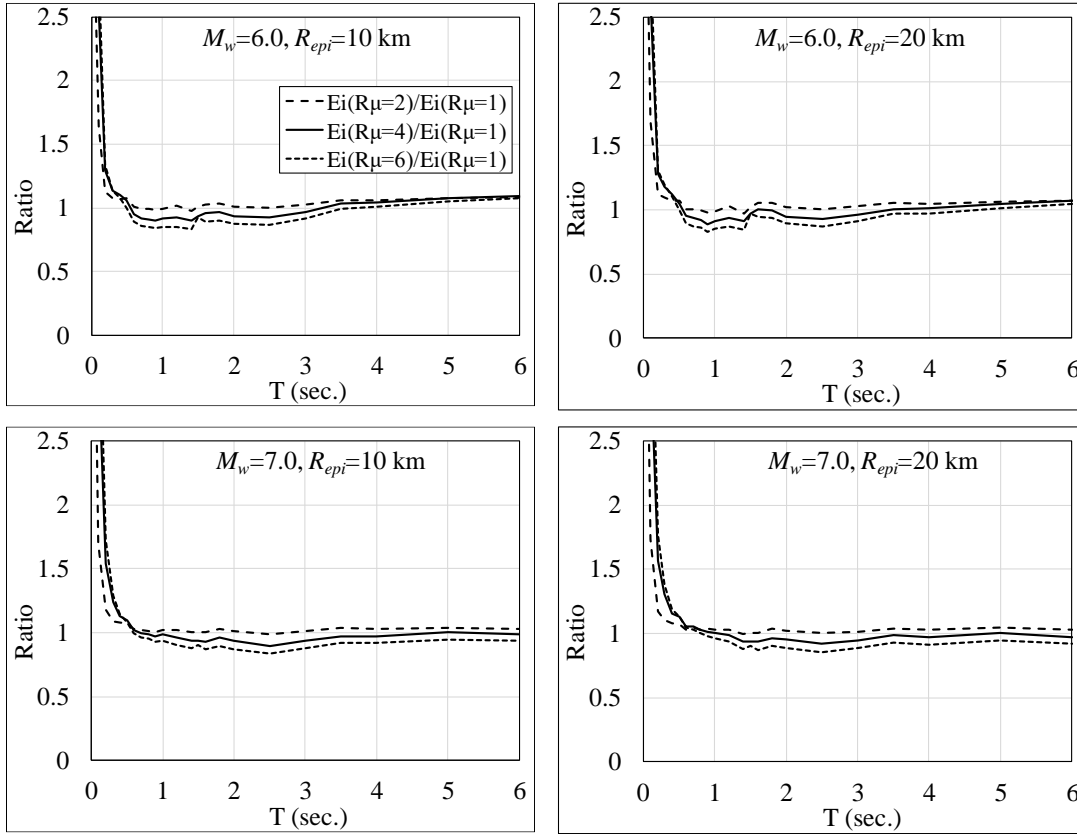


Figure 4.20. Ratios of inelastic energy spectral ordinates ($R_{\mu}=2, 4$ and 6) to the elastic energy spectral ordinates ($R=1$) predicted from the prediction model (Equation 4.2) for reverse faulting and stiff soil conditions considering $M_w= 6.0$ and 7.0 and $R_{epi}= 10$ km and 20 km

Sensitivity of the estimated mean inelastic V_{eq} spectra to magnitude, distance, fault type and soil type is further studied for two magnitudes, three fault distances, three fault types and two soil types. The spectral relations obtained from Equation 4.2 and Table 4.5 for $R_{\mu}=4$ are shown in Figure 4.21 to Figure 4.23 comparatively. It can be inferred from these figures that, similar to elastic input energy given in Section 4.3, reverse and strike-slip faults impose 20-30% higher energy demands compared to the normal faults, and energy demands of strike-slip faults exhibit a slower fall with periods. The effect of soil type is more prominent at large magnitudes, and input energy of ground motions on soft soils are considerably higher than those on stiff soils. The soft-to-stiff V_{eq} ratios calculated from the presented results are on average 1.26 for $M_w 7.0$ and 1.20 for $M_w 6.0$. These ratios are lower when compared to the elastic

case, which were 1.40 and 1.25, respectively. Inelastic input energy spectra are sensitive to distance for epicentral distances closer than 15 km, but distance sensitivity disappears after 15 km for the near fault ground motions.

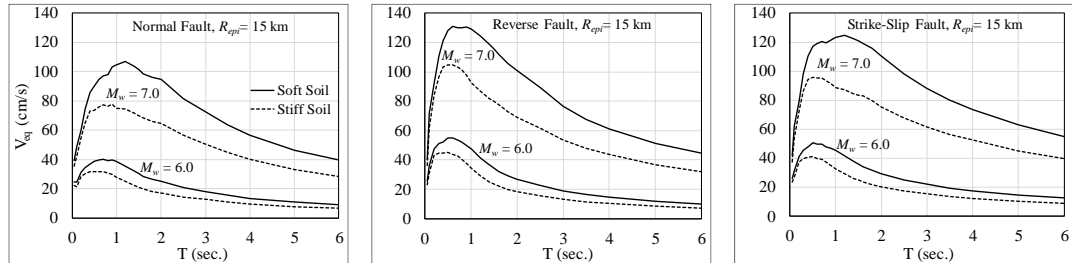


Figure 4.21. Variation of inelastic input energy spectra V_{eq} ($R_{\mu}=4$) with earthquake magnitude obtained from NF prediction model for different soil types and fault mechanisms, $R_{epi}=15$ km

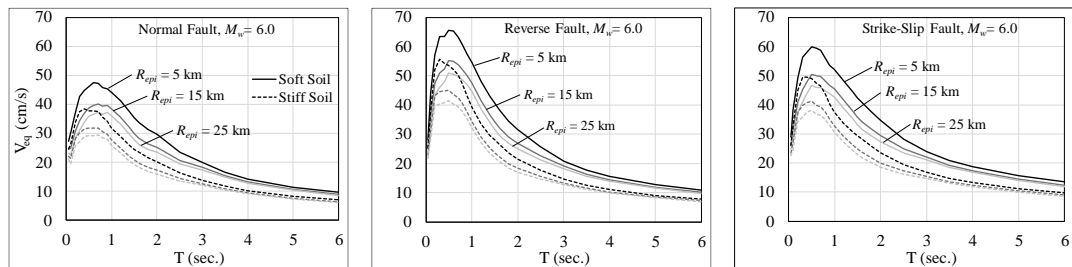


Figure 4.22. Variation of inelastic input energy spectra V_{eq} ($R_{\mu}=4$) with epicentral distance obtained from NF prediction model for different soil types and fault mechanisms, $M_w=6.0$

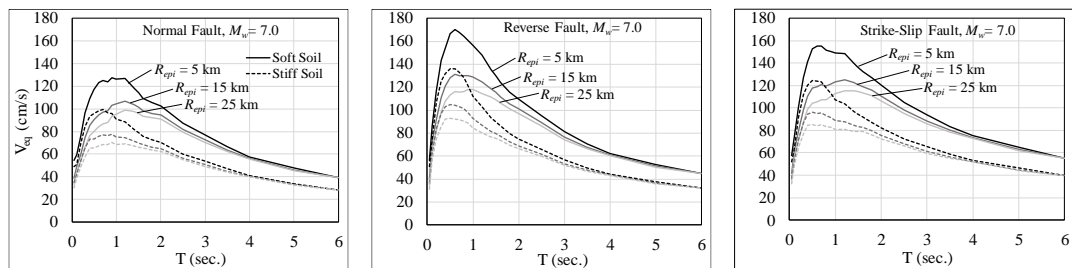


Figure 4.23. Variation of inelastic input energy spectra V_{eq} ($R_{\mu}=4$) with epicentral distance obtained from NF prediction model for different soil types and fault mechanisms, $M_w=7.0$

CHAPTER 5

EQUIVALENT DAMPING SPECTRA FOR EQUAL DISPLACEMENT

Equivalent damping spectra ($R_{\mu-\zeta}-T$ spectra) are derived for estimating the maximum displacement of inelastic SDOF systems from the maximum displacement of equivalent linear SDOF systems. These spectra are derived for two types of equivalent linearization: direct implementation through equal displacement rule where the period or initial stiffness is not changed, and indirect implementation where the period is shifted in view of the expected displacement ductility of the inelastic system. The damping ratios required for equivalent linear systems in order to achieve similar maximum inelastic displacements are furnished by the associated $R_{\mu-\zeta}-T$ spectra.

5.1. Concept of Equal Displacement Rule

Estimating inelastic seismic response through dynamic analysis of an equivalent linear system has been a challenge in earthquake engineering due to obvious reasons. If the maximum displacement of a yielding system can be expressed in terms of the maximum displacement of an equivalent system, this is a significant advantage particularly for the preliminary design of a structural system, or the seismic assessment of an existing system. Linear elastic procedures do not require full characterization of ground motions for calculating maximum deformations. Their implementation through response spectrum analysis is far simpler compared to conducting nonlinear time history analysis under ground motion excitations. Furthermore, estimation of earthquake design spectra from seismic hazard analysis is quite straightforward whereas the generation of design ground motions require complex analytical procedures.

The basic features of equivalent linearization is schematized in Figure 5.1(a). An elasto-plastic system with an initial stiffness k and viscous damping ratio ξ_0 can be represented by an equivalent linear system with a reduced stiffness k' and an equivalent viscous damping ratio of ξ_{eq} such that its maximum displacement u_0 under earthquake excitation is equal to that of the elasto-plastic system. Jacobsen (1930) first introduced the concept of equivalent damping for linear elastic SDOF systems under steady state harmonic excitation where the damping force is a nonlinear function of velocity, then extended the concept to inelastic SDOF systems. Here the situation is more complicated because of the frequency and amplitude dependence of k' and ξ_{eq} . Different linearization procedures have been proposed in the past (Jacobsen 1960, Rosenblueth and Herrera 1964) in order account for the frequency dependence of equivalent linear system characteristics under harmonic excitations. Jennings (1968) compared equivalent viscous damping expressions from different approaches based on equal resonant amplitude, equal resonant frequency, equal critical damping and equal energy dissipation of elasto-plastic and equivalent linear systems under harmonic excitation, and concluded that equal amplitude approach is most suitable. Equivalent viscous damping ratios obtained from these approaches were significantly different.

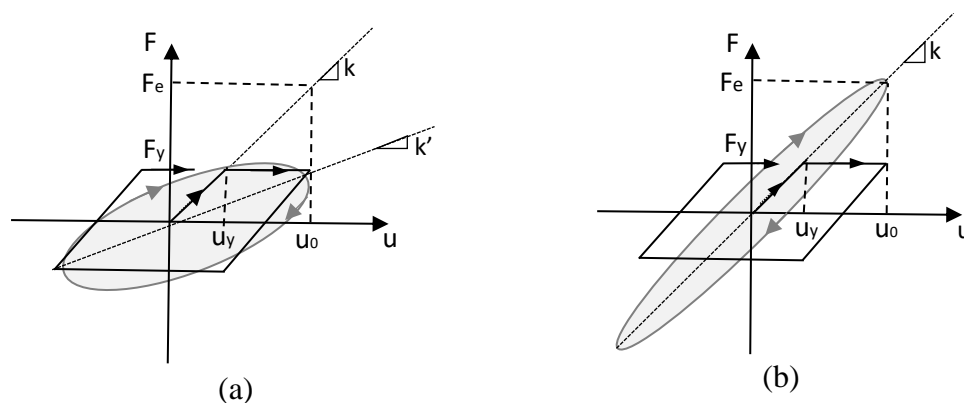


Figure 5.1. Typical equivalent linear systems, (a) with period shift, (b) without period shift

Gülkan and Sozen (1974) were the first researchers who investigated equivalent linear systems under earthquake excitation. Considering that equivalent damping ratios calculated for harmonic excitation are too conservative for earthquake excitation, they have defined a simple equivalent linear SDOF system with a period shift associated with the secant stiffness to the estimated maximum displacement, and proposed a period independent expression for equivalent damping in concrete structures based on shake table test results. Later Kowalsky (1994) has extended this approach to elasto-plastic systems with strain hardening. Iwan and Gates (1979) derived empirical expressions for equivalent period and damping of different hysteretic systems that provide the similarity of maximum displacements with least error. Quaranta and Mollaioli (2018) proposed similar empirical expressions for pulse type ground motions. Shibata and Sozen (1976) implemented equivalent linearization to the seismic design of MDOF concrete structures. They suggested reducing the stiffnesses of all yielding structural members, beams particularly, by an estimated ductility factor and applied the equivalent damping expression they derived for SDOF systems. Internal seismic design forces were calculated from this model by conducting response spectrum analysis.

An equivalent linear system can also be described without a period shift as shown in Figure 5.1(b). If it can be assumed that inherent viscous damping in the inelastic and linear elastic systems are the same, then this approach corresponds to the equal displacement rule. The rule was proposed by Veletsos and Newmark (1960) for mean maximum displacements of inelastic and linear elastic systems under a set of ground motions. Although equal displacement rule does not have a theoretical basis, and does not usually hold for individual ground excitations, it has introduced ultimate simplicity to seismic design. Newmark and Hall (1982) developed earthquake design spectra based on equal displacements at intermediate and long periods whereas the accelerations obtained from linear elastic spectra were reduced by the ductility factor. Similarity of inelastic and linear elastic mean maximum displacements under a suite

of ground motions have inspired several studies (Miranda 2000, Bozorgnia et al. 2010) for estimating the maximum inelastic displacement from linear elastic analysis. Usually these approaches employ modification factors that are effective at short periods and represent the variation of site conditions. Miranda and Ruiz-Garcia (2002) presented a comprehensive evaluation of equivalent linearization procedures for estimating the maximum inelastic displacements of SDOF systems from the analysis of equivalent linear elastic systems.

In this chapter, the main objective is to improve the maximum inelastic displacement predictions through linear elastic response analysis by introducing the $R_{\mu-\xi-T}$ spectra, and further extend its implementation to MDOF systems. Magnitude and distance dependence of inelastic to linear elastic maximum displacement ratio had been a subject of several valuable studies in the past; however, they did not necessarily agree on the effect of magnitude and distance on the displacement ratio (Miranda 2000, Chopra and Chintanapakdee 2004, Tothong and Cornell 2006). Since damping is an essential feature of the study presented in this chapter, the first step is a comprehensive investigation of damping efficiency in reducing maximum displacement response.

5.2. Damping Efficiency

Input energy and dissipated energy time histories of a 5% damped linear elastic system with a period of 1 second are shown in Figure 5.2(a). The ground motion excitation was recorded during the 1992 Cape Mendocino M_w 7.01 earthquake, at a fault distance of 10.4 km, on soil type C. Input energy accumulates at a specific rate, and viscous damping dissipates the accumulated input energy at a slower pace. The difference between the two energy time histories at a time t is the vibration energy $E_v(t)$, which is the sum of kinetic and potential energies at time t . Maximum displacement occurs shortly after E_v attains its maximum value during the following cycle when potential energy is maximum and kinetic energy is zero. This is shown in Figure 5.2(b). An efficient damping produces lower E_v , accordingly lower maximum displacement.

Hence, higher damping efficiency leads to faster dissipation of accumulated input energy imposed on the system by the ground excitation. However, energy dissipation rate varies quite erratically during earthquake ground excitations. It is rather chosen to define the damping efficiency, denoted by e_ξ , as a spectral parameter in Equation 5.1, which is the ratio of dissipated energy E_D to input energy E_I at the time t_{max} when $E_v(t)$ attains its maximum value for a SDOF system with period T .

$$e_\xi(T) = \frac{E_D(T)}{E_I(T)} \quad (5.1)$$

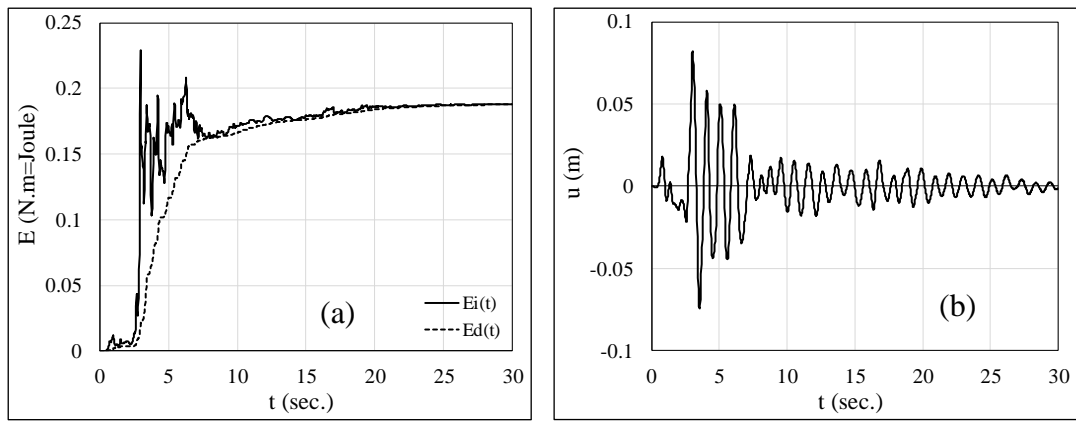


Figure 5.2. (a) Energy, (b) displacement time histories. $T=1$ sec., 5% damping

Damping efficiency for viscous damping is higher when e_ξ approaches 1, and lower when e_ξ approaches 0. The influence of earthquake magnitude, fault distance, soil type and fault type on damping efficiency are assessed here under the large set of ordinary earthquake ground motions employed in Chapter 3 that represent the distribution of such characteristics effectively.

5.2.1. Strong Ground Motions

The details of the large ground motion database were given in Section 3.1. For investigating damping efficiency, the ground motion database is divided into different groups with respect to ground motion related parameters. In this regard, Soil class (S), distance to epicenter (R_{epi}), moment magnitude (M_w), and fault mechanism are selected as the basic parameters in order to characterize source and site properties of ground motions. Based on the employed GM database, four M_w groups (5.5-6.0, 6.0-6.5, 6.5-7.0, >7.0), seven R_{epi} groups (<5 km, 5-10 km, 10-20 km, 20-30 km, 30-50 km, 50-100 km, >100 km), three fault types (normal, strike-slip, and reverse), and two soil types (stiff and soft) with respect to Figure 3.2 are considered in the evaluation.

5.2.2. Earthquake Magnitude

Figure 5.3 shows the variations of mean e_{ξ} for different M_w groups, two soil types and two R_{epi} groups. Fault type is reverse for all GM's in the figure. It is observed that damping efficiency is sensitive to earthquake magnitude, at all distance ranges irrespectively and for both soil types. Damping is more efficient at larger magnitudes in dissipating energy, hence in reducing the vibration energy. Note that there are no earthquakes in the $7.0 < M_w < 7.5$ range at the distances considered in Figure 5.3.

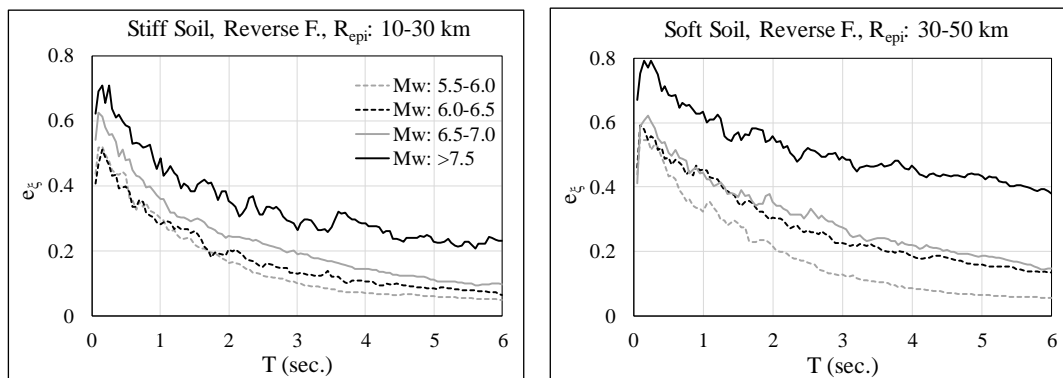


Figure 5.3. The effect of M_w on e_{ξ} for both soil types and two R_{epi} groups

5.2.3. Fault Distance

Damping efficiency spectra presented in Figure 5.4 reveal that damping efficiency increases with epicentral distance, although this sensitivity is not strong. The figures also indicate a grouping for $R_{epi} < 30$ km (near fault) and $R_{epi} > 30$ km (far fault). Accordingly, the near fault ground motions will be considered separately in this study.

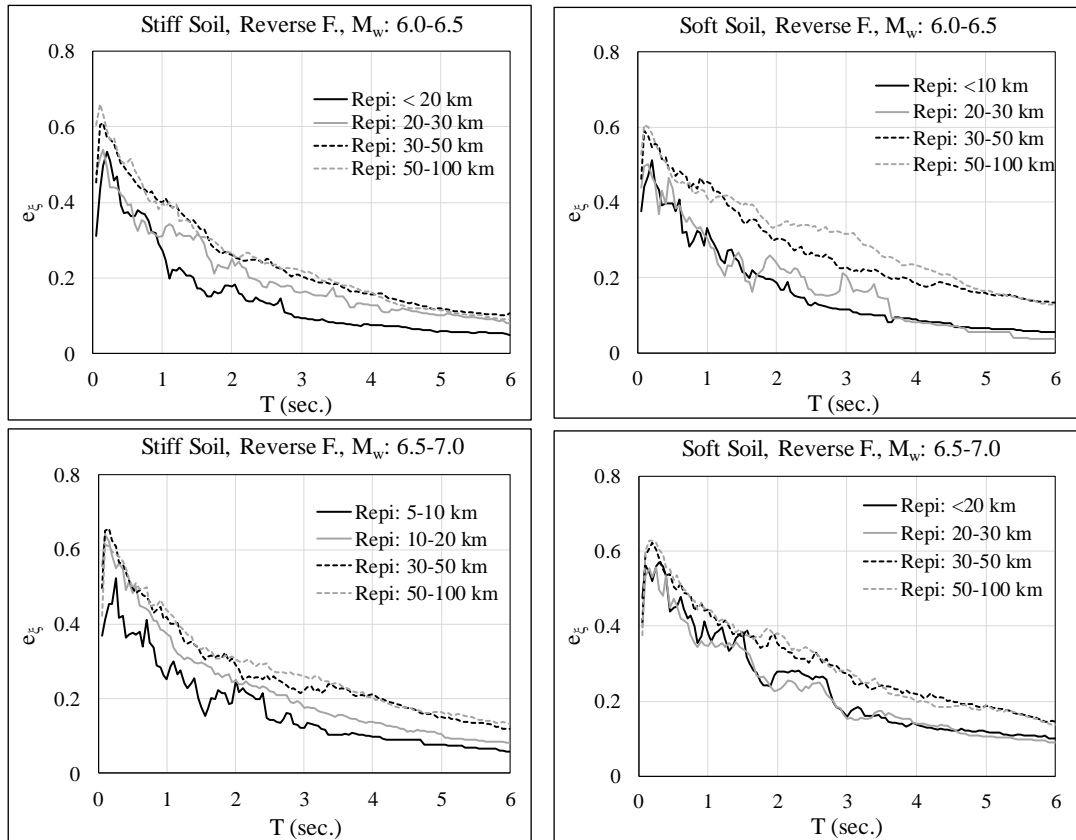


Figure 5.4. The effect of R_{epi} on e_z for both soil types and two M_w groups

5.2.4. Fault Type

Damping efficiency spectra is obtained for all three fault types, for the ground motions in the 6.0-6.5 magnitude range, and at near fault distances. The results shown in Figure

5.5 do not indicate a consistent sensitivity of damping efficiency to the fault type. The trends are similar for longer fault distances.

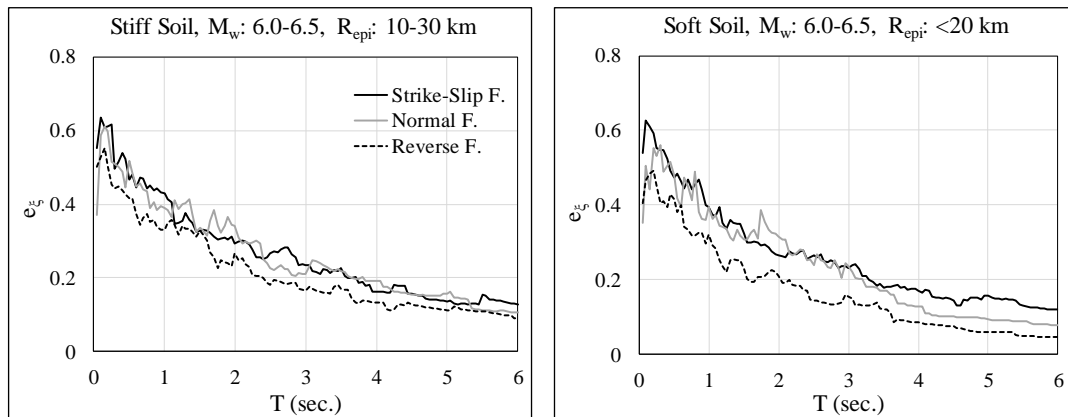


Figure 5.5. The effect of fault type on e_z for both soil types and two R_{epi} groups

5.2.5. Soil Type

The effect of soil type (stiff and soft) on damping efficiency is presented in Figure 5.6 for two magnitude groups and two distance groups. It is quite clear from both group of curves that soil type has no influence on damping efficiency, regardless of the magnitude and distance of ground motions.

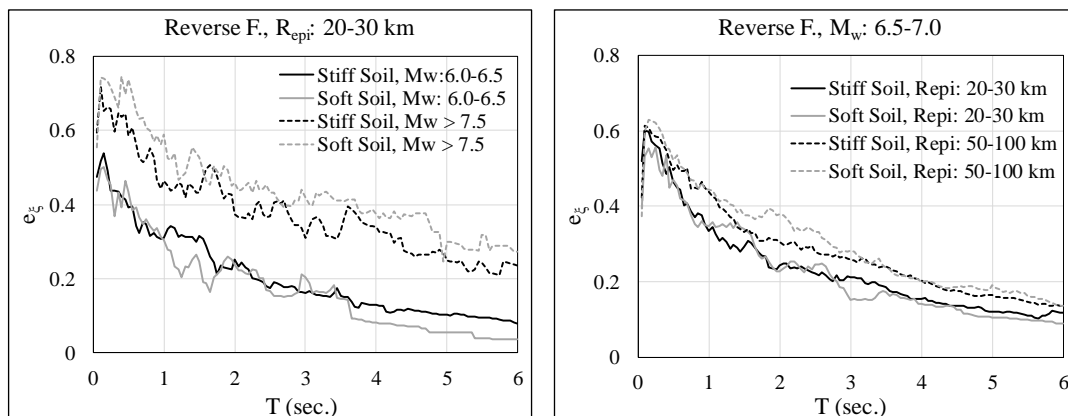


Figure 5.6. The effect of soil type on e_z for two magnitude and R_{epi} groups, respectively

5.2.6. Remarks on Damping Efficiency

The observations from Figure 5.3 to Figure 5.6 reveal the following remarks:

1. The effect of damping reduces with period. This is of course not a new observation. The $R_{\mu-\xi-T}$ spectra developed in the following sections consider this directly.
2. Damping efficiency increases with magnitude. Therefore, $R_{\mu-\xi-T}$ spectra should consider magnitude sensitivity, explicitly.
3. Damping efficiency reduces under near fault ground motions, but increase slightly under ground motions from far fault distances. Hence, the $R_{\mu-\xi-T}$ spectra will be developed separately for near fault ground motions.
4. The effects of fault type and soil type on damping efficiency are insignificant.
5. These remarks based on the observations from damping efficiency spectra of linear elastic systems, are also valid for inelastic systems where inelastic response is expressed by R_{μ} . Damping efficiency pertaining to inelastic systems are not presented here for brevity; however, the sensitivity of damping efficiency spectra of inelastic systems to the same parameters were almost similar.

5.2.7. Classification of Strong Ground Motions

The remarks presented in the previous section above particularly related to strong motion characteristics reveal that magnitude is the most influential parameter regarding damping efficiency. Furthermore, near fault ground motions exhibit less sensitivity to damping. Accordingly, $R_{\mu-\xi-T}$ spectra developed in this study are calculated separately for the four magnitude groups, and for ordinary and near-fault ground motions, respectively. The properties of NF ground motion database were

given in Section 4.1. Near fault ground motions are grouped similarly with respect to magnitude M_w .

The mean acceleration response spectra of the four magnitude groups for ordinary and near fault ground motions are shown in Figure 5.7. Although the two magnitude groups below $M_w 6.5$ and above $M_w 6.5$ display a grouping for both ground motion types, their spectral response distributions are different for short and long period systems.

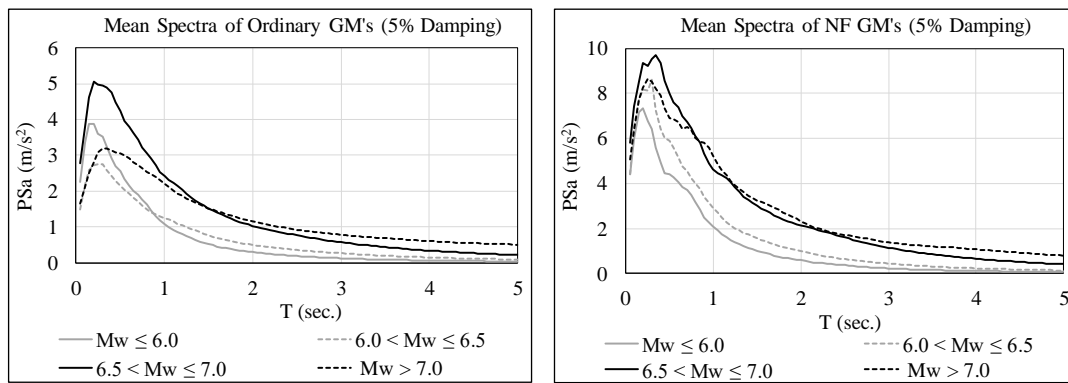


Figure 5.7. Five percent damped mean acceleration response spectra of ordinary and near fault ground motions for four M_w Groups.

5.3. Computation of $R_{\mu-\xi}-T$ Spectra

$R_{\mu-\xi}-T$ spectra for two different cases that was shown in Figure 5.1 are developed herein. When there is a period shift (Figure 5.1(a)), it is called “equivalent linearization procedure” and when the initial period is kept constant (Figure 5.1(b)), this is called “equal displacement rule” in this study. Since the implementation of equal displacement rule is simpler, the results for this case will be presented first.

5.3.1. R_μ - ζ - T Spectra for Equal Displacement Rule

Let us consider a linear elastic and an elasto-plastic SDOF system with the same initial stiffness and mass, i.e. identical initial period T_k , subjected to the same ground excitation GM_j . The elasto-plastic system is assigned an inherent viscous damping ratio of 2% that is lower than the commonly accepted 5% for linear elastic systems because viscous damping is less in inelastic systems exhibiting hysteretic energy dissipation. Employing 2% viscous damping in inelastic systems was first proposed by Gülkan and Sozen (1974), and justified with test data. It is an accepted practice for the inelastic time history analysis of tall buildings under maximum considered ground motion excitations (TBI 2017) where hysteretic energy dissipation is significant. Assuming larger viscous damping for inelastic systems is not reasonable because it masks the actual hysteretic response under earthquake ground excitations. The yield strength of the elasto-plastic system is determined from the response spectrum of GM_j at period T_k by employing a ductility reduction factor R_μ .

Dynamic responses of both the linear elastic system with an arbitrary damping ζ_{eq} and the elasto-plastic system with $\zeta=2\%$ and R_μ are calculated under the GM_j and the ratio of their maximum displacements are registered with the tensor $r_{j,k}$ defined below.

$$r_{j,k} = \frac{u_e(T_k, GM_j, \zeta_{eq})}{u_{ep}(T_k, GM_j, \zeta_{0.02}, R_\mu)} \quad (5.2)$$

In Equation 5.2, u_{ep} and u_e are the maximum displacement responses of the elasto-plastic and elastic SDOF systems, respectively, and ζ_{eq} is the arbitrary damping ratio assigned to the linear elastic system. The unknown in Equation 5.2 is ζ_{eq} , and its correct value is the one which makes $r = 1$. It should be noted however that obtaining $r = 1$ exactly cannot be possible for all ground motions. The best solution for ζ_{eq} that provides $r \approx 1$ is determined through numerical search for each GM_j , by varying ζ_{eq} with small increments. Then the median values of ζ_{eq} at T_k are determined for the entire

GM set. This procedure is repeated for a range of T_k values, and five different R_μ values, from 2 to 6. Accordingly, ξ_{eq} versus T_k relation for R_μ gives the $R_\mu-\xi-T$ spectra. They are presented in Figure 5.8 for four different M_w groups of ground motions.

Figure 5.8 reveals that less than the commonly accepted 5% equivalent damping is required for shorter period linear elastic SDOF systems for correctly estimating the maximum displacements of elasto-plastic systems with 2% viscous damping. As the magnitude gets larger, short period range lengthens from approximately 0.5 second for $M_w < 6$ to 4 seconds for $M_w > 7$. Assuming 5% damping for equivalent linear systems in the general implementation of equal displacement rule coincidentally corresponds to correct damping values for some cases.

Larger equivalent damping ratios are required for smaller magnitude earthquakes in order to maintain the maximum displacement equality with the associated elasto-plastic systems, as evidenced in Figure 5.8. This is a consequence of Figure 5.3, which indicates that damping is less efficient for small magnitude earthquakes in reducing vibration energy.

A similar exercise is carried out for the 157 pairs of near fault ground motions, grouped similarly with respect to magnitude M_w . The $R_\mu-\xi-T$ spectra obtained for the near fault ground motions are shown in Figure 5.9. A comparison of Figure 5.8 and Figure 5.9 indicates that slightly higher damping ratios are required at longer periods for the validity of equal displacement rule under near fault ground motions, as compared to ordinary ground motions. This difference can be explained in view of Figure 5.4. Damping efficiency reduces for near fault ground motions. Hence, larger equivalent damping ratios are necessary for linear elastic systems in order to satisfy the equality of maximum displacements with those of the inelastic systems under near fault ground motions.

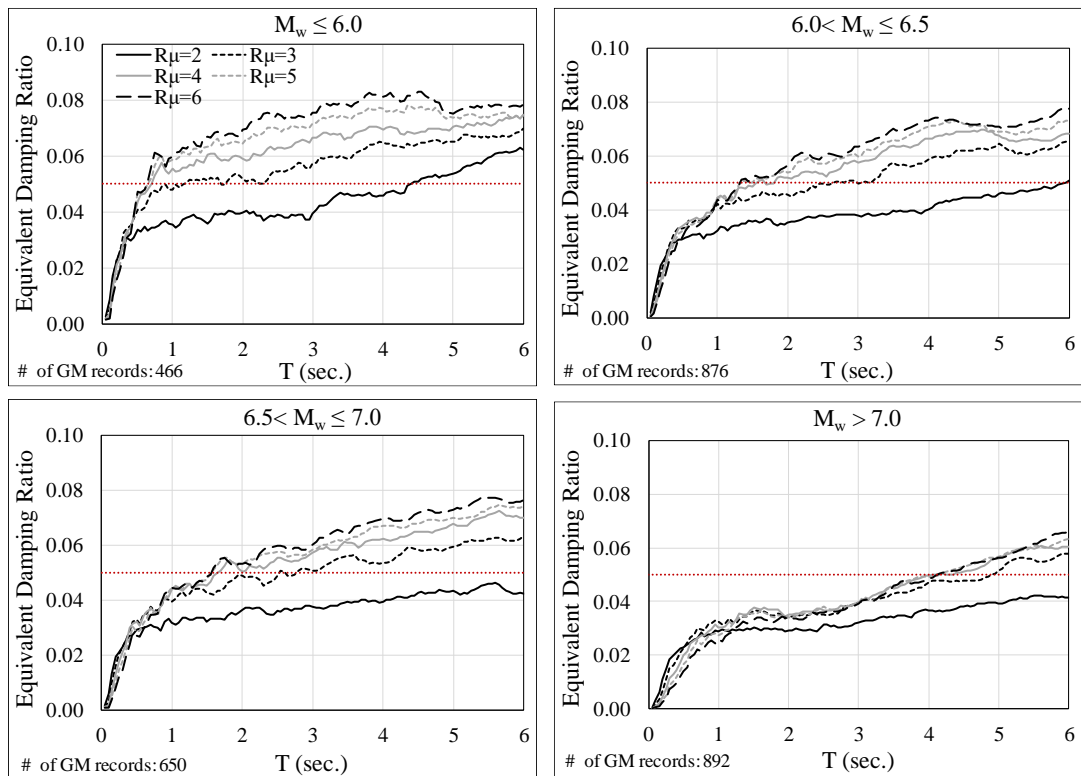


Figure 5.8. Mean $R_\mu-\xi-T$ spectra for equal displacement rule: Ordinary ground motions

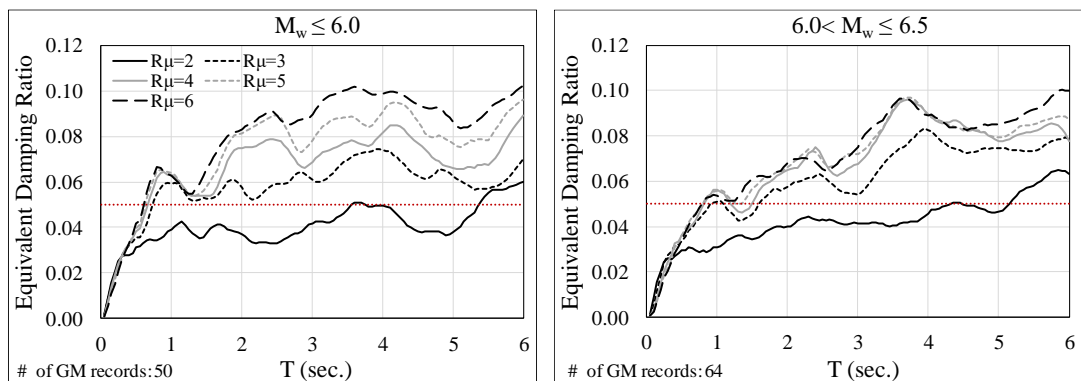


Figure 5.9. Mean $R_\mu-\xi-T$ spectra for equal displacement rule: Near fault ground motions

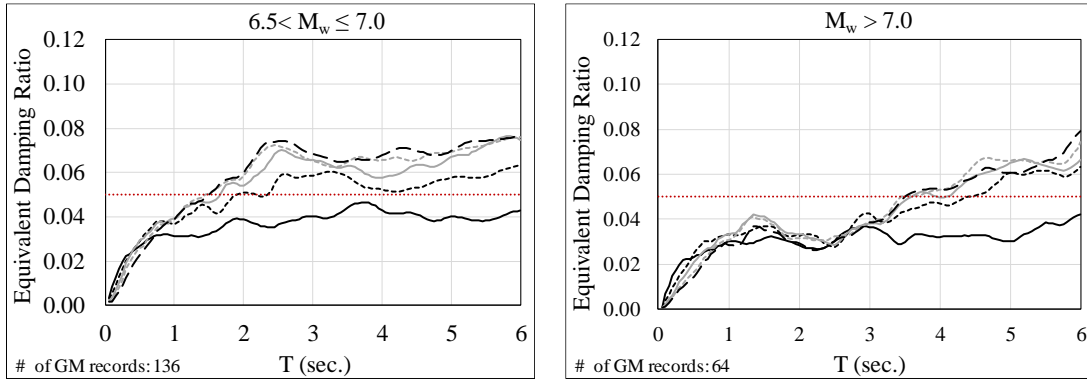


Figure 5.9. (Continued)

5.3.2. R_μ - ξ - T Spectra for Equivalent Linearization with Period Shift

The procedure is quite similar to that of equal displacement rule presented above, but with the difference of period shift. The numerator in Equation 5.2 for the inelastic system is the same, however T_k becomes $T_{k,j}$ for the equivalent linear system. Dynamic response of the elasto-plastic system with 2% damping and yield strength associated with R_μ is calculated first under GM_j . Then the shifted period is calculated from Equation 5.3.

$$T_{k,j} = T_k \sqrt{\mu_j} \quad (5.3)$$

Here μ_j is the ductility demand from the elasto-plastic system, calculated by nonlinear time history analysis under GM_j . Equation 5.3 directly follows from Figure 5.1(a). Accordingly, Equation 5.2 is modified as below.

$$r_{j,k} = \frac{u_e(T_{k,j}, GM_j, \xi_{eq,j})}{u_{ep}(T_k, GM_j, \xi_{0.02}, R_\mu)} \quad (5.4)$$

The corresponding $\zeta_{eq,j}$ of the equivalent linear system with $T_{k,j}$ is calculated similarly through a search algorithm for GM_j in order to satisfy $r_{j,k} \approx 1$. A practical problem arises here though, because there is no single T_k but a different $T_{k,j}$ for each GM_j . However, they are usually bundled around $T_k \sqrt{R_\mu}$ where R_μ is constant for all GM_j . We have selected a narrow period band around $T_k \sqrt{R_\mu}$ in the digital $(\zeta_{eq,j} - T_{k,j})$ plane, and calculated the mean values of $T_{k,j}$ and $\zeta_{eq,j}$ falling into the selected band. Accordingly, the mean $\zeta_{eq,j}$ versus mean $T_{k,j}$ relation for R_μ gives the R_μ - ζ - T spectra. They are presented in Figure 5.10 for four different M_w groups of ground motions.

It was observed from Figure 5.8 for the equal displacement rule that damping ratio is less effective for smaller magnitudes and more effective at larger magnitudes. However, the trend is almost the opposite for the equivalent linearization procedure in Figure 5.10. An interesting observation is on the effective damping suggested by Güllkan and Sozen (1974), which is period independent. It yields 8%, 12% and 14% equivalent damping ratios for $R_\mu = 2, 4$ and 6 , respectively. If μ is taken approximately equal to R_μ in their suggested equation, then the proposed values display somewhat the average values along period (except for $M_w > 7$), although period dependence is seemingly quite significant. $\zeta_{eq} = 0.12$ is marked on Figure 5.10.

Mean R_μ - ζ - T spectra for the equivalent linearization procedure are also obtained under the near fault ground motions by following the same procedure above. These spectra for different magnitude groups are presented in Figure 5.11. R_μ - ζ - T spectra obtained under ordinary and near-fault ground motions are not very different from each other in the case of equivalent linearization, implied by the comparison of Figure 5.10 and Figure 5.11.

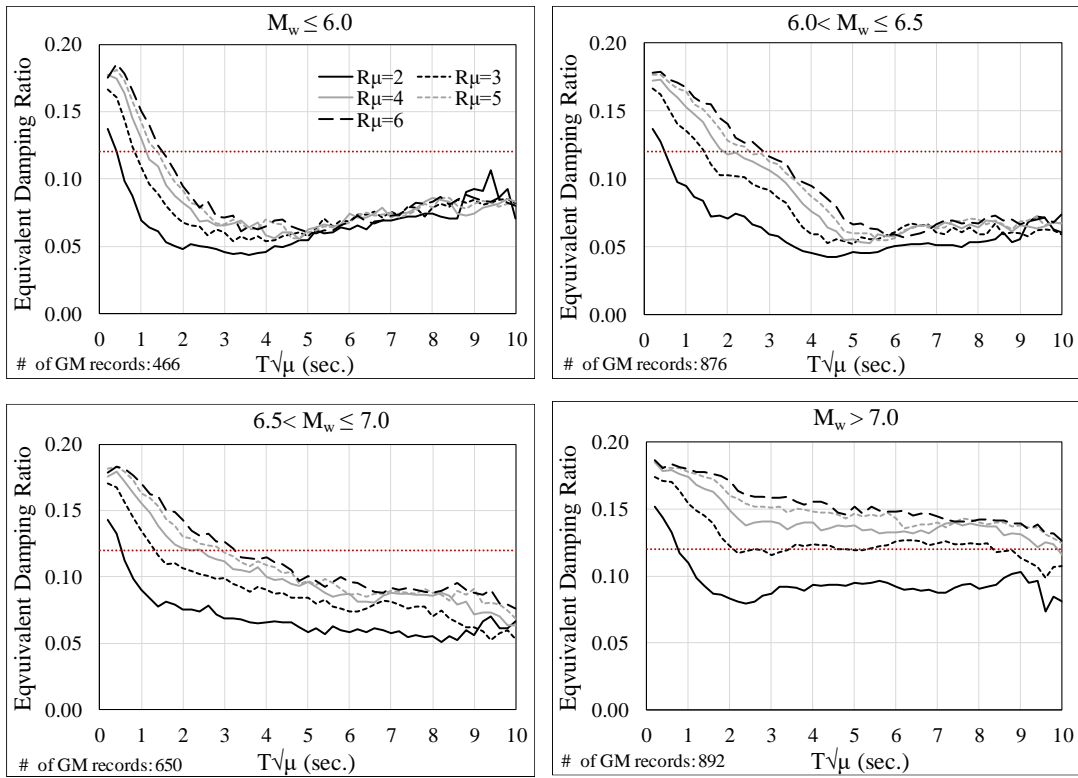


Figure 5.10. Mean R_{μ} - ξ - T spectra for equivalent linearization with period shift: Ordinary ground motions

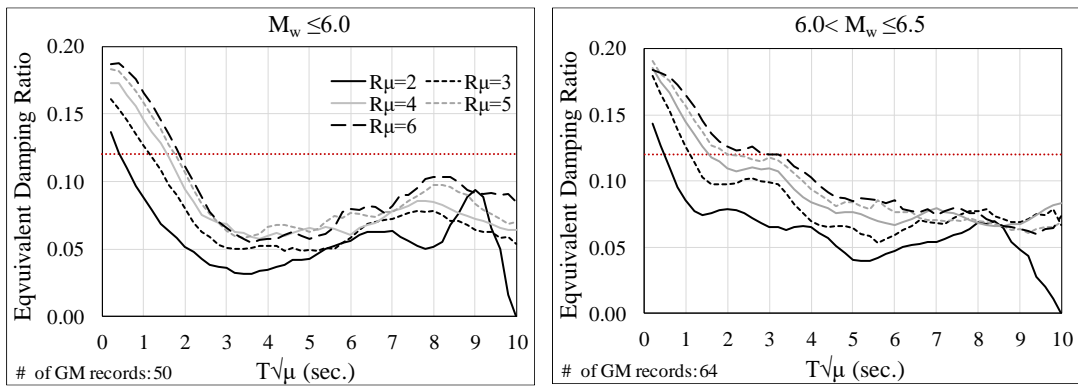


Figure 5.11. Mean R_{μ} - ξ - T spectra for equivalent linearization with period shift: Near fault ground motions

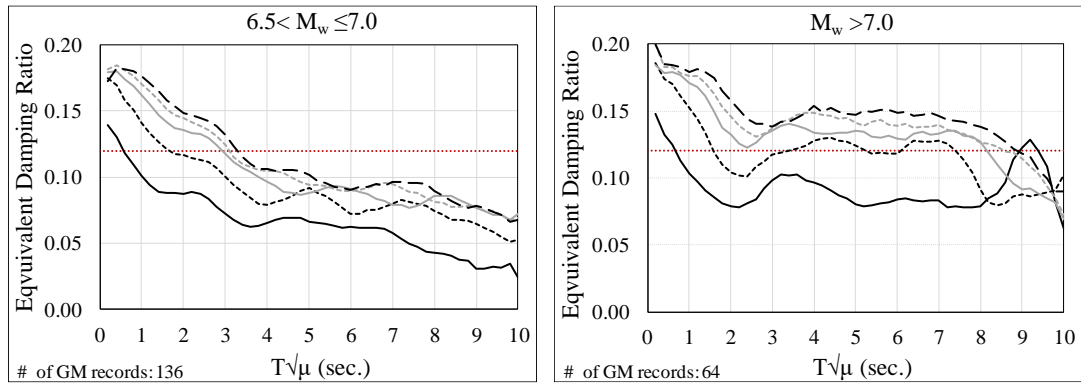


Figure 5.11. (Continued)

5.4. Comparative Evaluation of Equivalent Linearization Procedures

Three different equivalent linear procedures are compared here. The first one is the classical equal displacement rule implemented with 5% damping, and the second one is the equal displacement rule modified with the proposed $R_{\mu-\zeta}-T$ spectra. The third one is equivalent linearization with period shift where equivalent damping is taken from the $R_{\mu-\zeta}-T$ spectra derived herein. Elastic to inelastic maximum displacement ratios of SDOF systems are calculated for three M_w groups and $R_{\mu} = 4$, by employing Equations 5.2 and 5.4, and the associated $R_{\mu-\zeta}-T$ spectra proposed in this study. Inherent damping ratio for the inelastic systems is 2%.

The median values and standard deviations of r are compared in Figure 5.12 and Figure 5.13, for ordinary and near fault ground motions, respectively. Apparently, the modified equal displacement rule satisfies the intended target value of $r = 1$ for all M_w groups and for both types of ground motions along the entire period range, except at very short periods. Equal displacement rule with 5% damping is also quite satisfactory for both ordinary and near fault ground motions, however it underestimates inelastic displacements at short and moderate periods for larger magnitude groups. On the other hand, equivalent linearization procedure with period shift yields median results that deviate significantly from the target $r = 1$ in all cases. In Figure 5.12 and Figure 5.13,

the period is the “unshifted” period corresponding to the initial stiffness in order to facilitate comparison.

The average values of standard deviations along the period axes for all M_w groups and both strong motion types are around 0.3 for both the equal displacement rule and the modified equal displacement rule, whereas it is larger for the equivalent linearization procedure with period shift. When the median and standard deviations obtained from the three procedures are evaluated comparatively, the modified equal displacement procedure appears as the more accurate method regarding least median errors and lesser standard deviations. Although the implementation of equivalent linearization procedure with period shift is more demanding in practice since it requires an initial estimation of displacement ductility, it does not provide any particular advantage. In fact, it is least successful in view of the results presented in Figure 5.12 and Figure 5.13.

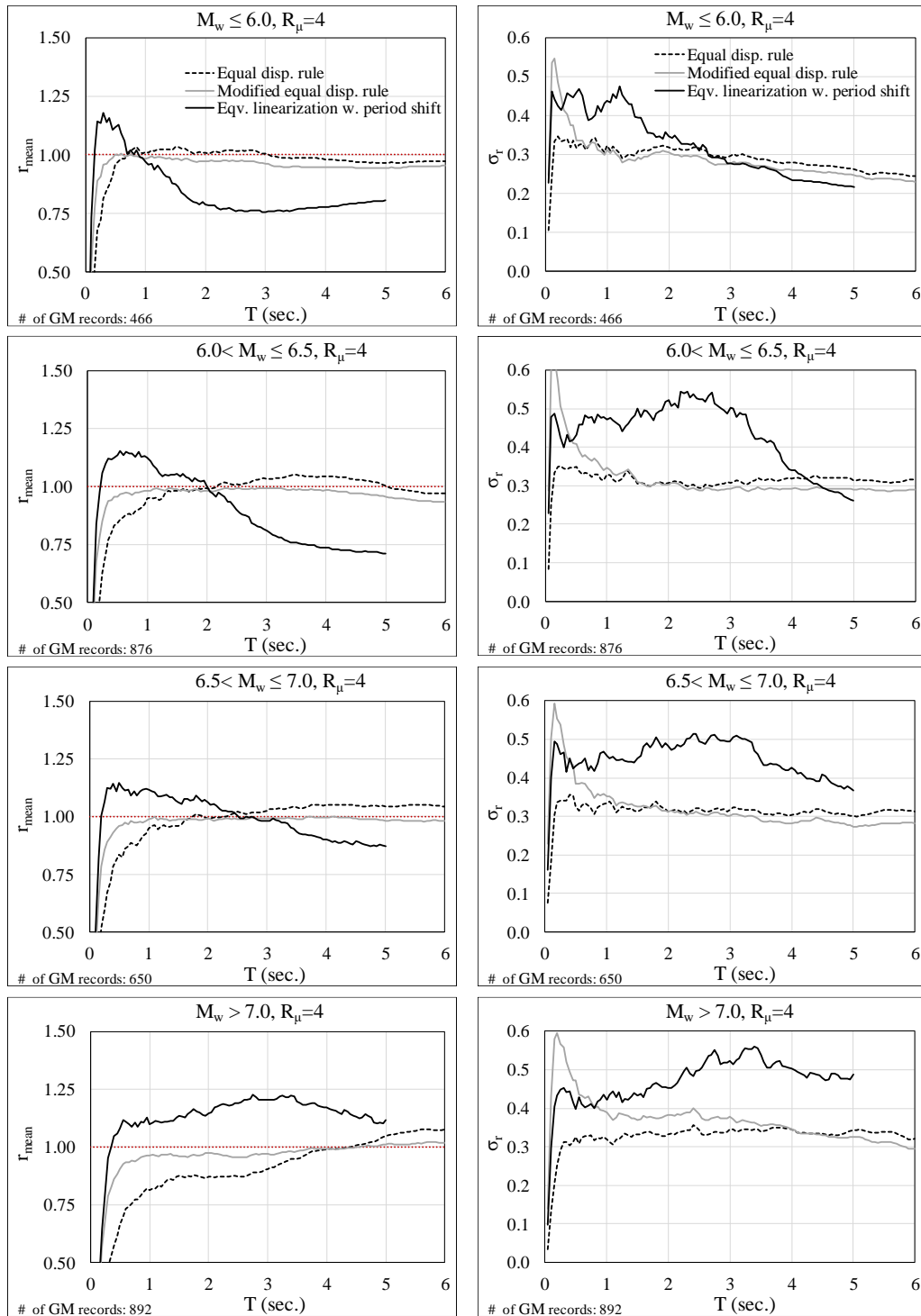


Figure 5.12. Comparison of median and standard deviation of maximum displacement ratios of elastic to inelastic SDOF systems: Ordinary ground motions

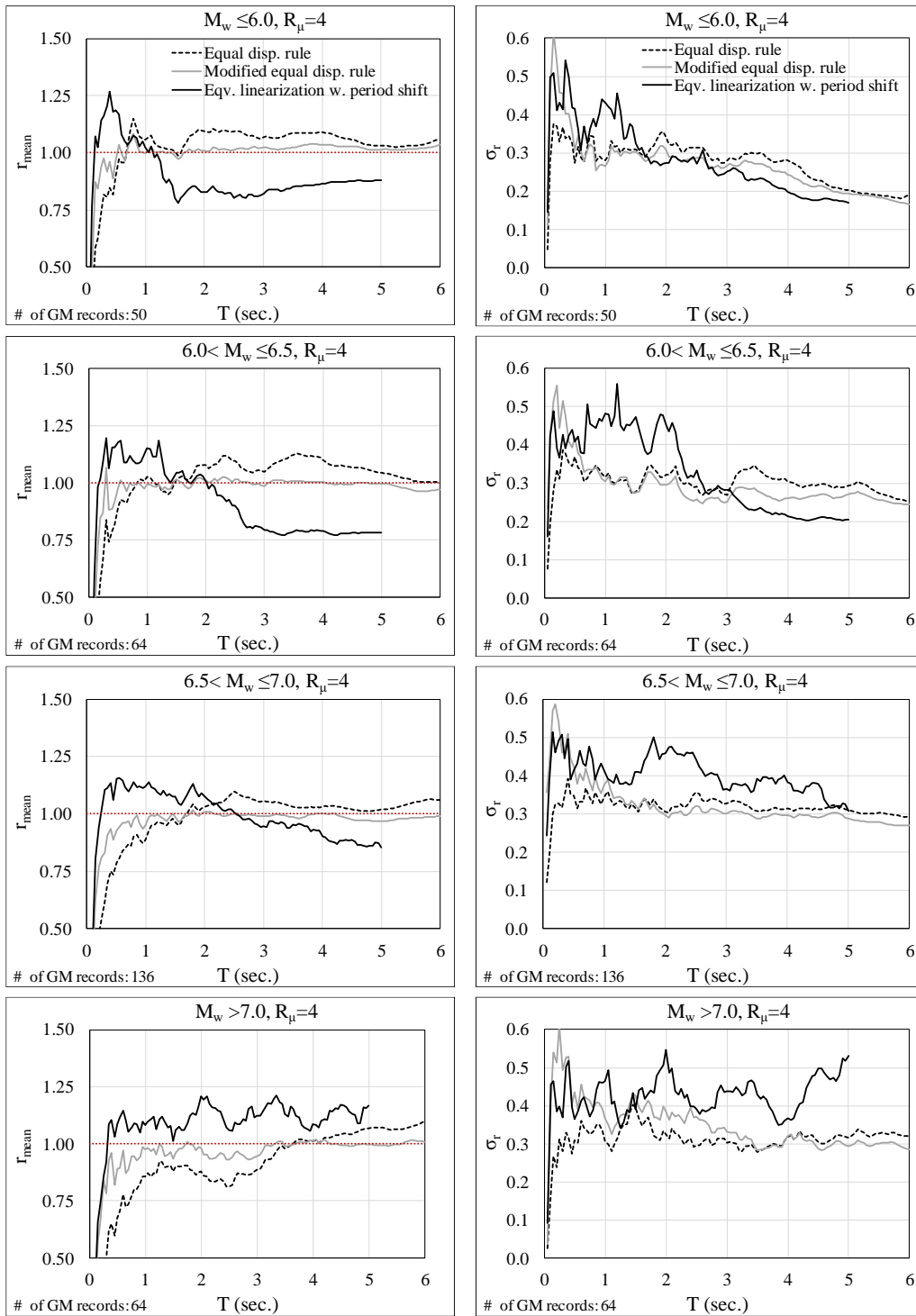


Figure 5.13. Comparison of median and standard deviation of maximum displacement ratios of elastic to inelastic SDOF systems: Near fault ground motions

5.5. Implementation of Equivalent Linearization Procedures for the Response Prediction of a 5 Story Frame

A five-story reinforced concrete frame with the plan and elevation views shown in Figure 5.14 is designed under the design spectrum specified for a high seismicity region in California in accordance with the seismic code regulations (ASCE 2010), by employing a response reduction factor of $R=8$. The column dimensions are $50 \times 40 \text{ cm}^2$ and beam dimensions are $50 \times 30 \text{ cm}^2$ for the entire structure. The cross-sections of beams and columns with the longitudinal reinforcement information and shear reinforcement detailing are shown in Figure 5.15. Characteristic strengths of concrete and steel are 25 MPa and 420 MPa, respectively. Free vibration properties of the five story R/C frame are calculated by eigenvalue analysis of the linear elastic model with cracked stiffness values, which are obtained by multiplying the gross moment of inertias by 0.35 and 0.70 for beams and columns, respectively. Modal information regarding the first three modes is tabulated in Table 5.1. From the table, the first and second modal vibration periods are 0.94 s and 0.28 s, with the corresponding modal mass ratios of 0.80 and 0.11, respectively. Total mass is 260 tons. The capacity curve obtained from the first mode pushover analysis, shown in Figure 5.14, indicates a lateral load capacity of 410 kN.

This building is analyzed under the ordinary and near fault ground motions sets with the magnitude range of $6.5 < M_w < 7.0$. There are 650 and 136 ground motions in these two sets, respectively. Their 5% damped mean acceleration response spectra were shown in Figure 5.7.

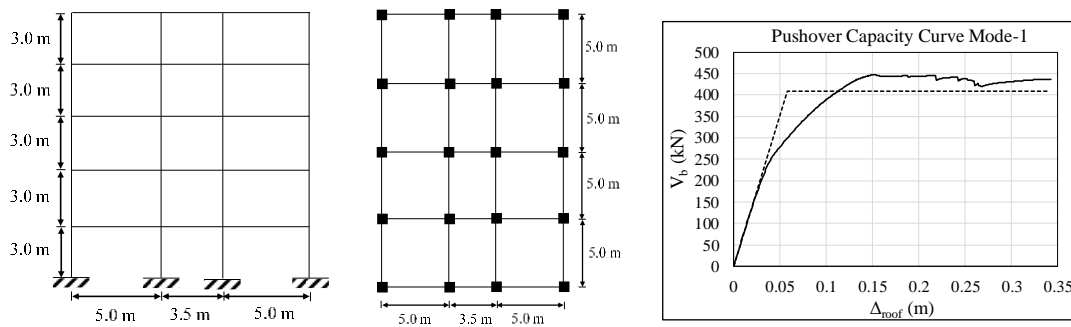


Figure 5.14. Elevation and plan views of the 5-story frame, and capacity curve from first mode pushover analysis

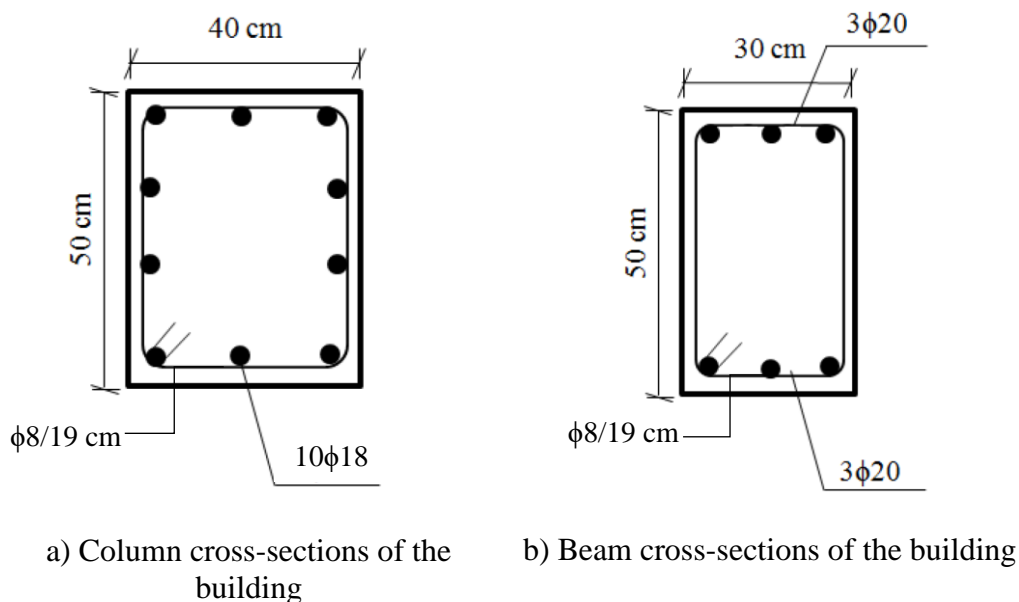


Figure 5.15. Cross-section details of columns and beams of five story building

Table 5.1. Free vibration properties of the first three modes of five story R/C frame

Mode #	T (sec.)	Effective Modal Mass (tons)	Effective Modal Mass Ratio
1	0.94	208.11	0.80
2	0.28	28.96	0.11
3	0.15	12.25	0.05

The frame is first analyzed under each ground motion by conducting nonlinear response history analysis (NRHA). These results are considered as the benchmark. Then three different equivalent linear procedures are applied for calculating the frame deformations, namely lateral story displacements, interstory drift ratios, beam and column end-rotations. R_μ values are required in order to utilize the R_μ - ζ - T spectra for estimating the deformations from equivalent linear procedures.

It is possible to infer the realized R_μ values for each ground motion set by employing their mean spectral acceleration at the first mode, and the frame lateral load capacity. Simply, Equation 5.5 can be employed to obtain R_μ values.

$$R_\mu = \frac{M_{tot} \cdot S_a(T_1)}{F_y} \quad (5.5)$$

Where M_{tot} is the total mass of the building, $S_a(T_1)$ is the first mode spectral acceleration from mean ground motion spectra of the associated ground motion set, and F_y is the frame lateral load capacity from first mode pushover analysis that is presented in Figure 5.14 above. The calculated R_μ values for the ordinary and near fault ground motion sets are 1.6 and 3.1, respectively. These R_μ values are employed as 2 and 3 respectively for obtaining the equivalent modal damping ratios from Figure 5.8 and Figure 5.9 in the implementation of Modified Equal Displacement Rule. This assumption corresponds to employing a single response reduction factor for all modes in seismic design. For practical purposes, considering that F_y is not available from capacity analysis, R_μ can be estimated from Equation 5.6 where Ω_0 is the overstrength factor.

$$R_\mu = R / \Omega_0 \quad (5.6)$$

Ω_0 is suggested as 3 and R as 8 in ASCE-7-10 (2010) for special (ductile) reinforced concrete moment frames, leading to $R_\mu = 2.67$. This value falls somewhere in between the calculated values from Equation 5.5.

This approach however is not valid for the implementation of Equivalent Linearization Procedure with Period Shift. Equivalent modal damping ratios should be obtained from the $R_\mu-\zeta-T$ spectra given in Figure 5.10 and Figure 5.11 where modal ductility ratios are required for obtaining the shifted modal periods. This is the major difficulty in implementing the Equivalent Linearization Procedure with Period Shift to MDOF systems. An intuitive but a practical solution is sought here, where R_μ calculated above for the first mode is assumed equal to the first mode ductility ratio, and the higher modes are assumed as linear elastic with 5% damping.

Mean displacement results calculated by NRHA, and from the three equivalent linear procedures under the mean spectra of ordinary and near fault ground motions are presented in graphical form in Figure 5.16 and Figure 5.17, respectively. It can be inferred from ordinary and NF ground motion results that the Equivalent Linearization Procedure with Period Shift gives larger response values when compared to those obtained from the other equal displacement rule methods. This situation was also observed from the figures (Figure 5.12 and Figure 5.13) obtained in the previous section, where the obtained displacement ratios from this procedure were larger than one ($r > 1$) for the period values of the frame considered. On the other hand, the Modified Equal Displacement Rule improves the classical equal displacement rule predictions at the lower story levels. It can be observed especially from story displacement, beam and column chord rotation graphs presented below. The lower stories are the potential locations for plastic hinges as in plastic rotation distribution obtained from NRHA shown in Figure 5.16 and Figure 5.17; therefore, predicting displacement response at these story levels more accurately with respect to the

benchmark results will become important for energy based design approach introduced in the following chapter.

Maximum beam-end and column-base plastic rotations obtained from NRHA indicated in both figures reveal significant yielding at the lower stories under both types of ground motions.

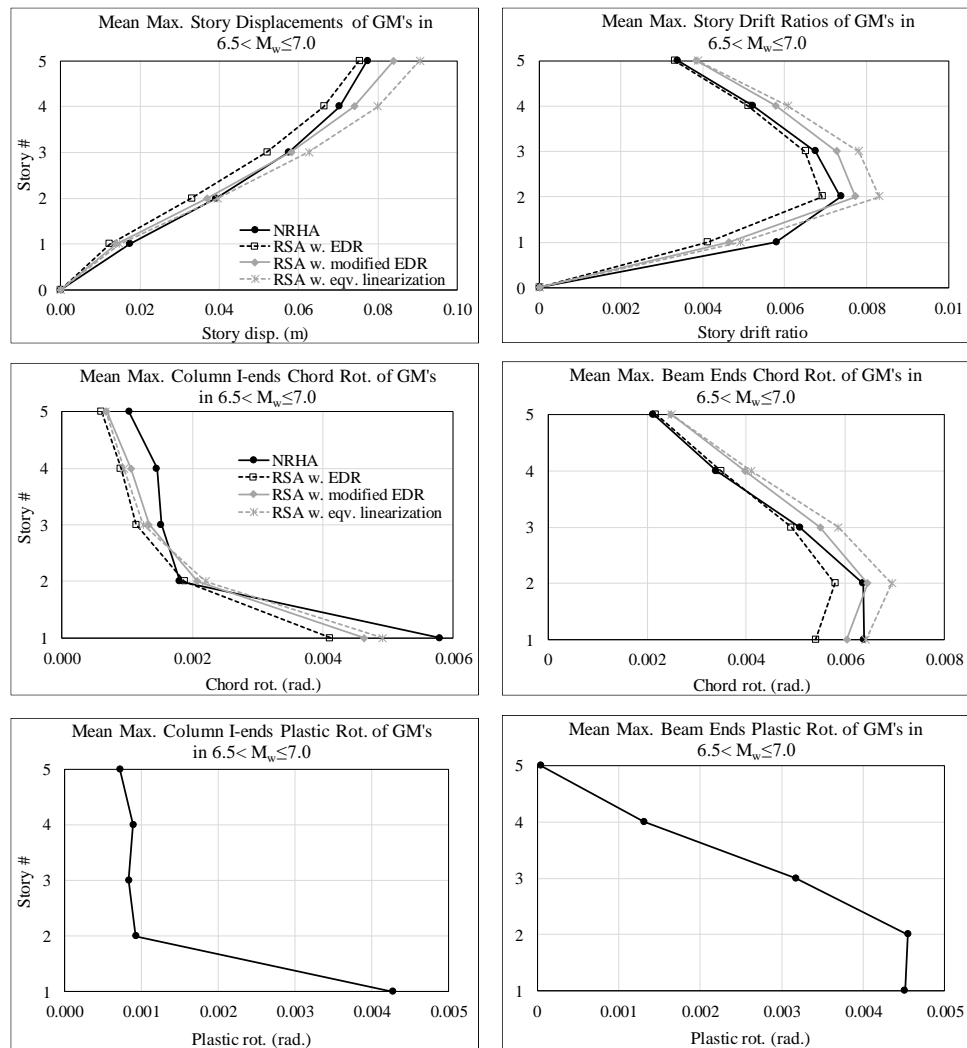


Figure 5.16. Mean maximum story displacements, interstory drift ratios, column bottom-end and beam-end chord rotations and plastic end rotations of the 5-story frame under ordinary ground motions

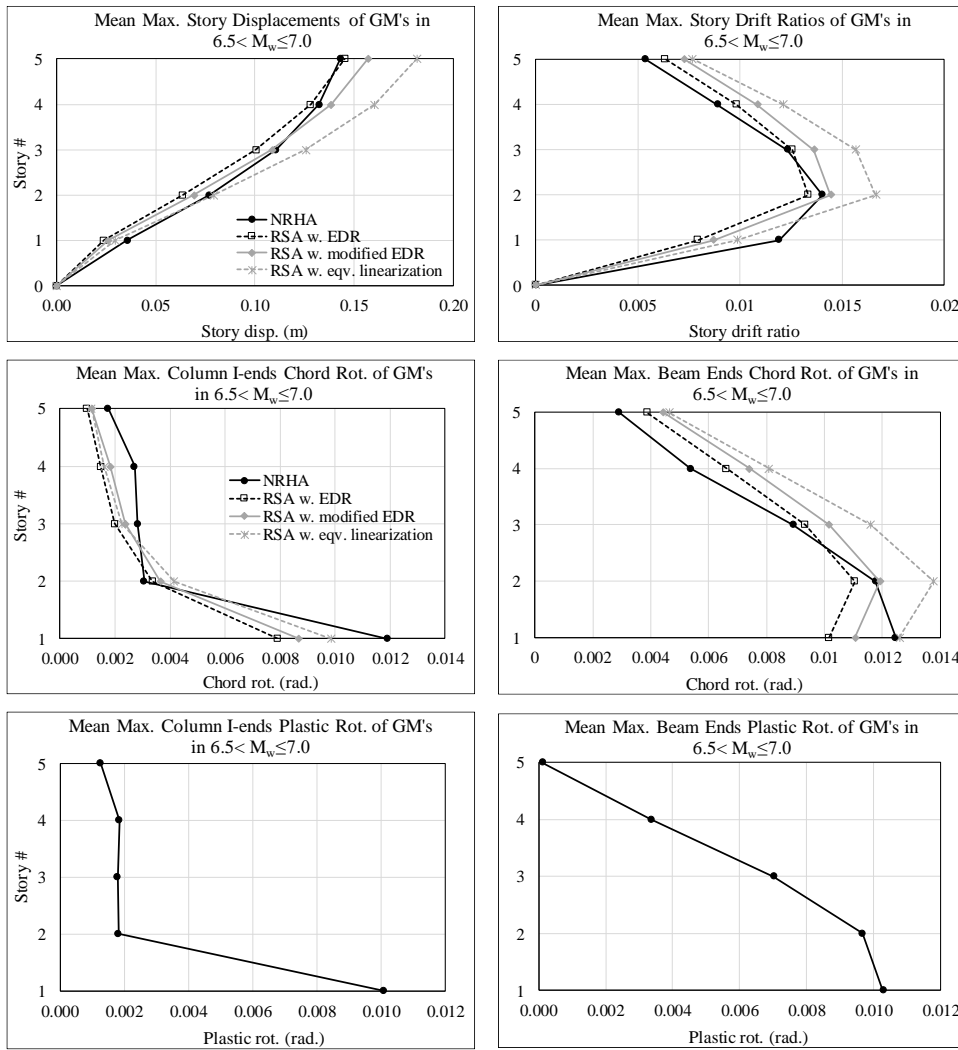


Figure 5.17. Mean maximum story displacements, interstory drift ratios, column bottom-end and beam-end chord rotations and plastic end rotations of the 5-story frame under near fault ground motions

CHAPTER 6

AN ENERGY BASED ASSESSMENT AND DESIGN PROCEDURE

The main objective of the design procedure introduced in this chapter is to improve the classical seismic design approach, but not to overrule it. Thus, the initial step of the procedure is to conduct a preliminary design of the building in which vertical gravity loads and earthquake design loads from a seismic design code are considered. The new approach on the other hand includes determination of the amount of energy the structure can absorb and dissipate under an earthquake excitation. The amount of energy dissipated by the inelastic response of structural members in turn corresponds to the damage, or seismic performance of the structure. Therefore, the main objective of the proposed method is to predict the energy dissipation mechanism of a structural system, and to determine the amount and location of plastic hinges throughout the structure that is required to dissipate the seismic input energy imparted by seismic excitation efficiently. In this regard, the energy equilibrium equations for MDOF systems are derived first, and then the new method based on the previous statements is elaborated and verified for seismic assessment and design.

6.1. Energy Equations for MDOF Systems

The equation of motion under a base excitation for a MDOF system has the same form with the equation used for SDOF systems, but scalar displacement related variables are replaced with the vectorial displacement variables. Similarly, the scalar mass, stiffness, and damping property terms are replaced with the associated matrix terms. The equation of motion for MDOF system is given in Equation 6.1, where \underline{m} , \underline{c} and \underline{k} are mass, viscous damping and stiffness matrices of the MDOF system respectively. Here, \underline{u} is the relative displacement vector of the MDOF system with respect to the

ground, \ddot{u}_g is the earthquake ground acceleration and \underline{l} is the influence vector for ground acceleration.

$$\underline{m} \ddot{\underline{u}} + \underline{c} \dot{\underline{u}} + \underline{k} \underline{u} = -\underline{m} \underline{l} \ddot{u}_g \quad (6.1)$$

The displacement vector $\underline{u}(t)$ can be expressed as a linear combination of the orthogonal modal shape vectors:

$$\underline{u}(t) = \sum_{n=1}^N q_n(t) \underline{\phi}_n \quad (6.2)$$

After substituting $\underline{u}(t)$ in Equation 6.2 into Equation 6.1, the equation of motion is converted into modal coordinates as shown in Equation 6.3.

$$\underline{m} \sum \ddot{q}_n \underline{\phi}_n + \underline{c} \sum \dot{q}_n \underline{\phi}_n + \underline{k} \sum q_n \underline{\phi}_n = -\underline{m} \underline{l} \ddot{u}_g \quad (6.3)$$

Pre-multiplying each term in Equation 6.3 with $\underline{\phi}_r^T$, and invoking the orthogonality of modes, only those terms with $r=n$ are non-zero. Hence, the equation can be re-arranged as follows,

$$M_n \ddot{q}_n + C_n \dot{q}_n + K_n q_n = -L_n \ddot{u}_g \quad (6.4)$$

where $M_n = \underline{\phi}_n^T \underline{m} \underline{\phi}_n$ is the modal mass, $C_n = \underline{\phi}_n^T \underline{c} \underline{\phi}_n$ is the modal damping, $K_n = \underline{\phi}_n^T \underline{k} \underline{\phi}_n$ is the modal stiffness, and the term $L_n = \underline{\phi}_n^T \underline{m} \underline{l}$ on the right hand side is called the modal excitation factor. Dividing all terms by M_n leads to a final normalized form expressed in Equation 6.5.

$$\ddot{q}_n + 2\zeta_n \omega_n \dot{q}_n + \omega_n^2 q_n = -\frac{L_n}{M_n} \ddot{u}_g \quad (6.5)$$

Equation 6.5 is valid for all modes, $n = 1, 2, 3 \dots N$. This is equivalent to a SDOF system in modal coordinates q_n . Recalling the equation of motion for a SDOF system, Equation 6.6, and comparing with Equation 6.5, the only difference between them is the L_n/M_n term applied to the ground excitation in the modal equation of motion, Equation 6.5. Therefore, q_n can be expressed in terms of u as $q_n(t) = L_n/M_n u(t)$. This equality will be employed in the derivation of energy equations for MDOF systems.

$$\ddot{u} + 2\zeta\omega_n\dot{u} + \omega_n^2 u = -\ddot{u}_g \quad (6.6)$$

Energy equation for MDOF system is obtained by integrating the equation of motion given in Equation 6.4 over the modal displacement term q_n as shown in Equation 6.7. Definitions of the integral terms are the same for SDOF energy equation explained in Section 3.2. Since the modal displacement q_n is related to physical displacement u through $L_n/M_n u$, then dq_n in Equation 6.7 is also equal to $L_n/M_n du$. After replacing q_n and dq_n terms, the right hand side of the equation representing the modal total input energy becomes as given in Equation 6.8.

$$\int M_n \ddot{q}_n dq_n + \int C_n \dot{q}_n dq_n + \int K_n q_n dq_n = - \int L_n \ddot{u}_g dq_n \quad (6.7)$$

$$E_{I,n} = - \frac{L_n^2}{M_n} \int \ddot{u}_g du = - \frac{L_n^2}{M_n} \int \ddot{u}_g \dot{u} dt \quad (6.8)$$

Here, L_n^2/M_n represents the effective modal mass M_n^* . Thus, the n^{th} mode total input energy $E_{I,n}(T_n)$ can be obtained by multiplying M_n^* with the corresponding input energy spectral ordinate derived for a unit mass, $E_I(T_n)/m$. On the other hand, when the energy spectrum is expressed in terms of energy equivalent velocity V_{eq} (Equation 3.3), $E_{I,n}(T_n)$ can be obtained from Equation 6.9.

$$E_{I,n}(T_n) = \frac{1}{2} M_n^* V_{eq}^2(T_n) \quad (6.9)$$

Considering the combination of modal quantities, the total input energy for a MDOF system is equal to sum of the modal energies ($n=1, 2, 3, \dots, N$) as shown in Equation (6.10). For determining the minimum required number of modes in this equation, the procedure in the modal combination rule can be utilized where the sum of modal masses associated with the modes considered should be equal to at least 90% of the total mass of the system.

$$E_{I,tot} = \sum_{n=1}^N E_{I,n}(T_n) \quad (6.10)$$

6.2. Energy Dissipation at the Maximum Displacement Cycle

Input energy imparted to a structural system is dissipated by damping if the system remains in the linear elastic range during seismic response. Otherwise, it is dissipated simultaneously by viscous and hysteretic damping mechanisms in the inelastic range. The portion of total input energy dissipated by hysteretic damping through inelastic behavior during seismic response is a crucial information in energy-based design, because the amplitude and number of hysteretic cycles are directly related to damage in structural systems.

Figure 6.1 shows the response of an elastoplastic SDOF system under an earthquake ground excitation. The amount of energy dissipated by hysteretic cycles is calculated simply by integrating the area under the hysteresis curve with respect to deformation, where the remaining energy is dissipated by viscous damping. Hysteretic cycles, i.e. inelastic response history during seismic response display significant variability under different earthquake excitations, and it is not possible to predict this type of response accurately in the design stage. Instead, more predictable response parameters such as maximum inelastic displacement can be employed to predict hysteretic energy dissipation of the system.

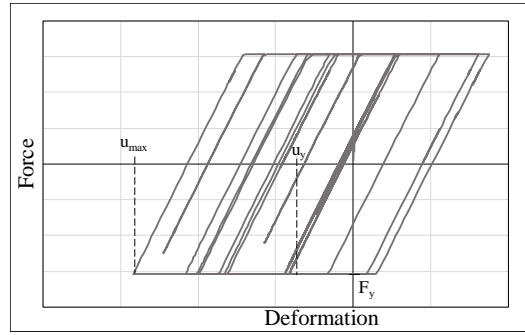


Figure 6.1. Force-deformation response of an elastoplastic SDOF system

In the previous chapter, two new approaches have been introduced in order to predict maximum inelastic displacements. Figure 6.1 shows a typical inelastic force (F) – deformation (u) response with u_y , u_{max} and F_y representing the main characteristics of an elasto-plastic system. Here F_y is the yield force, u_y is the yield displacement corresponding to F_y , and u_{max} is the maximum inelastic displacement under the ground excitation. The amount of energy dissipated at the maximum displacement cycle at u_{max} , which is denoted by E_0 , can be calculated by using the simple expression given in Equation 6.11. In this expression, the area enclosed by u_y and u_{max} is attained when the system reaches its maximum displacement during the maximum displacement cycle. E_0 can be predicted by linear elastic analysis if the maximum inelastic displacement can be predicted through the analysis of an equivalent linear system, as introduced in the previous chapter. The relation between E_0 and total input energy E_I can be employed for design purposes. The important point is to determine what portion of the total input energy, i.e. E_0 is dissipated at the maximum displacement cycle.

$$E_0 = F_y (u_{max} - u_y) \quad (6.11)$$

In this regard, the E_0/E_I ratio are computed in spectral form by employing the NF ground motion database mentioned in Chapter 4, for different R_μ values (2, 4 and 6) and 2% viscous damping. The E_0/E_I spectra obtained for each GM in the database and the corresponding mean and mean \pm standard deviations are presented in Figure 6.2

for three different R_μ values, respectively. It can be observed from the figures that mean curves are in the range of 0.2 to 0.3, and they display almost a constant variation independent of vibration period T . In order to observe the effects of R_μ more clearly, three mean spectral curves are plotted together and presented in Figure 6.3. It is clear that as R_μ increases from 2 to 6, spectral ratios reduce from 0.25 to 0.20 on average, and this difference is acceptably small. Thus, E_0/E_I ratio can be evaluated independent from R_μ for design purposes.

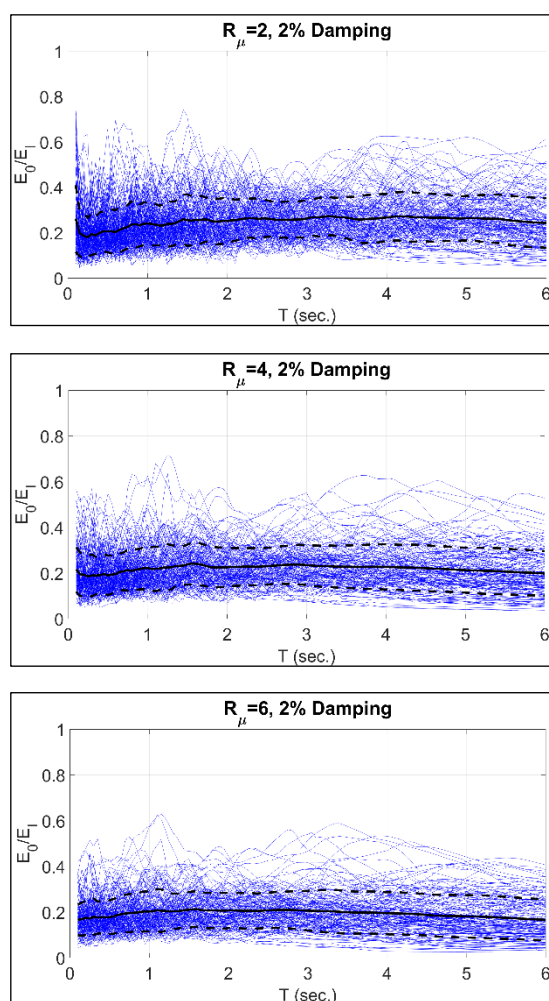


Figure 6.2. E_0/E_I spectra (2% damping) for three different R_μ values with the corresponding mean and mean \pm standard deviation curves: NF ground motions

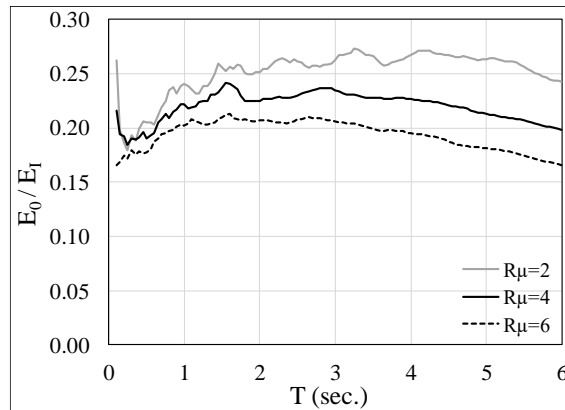


Figure 6.3. Comparison of mean E_0/E_I spectra (2% damping) obtained for three different R_μ values: NF ground motions

It was stated in Section 5.2 that damping efficiency shows strong dependency on M_w . Accordingly, the effect of M_w on E_0/E_I ratio is also investigated herein. The same four different M_w groups (M_w -1: 5.5-6.0, M_w -2: 6.0-6.5, M_w -3: 6.5-7.0, and M_w -4: >7.5), as expressed in Section 5.2.2, are employed for the investigation. Mean ratio spectra of the four M_w groups obtained for $R_\mu=4$ are shown in Figure 6.4. It can be seen from the figure that mean curves do not show any significant differences with respect to each other up to the period of 2 seconds. After $T=2$ sec., lower magnitude groups M_w -1 and M_w -2 give smaller values when compared to the other two means of M_w -3 and M_w -4, and show a decaying trend with period, unlike the higher M_w groups. In this period region, the differences between the mean curves get larger. Therefore, employing the E_0/E_I ratio for M_w -3 and M_w -4 in the long period range ($T > 2$ sec.) can be more conservative for seismic design.

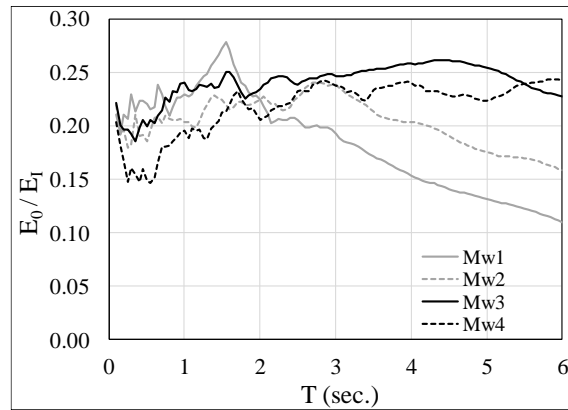


Figure 6.4. Comparison of mean E_0/E_I ratio spectra (2% damping) of four different M_w groups for $R_{\mu}=4$: NF ground motions

6.3. Energy-Based Seismic Assessment

The first step in the assessment procedure is the preliminary design of a structure by considering vertical service loads and reduced earthquake loads with respect to a seismic design code. Then eigenvalue analysis is conducted in order to obtain modal properties of the corresponding system. The next step is to calculate total input energy (E_I) for the MDOF system from input energy spectrum for unit mass, or in terms of equivalent velocity V_{eq} in order to employ the modal formulation derived in Section 6.1.

Prediction of deformation responses of the structural system is one of the most important step in this procedure. Due to its simplicity, response spectrum analysis (RSA) is preferred in the analysis. Response spectrum analysis is conducted by employing one of the equivalent linearization methods, including equal displacement rule with 5% viscous damping or with the equivalent damping spectra (modified equal displacement rule), or equivalent linearization with period shift introduced in Chapter 5. The important point in this step is to estimate the member-end deformations of the

inelastic (actual) system reasonably well in order to predict the energy dissipation mechanism accurately.

In the following stages of the procedure, energy dissipation responses of member-ends in terms of E_0 are evaluated to set a proper energy dissipation mechanism for the system. In the E_0 computations, moment (M) – rotation (θ) response of each member-end are taken into account. In this regard, the expression given in Equation 6.11 is modified for M and θ instead of F and u as in Equation 6.12 for calculating $E_{0,j}$ for the j^{th} member-end. The elasto-plastic moment (M) - rotation (θ) response is still employed herein as given in Figure 6.1. Hence,

$$E_{0,j} = M_{y,j} (\theta_{max,j} - \theta_{y,j}) \quad (6.12)$$

where $M_{y,j}$ is the yield moment capacity of the j^{th} member-end, $\theta_{y,j}$ is the associated yield rotation, and $\theta_{max,j}$ is the maximum rotation response obtained from RSA. It is noted that $M_{y,j}$ and $\theta_{y,j}$ are obtained from the preliminary design phase.

Then, the calculated $E_{0,j}$ values for each member-end are converted into the total energy that can be dissipated by the j^{th} member-end by using a scaling value. The scaling value is equal to the inverse of the ratio of E_0 to E_I , i.e. $(E_0/E_I)^{-1}$. After applying the scaling procedure, the energy dissipated by the j^{th} plastic hinge can be obtained from Equation 6.13.

$$E_j = E_{0,j} (E_0/E_I)^{-1} \quad (6.13)$$

The E_0/E_I spectra were obtained for the NF ground motion database in the previous section, and it was observed that E_0/E_I ratio is almost constant throughout the entire period region. This brings an important advantage for design calculations, since the E_0/E_I ratio is independent from T and R_μ when the mean spectrum of E_0/E_I is employed for design.

The E_j values can be calculated for the NP member ends which are expected to undergo plastic rotation during seismic response. The total plastic energy dissipated by the NP plastic hinges (E_{NP}) is simply calculated from Equation 6.14, where the summation of E_j 's give the total dissipated hysteretic energy. The remaining step is to determine the number and location of NP plastic hinges. NP is determined from the internal energy equilibrium given by Equation 6.15. That is, the energy dissipated by the NP number of plastic hinges should be equal to E_I .

$$E_{NP} = \sum_{j=1}^{NP} E_j \quad (6.14)$$

$$E_{NP} = E_I \quad (6.15)$$

The energy-based seismic assessment approach introduced herein suggests that the required number of plastic hinges and their locations, and the energy dissipation mechanism can be predicted reasonably well, by conducting response spectrum analysis (RSA) on the linear elastic model by using an equivalent linearization approach. Modified equal displacement rule implemented with the proposed damping spectra in the previous section is the preferred procedure here due to its simplicity and improved accuracy.

6.3.1. Verification of Energy-Based Seismic Assessment

The assessment procedure introduced previously is implemented on the 5-story frame which was also employed in the previous chapter. The design details were presented in Section 5.5. The procedure applied on the case study model can be summarized as follows:

1. Preliminary design: Capacity design with the design spectrum $PSa(T)$, reduced with an R_μ factor. Hence, overstrength is directly included. Internal end moments under design spectrum are the capacity moments $M_{y,j}$.

2. Obtain modal properties from eigenvalue analysis: T_n, ϕ_n ,
3. Employ input energy spectrum for unit mass, or equivalent velocity spectrum for the input energy of mode n : $E_{I,n} = M_n^* E_I(T_n)$, or $E_{I,n} = 1/2 M_n^* V_{eq}^2(T_n)$,
4. Compute total input energy from the MDOF formulation: $E_I = \sum E_{I,n}$,
5. Conduct response spectrum analysis (RSA) by using modified equal displacement rule (EDR) with equivalent damping spectra in order to obtain the member-end chord rotations $\theta_{max,j}$. Identify those *NP* hinges which exceed the associated yield rotation $\theta_{y,j}$.
6. For those yielding member-ends j : estimate $E_{0,j}$ from Equation 6.12,
7. Find the associated E_0/E_I spectral ratio for the 1st mode vibration period,
8. Calculate the energy dissipated by the j^{th} plastic hinge from Equation 6.13,
9. Computing the total energy dissipated by the *NP* plastic hinges as given in Equation 6.14,
10. Check the internal energy equilibrium stated in Equation 6.15.

In the following analyses, one ground motion record is selected from the batch of NF M_w -3 database defined in in Section 5.2.2. The ground motion labelled as GM46 was recorded during the M_w 6.69 Norridge-01 (1994) earthquake on site class *D* with the features of reverse faulting, 18 km fault rupture length (L_{rup}) and R_{epi} =4.85 km (R_{cst} =14.7 km). 5% damped elastic pseudo acceleration (PSa) spectrum of GM46 is shown in Figure 6.5(a). The main purpose of the verification is first the prediction of plastic hinge locations under GM46 by using RSA with modified EDR, and then comparing the actual plastic hinges under GM46 obtained from NRHA.

From the PSa spectrum of GM46, R_μ value is computed from Equation 5.5 as 3.2, and it is taken as 3 for brevity. Based on the findings in Chapter 4, elastic V_{eq} spectrum of

GM46 given in Figure 6.5(b) is utilized for E_I computation of the frame system. Modal properties of the first three modes and the corresponding modal energies are also presented in Table 6.1. The first three modes are taken into consideration, where the summation of the associated effective modal masses is equal to 96% of the total mass ($M_{tot} = 260.74$ tons).

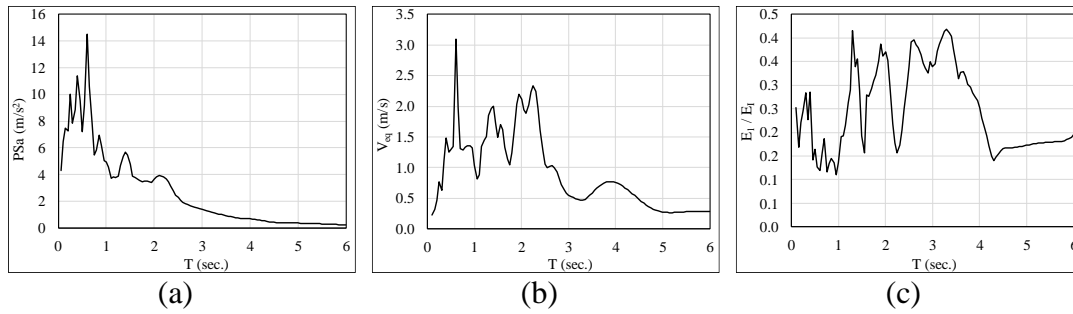


Figure 6.5. a) 5% damped PSA spectrum of GM46, b) Elastic equivalent velocity spectrum of GM46, c) E_0/E_I ratio spectrum of GM46 for $R_\mu=3$

Table 6.1. Modal properties and modal energies of the first three modes

Mode#	Periods (s)	M_n^* (tons)	$V_{eq}(T_n)$ (m/s)	$E_{I,n}$ (kJ)
1	0.94	208.11	1.37	194.74
2	0.28	28.96	0.66	6.37
3	0.15	12.25	0.31	0.60

Now, it is required to obtain maximum member-end rotations for calculating $E_{0,j}$. RSA is conducted considering the first three modes with equivalent damping spectrum of the modified equal displacement rule as explained in Section 5.3.1. Maximum responses from RSA is obtained from SRSS combination of the associated modal results. In calculating $E_{0,j}$ from Equation 6.12, $M_{y,j}$ and $\theta_{y,j}$ of the j^{th} member-end, such as column-end or beam-end, are obtained from the preliminary design as stated before. The obtained non-zero $E_{0,j}$ values are tabulated in Table 6.2 for beams and columns

separately, where a non-zero value indicates that the corresponding member ends exceed the elastic range ($\theta_{max,j} > \theta_{y,j}$). In the table given below, labels used for beams are composed of the letter *B* and three numbers expressing that the first number represents the story no, and the last number is used for the bay number from left to right, considering the elevation view of the frame shown in Figure 5.14(a). Similarly, the column labels are composed of the letter *C* and four numbers, where the first number is for the story number, and the last number is for the order from left to right in that story. I-end and J-end in the table means respectively the left end and the right end for beams, and bottom end and top end for columns. It is obvious from Table 6.2 that the first story column bottom ends dissipate the most energy, and then the beams ends follow the order of second story – first story – third story.

Table 6.2. Computed $E_{0,j}$ for member-ends j

Member Label	$E_{0,j}$ (kJ)	
	I-end	J-end
B111	1.22	0.91
B112	1.14	1.14
B113	0.91	1.22
B211	1.42	1.12
B212	1.34	1.34
B213	1.12	1.42
B311	1.07	0.81
B312	1.02	1.02
B313	0.81	1.07
B411	0.46	0.32
B412	0.52	0.52
B413	0.32	0.46
C1001	1.88	0.37
C1002	1.88	0.00
C1003	1.88	0.00
C1004	1.88	0.37

Then, the energy dissipated by the j^{th} plastic hinge (member-end) E_j is computed from Equation (6.13). The scaling factor is taken from E_0/E_I spectrum of GM46 shown in

Figure 6.5(c) for the first vibration period T_I . The corresponding value of $E_0/E_I(T_I)$ is equal to 0.118. By using the inverse of this ratio, E_j values of each plastic hinge are obtained for the given member-ends previously shown in Table 6.2. E_j values are presented in Table 6.3 in the descending order. These E_j values constitute E_{NP} for the next step. Finally, it is required to find out the required number of plastic hinges to satisfy the internal energy equilibrium stated in Equation 6.15. E_I is computed as equal to 201.70 kJ from the summation of $E_{I,n}$ values given in Table 6.1. Then, it is revealed from Table 6.3 that the first story column ends, and the total number of nine beam ends at the first and the second stories are adequate to dissipate E_I , where the energy dissipated by them (summation of E_j) is almost equal to 192 kJ.

Table 6.3. E_j values of plastic hinges at member-ends j

Member Label	E_j (kJ)	
	I-end	J-end
C1001	15.97	3.15
C1004	15.97	3.15
C1002	15.95	0.00
C1003	15.95	0.00
B211	12.05	9.49
B213	9.49	12.05
B212	11.32	11.32
B111	10.38	7.70
B113	7.70	10.38
B112	9.69	9.69
B311	9.03	6.88
B313	6.88	9.03
B312	8.61	8.61
B412	4.39	4.39
B411	3.92	2.70
B413	2.70	3.92

In order check the effectiveness of this proposed procedure, the determined plastic hinge locations is compared with those obtained from NRHA of the 5 story frame. The damping ratio is taken equal to 2% in the nonlinear model due to the reasons

mentioned in the previous chapter. In this sense, firstly maximum story displacements and story drift ratios from RSA and NRHA under GM46 are compared in order to check the prediction accuracy of RSA with modified equal displacement rule. The associated comparisons are shown in Figure 6.6. It can be observed that the obtained maximum story displacements and drifts obtained from RSA are very close to those obtained from NRHA. RSA with modified EDR gives 30% lower drift ratio at the first story than NRHA probably due to the formation of the first story mechanism during inelastic seismic response.

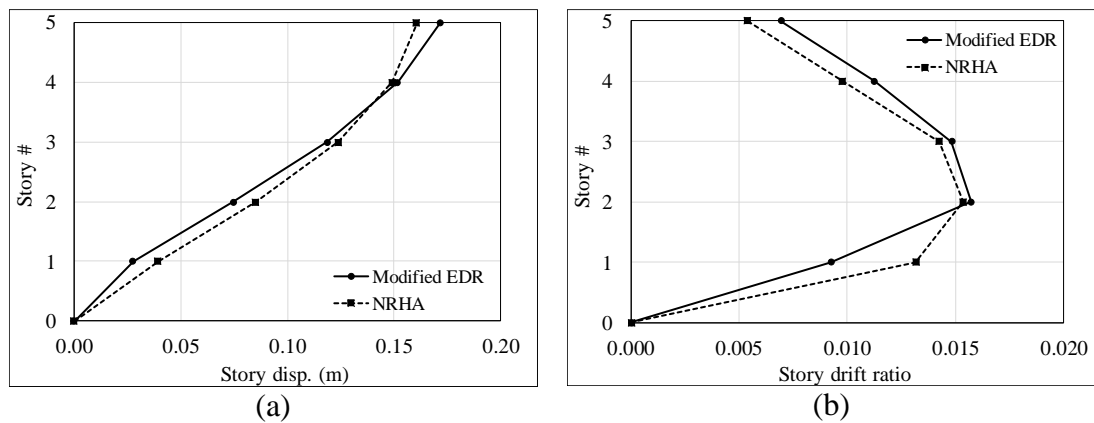


Figure 6.6. Original frame: a) Comparison of maximum story displacements from NRHA and RSA under GM46, b) Comparison of maximum story drifts from NRHA and RSA under GM46

Furthermore, the maximum chord rotations of column and beam ends obtained from RSA and NRHA are compared to verify the predicted plastic hinges. Figure 6.7 and Figure 6.8 show the maximum first story column-end rotations and the maximum beam-end rotations at the first, second and third story levels, respectively. In Figure 6.7, only first column end chord rotation demands are shown, since column end rotation at the upper stories are very low when compared to the first story results. Similarly, in Figure 6.8, only beam ends at the first three story levels are shown because beam end rotation demands decrease with story level, and so at the upper

floors the obtained rotations are so small. It is noted that the x-axis in these figures represent the coordinates of the member ends along the bay direction of the frame given in Figure 5.14(a). It is also seen from the figures that RSA with modified EDR predicts successfully the maximum end rotations from NRHA analysis. On the other hand, the maximum chord rotation locations in the system represent locations of maximum beam end plastic rotations, or plastic hinge locations. As stated before, in NRHA the maximum chord rotations are obtained at the first story column bottom ends, and beam ends in the first three stories. Besides, more demanding plastic rotations are computed at the first story column bottom ends, and at the beam ends in the first two story. These results are consistent with those obtained from the energy-based method. On the other hand, the third story beam ends give also plastic rotations, but they seem not so critical. This was also observed from Table 6.3, where E_j values of third story beam ends are lower than the energy values of beam ends at the first two stories. As a result, it is verified that energy-based assessment method can predict plastic hinge locations successfully, without conducting any nonlinear time history analysis.

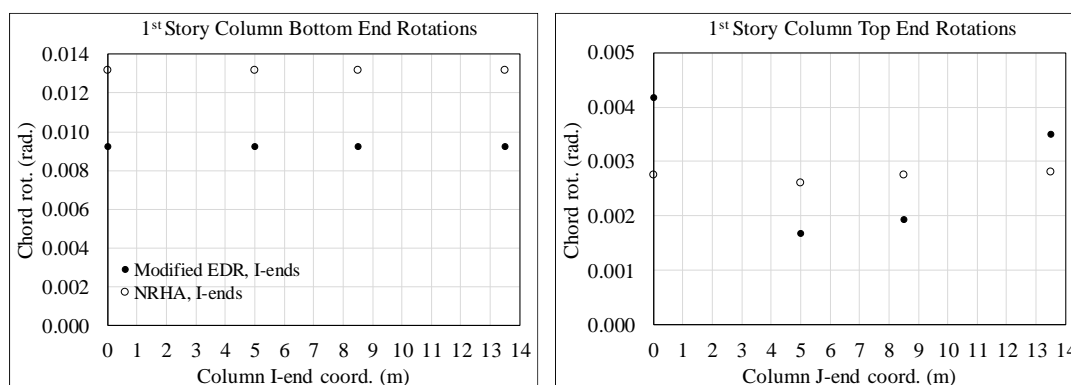


Figure 6.7. Comparison of maximum column end chord rotations from NRHA and RSA with modified EDR at the first story level

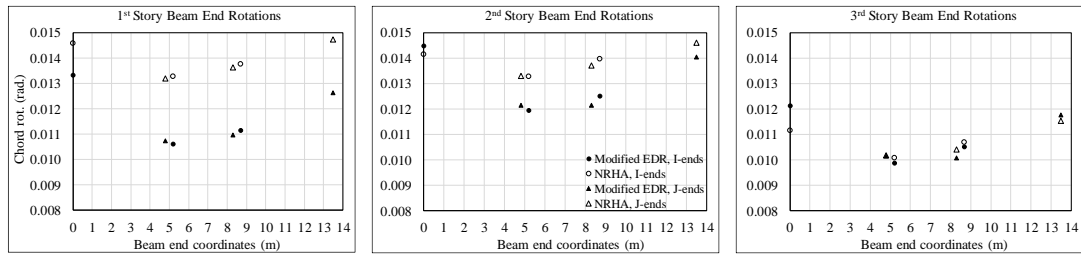


Figure 6.8. Comparison of maximum beam end chord rotations from NRHA and RSA with modified EDR at the first, second and third story levels, respectively

Energy-based approach gains a different perspective for predicting the seismic response of structural members. Based on the previous results, it can be seen that first story columns and the first two story beams could dissipate the seismic input energy imparted under GM46 record. Therefore, it can be examined that what if the actual response of the 5-story case study frame becomes, when the system can dissipate seismic energy at only the first column ends and beam ends in the first two stories. To test this approach, beams in the first two stories are weakened by reducing only the depth to 0.4 m. The section details remain as the same with the original section as shown in Figure 5.15(b). Thus, these beams are forced to dissipate more energy with increased deformations, and it is expected that the deformation levels of the beams at the upper stories remains almost in elastic limits.

The same procedure summarized above is employed for the modified frame. Modal properties and modal input energies ($E_{I,n}$) from energy spectrum of GM46 given in Figure 6.5(b) are shown in Table 6.4. Then, E_I is calculated as equal to 78.20 kJ from the summation of $E_{I,n}$. R_μ is calculated as 2.7 for this modified frame, and used as 3 in analyses. After calculating $E_{0,j}$ for each member end, E_j values are computed by multiplying the inverse of E_0/E_I ratio which is equal to 0.190 for T_1 from the spectrum given in Figure 5.15(c). The computed non-zero E_j values are shown in Table 6.5 in descending order. It can be investigated from the table that the first story columns and the beams at the second story can dissipate the entire energy imparted to the system

E_L . The total E_j corresponding to these member ends are equal to 99.00 kJ. Therefore, it can be stated that the modified frame system can dissipate the input energy efficiently by increasing deformation levels (reducing stiffnesses) only at the first two stories.

Table 6.4. Modal properties and modal energies of the first three modes of the modified frame

Mode#	Periods (s)	M_n^* (tons)	V_{eq} (T_n) (m/s)	$E_{L,n}$ (kJ)
1	1.07	211.82	0.83	72.27
2	0.29	24.67	0.64	5.11
3	0.15	12.74	0.35	0.80

Table 6.5. E_j values of plastic hinges at member-ends of the modified frame

Member Label	E_j (kJ)	
	I-end	J-end
C1001	10.72	4.76
C1004	10.72	4.76
C1002	10.71	2.43
C1003	10.71	2.43
B212	7.56	7.56
B211	7.05	6.26
B213	6.26	7.05
B112	6.49	6.49
B111	6.15	5.10
B113	5.10	6.15
B311	4.18	3.05
B313	3.05	4.18
B312	3.96	3.96
B412	1.60	1.60
B411	1.17	0.71
B413	0.71	1.17

Maximum responses obtained from NRHA of the modified frame are also calculated, and compared to those obtained from RSA with modified EDR to verify efficacy of the energy-based assessment procedure. Similar to the previous case, maximum story displacements and drifts, and maximum chord rotations of the critical columns and

beams are presented in Figure 6.9, Figure 6.10 and Figure 6.11 respectively. It is seen from Figure 6.9 that reducing beam sizes in the first two stories increase story displacements and drifts at these story levels. Furthermore, it can be seen from Figure 6.10 and Figure 6.11 that deformation levels at the bottom column-ends at the first story and beam-ends at the first two stories increase; however, chord rotation values are almost the same with the previous model presented in Figure 6.8. As expressed before, larger chord rotations imply plastic hinge locations with significant plastic deformations. Based on the implications from the figures below, the critical plastic deformations can be seen on the first story columns and beam ends at the first two stories like the initial assumption made for the modified frame.

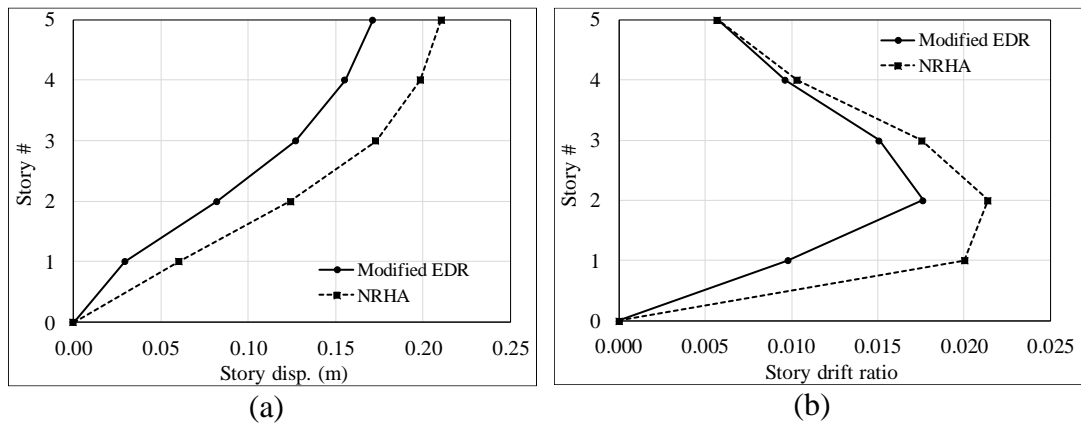


Figure 6.9. Modified frame: a) Comparison of maximum story displacement responses from NRHA and RSA under GM46, b) Comparison of maximum story drift responses from NRHA and RSA under GM46

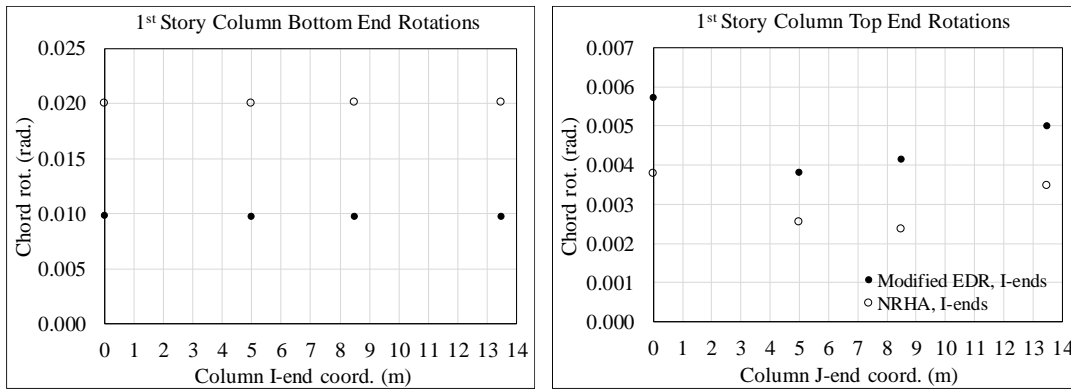


Figure 6.10. Comparison of maximum column end chord rotations from NRHA and RSA with modified EDR at the first story level of the modified frame

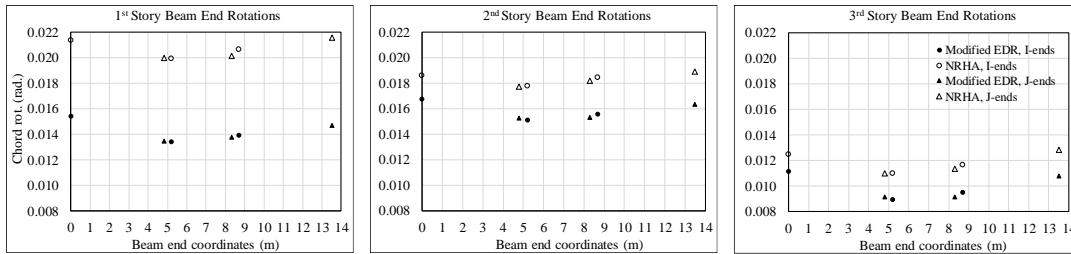


Figure 6.11. Comparison of maximum beam end chord rotations from NRHA and RSA with modified EDR at the first, second and third story levels, respectively

6.4. Energy-Based Seismic Design

The background study for energy-based seismic design is carried out, and presented herein. The main objective of the design procedure is to adopt seismic input energy as the input design parameter in order to obtain design forces for the earthquake load case. The new procedure is based on the computation of plastic rotation demands, and using them to determine energy-based design moments M_y under earthquake loads.

Before introducing the new seismic design procedure, it has to be noted that the preliminary sizing of the structural members is obtained by considering vertical service loads only. In the first step, maximum rotation demands at member ends $\theta_{max,j}$

are obtained from RSA with modified EDR without applying any vertical loads. Then, in order to compute the plastic rotation demands, it is required to calculate member-end yield rotations $\theta_{y,j}$. For this purpose, the well-known formula from the literature shown in Equation 6.16 is employed to calculate $\theta_{y,j}$ for structural members.

$$\theta_{y,j} = \frac{M_{d,j} l_c}{3EI} \left(1 - \frac{M_{d,i}}{2M_{d,j}} \right) \quad (6.16)$$

Here, $M_{d,j}$ is the preliminary design moment at the j^{th} end of the member, l_c is the clear span length of the corresponding member, E is the modulus of elasticity, and I is the moment of inertia of the member cross section. $M_{d,j}$ in the equation above is the design moment obtained from Equation 6.17.

$$M_{d,j} = \frac{M_{e,j}}{R_\mu} \quad (6.17)$$

In Equation 6.17, $M_{e,j}$ is calculated from RSA for the elastic case ($R_\mu=1$) considering only earthquake loads. Then, plastic rotations are determined for each joint j from the expression given in Equation 6.18. The computed values taken into account should be larger than zero for inelastic response.

$$\theta_{p,j} = (\theta_{max,j} - \theta_{y,j}), \text{ and } > 0 \quad (6.18)$$

The estimated plastic rotation amount of the j^{th} member-end can be used to predict the distribution of energy dissipation in the system. For the implementation of this concept, total E_0 of the system is obtained from the computed total input energy E_I and the E_0/E_I ratio spectrum, and then can be distributed to the j^{th} member end in the proportion of $\theta_{p,j}$. In this regard, the j^{th} end scale factor $r_{\theta,j}$ can be introduced, which is calculated by dividing the associated plastic rotation $\theta_{p,j}$ with the summation of all

plastic rotations at all member ends. The expression for this operation is presented in Equation 6.19.

$$r_{\theta,j} = \frac{\theta_{p,j}}{\sum \theta_{p,j}} \quad (6.19)$$

In the next step, as stated above, it is required to obtain the total E_0 ($E_{0,total}$) for the structural system. In this sense, the total input energy of the system E_I can be computed by employing the formulation given in Section 6.1, and then it can be converted to the total $E_{0,total}$ by utilizing E_0/E_I spectrum. The conversion operation for $E_{0,total}$ is shown in Equation 6.20.

$$E_{0,total} = \left(\frac{E_0}{E_I} \right) E_I \quad (6.20)$$

The rest of the procedure includes calculation of $E_{0,j}$ for each member end, and then computation of design moments $M_{y,j}$ for the earthquake loading case. As stated previously, $E_{0,j}$ for the j^{th} member end can easily be obtained by multiplying the associated scaling factor $r_{\theta,j}$ with $E_{0,total}$ as shown in Equation 6.21.

$$E_{0,j} = E_{0,total} \times r_{\theta,j} \quad (6.21)$$

Equation 6.12 given in Section 6.3 shows the calculation of $E_{0,j}$ from M_y , $\theta_{y,j}$, $\theta_{max,j}$. In this case, the unknown parameter for the j^{th} member end is $M_{y,j}$, and it can be computed by substituting Equation 6.12 into Equation 6.22. In the equation given below, $\theta_{p,j}$ is equal to $(\theta_{max,j} - \theta_{y,j})$ in the initial equation. Thus, design moments $M_{y,j}$ for each member end j can be obtained for design earthquake loading as given below.

$$M_{y,j} = \frac{E_{0,j}}{\theta_{p,j}} \quad (6.22)$$

Here, $E_{0,j}$ is obtained from Equation 6.21, in which $r_{\theta,j}$ is calculated from Equation 6.19. After substituting them into Equation 6.22, the equation becomes as given in Equation 6.23.

$$M_{y,j} = \frac{E_{0,total}}{\sum \theta_{p,j}} \quad (6.23)$$

6.4.1. Implementation of Energy-Based Seismic Design

The design approach developed in the previous section is implemented to the 5-story frame as in the assessment procedure verification. The design details of the frame were explained in Section 5.5. The design procedure implemented to the model is summarized step by step as follows:

1. Conduct preliminary sizing of structural members under vertical service loads only,
2. Obtain $\theta_{max,j}$ for each member end from RSA with modified EDR,
3. Calculating $\theta_{y,j}$ for each member end from Equation 6.16,
4. Determine non-zero $\theta_{p,j}$ from Equation 6.18 for the j^{th} member end,
5. Compute the scale (distribution) factor $r_{\theta,j}$,
6. Obtain $E_{0,total}$ from E_I of the system and E_0/E_I spectrum with respect to Equation 6.20,
7. Compute $E_{0,j}$ for the j^{th} member-end from $E_{0,total}$ and $r_{\theta,j}$ by using Equation 6.21,
8. Finally, obtain earthquake design moment $M_{y,j}$ from Equation 6.23 for the j^{th} member-end.

In the following analyses, two ground motion records are selected from the batch of NF M_w -3 (M_w 6.5- M_w 7.0) database defined in in Section 5.2.2. These ground motions are labelled as GM46, which was used also in the previous sections, and GM52. As

stated before, GM46 was recorded during M_w 6.69 Nortridge-01 (1994) earthquake on D site class with the features of reverse faulting, 18 km fault rupture length (L_{rup}) and R_{epi} =4.85 km (R_{clst} =14.7 km). GM52 was recorded during the M_w 6.69 Erzincan (1992) earthquake on D site class with the features of strike-slip faulting, 29 km fault rupture length (L_{rup}) and R_{epi} =8.97 km (R_{clst} =4.38 km). Elastic pseudo acceleration (PSa) spectra of GM46 and GM52 with 5% damping are presented in Figure 6.12(a).

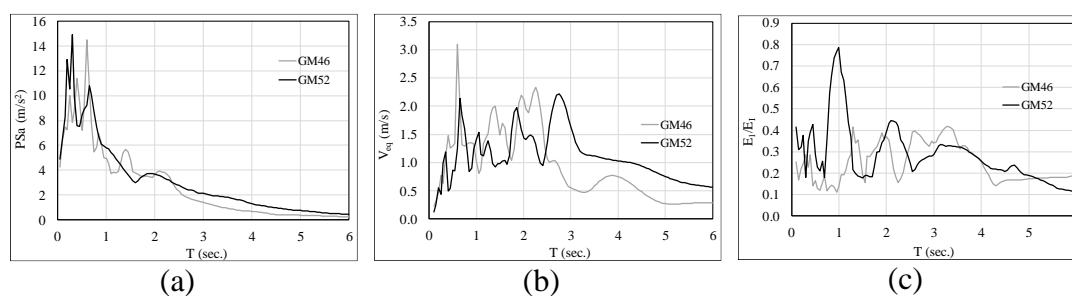


Figure 6.12. a) 5% damped PSa spectra of GM46 and GM52, b) Elastic equivalent velocity spectra of GM46 and GM52, c) E_0/E_1 ratio spectra of GM46 and GM52 for $R_\mu=3$

From the PSa spectra of GM46 and GM52, both R_μ values are computed from Equation 5.5 as 3.2 and 3.6, respectively. For RSA with modified EDR analyses, R_μ is taken as 3 for both records. Based on the findings in Chapter 4, elastic V_{eq} spectra of GM46 and GM52, given in Figure 6.12(b) are employed for input energy computation of the frame. Modal properties of the frame for the first three modes were also presented in Table 6.1. Due to the same reason stated in Section 6.3.1, the first three modes are taken in the SRSS combination for obtaining maximum responses from RSA with modified EDR.

From RSA with modified EDR, maximum rotation demands $\theta_{max,j}$ are obtained for each GM, and member end yield rotations $\theta_{y,j}$ are calculated, as the first step. Then, non-zero member end plastic rotations $\theta_{p,j}$ are determined from Equation 6.18, and presented in Table 6.6 and Table 6.7 below for GM46 and GM52, respectively. The

member labels in the tables given below represent the location at each story level along the bay axis of the frame shown in Figure 5.14(a). Zero values indicate no plastic action at the corresponding member-end. Now, distribution factors for member ends can be obtained simply from Equation 6.19 for each GM, separately.

Table 6.6. Plastic rotations $\theta_{p,j}$ of member ends from RSA under GM46

Member	Story 1 (rad.)		Story 2 (rad.)		Story 3 (rad.)		Story 4 (rad.)		Story 5 (rad.)	
	I-end	J-end	I-end	J-end	I-end	J-end	I-end	J-end	I-end	J-end
Left ext. beam	0.0091	0.0071	0.0100	0.0080	0.0084	0.0067	0.0056	0.0047	0.0034	0.0023
Interior beam	0.0076	0.0076	0.0084	0.0084	0.0070	0.0070	0.0047	0.0047	0.0023	0.0023
Right ext. beam	0.0071	0.0092	0.0081	0.0100	0.0067	0.0084	0.0047	0.0056	0.0023	0.0034
Left ext. column	0.0039	0.0000	0.0012	0.0000	0.0007	0.0000	0.0015	0.0000	0.0015	0.0000
Left int. column	0.0039	0.0000	0.0020	0.0000	0.0011	0.0000	0.0006	0.0000	0.0007	0.0000
Right int. column	0.0039	0.0000	0.0020	0.0000	0.0011	0.0000	0.0006	0.0000	0.0007	0.0000
Right ext. column	0.0039	0.0000	0.0012	0.0000	0.0007	0.0000	0.0015	0.0000	0.0015	0.0000

Table 6.7. Plastic rotations $\theta_{p,j}$ of member ends from RSA under GM52

Member	Story 1 (rad.)		Story 2 (rad.)		Story 3 (rad.)		Story 4 (rad.)		Story 5 (rad.)	
	I-end	J-end	I-end	J-end	I-end	J-end	I-end	J-end	I-end	J-end
Left ext. beam	0.0098	0.0075	0.0104	0.0084	0.0090	0.0072	0.0066	0.0054	0.0043	0.0029
Interior beam	0.0081	0.0081	0.0088	0.0088	0.0075	0.0075	0.0055	0.0055	0.0029	0.0029
Right ext. beam	0.0076	0.0098	0.0084	0.0104	0.0072	0.0090	0.0054	0.0066	0.0029	0.0043
Left ext. column	0.0042	0.0000	0.0015	0.0000	0.0017	0.0000	0.0016	0.0000	0.0015	0.0000
Left int. column	0.0042	0.0000	0.0021	0.0000	0.0016	0.0000	0.0012	0.0000	0.0007	0.0000
Right int. column	0.0042	0.0000	0.0021	0.0000	0.0016	0.0000	0.0012	0.0000	0.0007	0.0000
Right ext. column	0.0043	0.0000	0.0015	0.0000	0.0017	0.0000	0.0017	0.0000	0.0015	0.0000

Total input energies imparted to the frame are computed as 201.70 kJ and 157.36 kJ under GM46 and GM52, respectively. Then, E_0/E_I ratio is obtained by taking the mean of E_0/E_I ratios of the first three modes for each GM. Mean E_0/E_I ratios are calculated as 0.19 for GM46, and as 0.42 for GM52. Hence, from Equation 6.20, $E_{0,total}$ values can be calculated for the records. After scaling $E_{0,total}$ to member ends $E_{0,j}$ (Equation 6.21), earthquake design moments can be computed from Equation 6.23 for each GM. Equation 6.23 gives the same design moment M_y for all member ends, since design moments are equal to $E_{0,total} / \sum \theta_{p,j}$. The computed design moments are 171 kNm and 261 kNm for GM46 and GM52, respectively. From seismic response point of view, column base moment capacities can be assigned larger than the beam end moments to ensure stable behavior. Therefore, the obtained design moments M_y for GM46 and GM52 are raised to 250 kNm and 320 kNm, respectively. Earthquake design moments for member ends obtained from the energy-based procedure are shown in Table 6.8 for each GM record.

Table 6.8. Earthquake design moments obtained from energy-based procedure for GM46 and GM52

Member	GM46	GM52
	$M_{y,j}$ (kNm)	$M_{y,j}$ (kNm)
Beam	171	261
Column	250	320

Earthquake design moments are also obtained from force-based design in which maximum responses are obtained from RSA with modified EDR, considering the first three modes in SRSS combination. Beam end-moments and the first story column bottom end moments obtained from the RSA analyses under earthquake loads are shown in Figure 6.13 for the selected records separately. For single-type beam design and column design, force-based earthquake design moments are obtained by taking the maxima of beam moments and column moments, and presented in Table 6.9 for each GM.

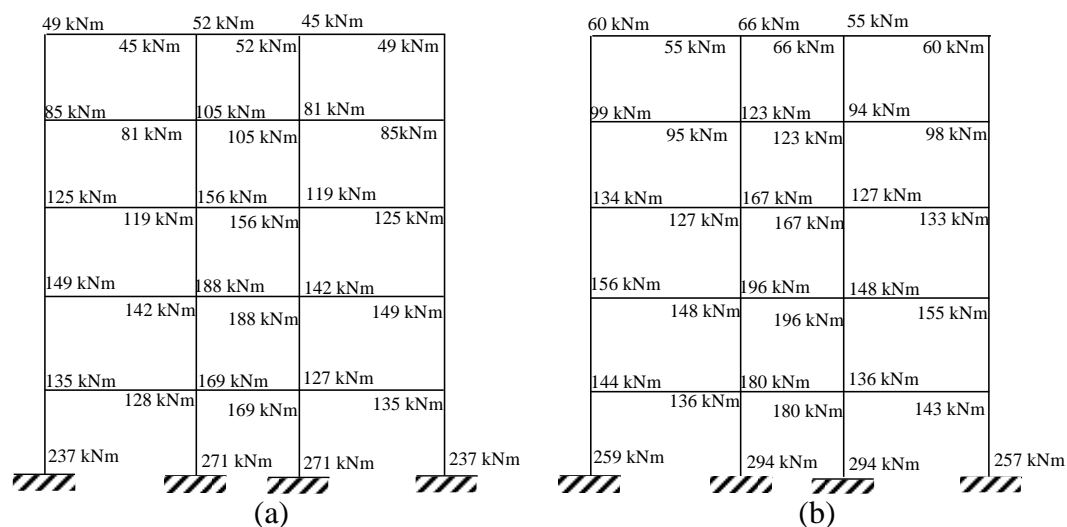


Figure 6.13. Member end moments from RSA w. modified EDR considering earthquake loads only from a) GM46, b) GM52

Table 6.9. Earthquake design moments obtained from force-based design for GM46 and GM52

Member	GM46	GM52
	$M_{y,j}$ (kNm)	$M_{y,j}$ (kNm)
Beam	188	196
Column	271	294

Although there is not much difference between earthquake design moments obtained from energy-based and force-based designs, force-based design gives 10% larger moments when compared to those from energy-based design for GM46. On the other hand, for GM52 energy-based design gives 30% larger design moments for beams, and 10% larger for columns compared to force-based design.

Seismic performance of the energy-based and force-based design are also compared. For this purpose, NRHA of the frames with two different design moments are conducted for each GM record. Figure 6.14 and Figure 6.15 show maximum story displacement and maximum story drift ratio comparisons for GM46 and GM52 respectively, including the associated RSA with modified EDR results. Although the

general responses of force-based and energy-based designed frames seem to be similar with each other, maximum story drifts for middle stories are 5% to 15% lower for the frame with energy-based design than the force-based designed frame.

The differences between maximum story drifts of the two design approaches have an effect on the maximum chord rotations. Figure 6.16 and Figure 6.17 show distributions of member-end plastic hinges throughout the frame systems obtained from NRHA of the two different designs for GM46 and GM52 records, respectively. It can be seen from Figure 6.16 for GM46 that there are more plastic hinges with considerable amount of plastic rotations in the first two story beams of the energy-base designed frame, when compared to the frame with force-based design. This is mainly due to the fact that maximum plastic rotations of the first story column ends with the force-based design are 10% larger than those in the energy-based results. This reduces rotation demands on the beams in the force-based designed frame. On the other hand, as can be seen from Figure 6.17 for GM52, energy-based design approach almost limits the plastic hinges into the first two stories and the first story column bottom ends. However, in force-based design, plastic hinges spread over the third story beams with considerable values of plastic rotations. In this case, maximum column bottom end plastic rotations are 3% larger in the energy-based designed frame than in the force-based design case. Eventually, increased member capacities in energy-based design for GM52 improves the seismic response of the frame system slightly.

The basic difference is in the design approach. In force-based design, member design forces are obtained from force-based linear elastic analysis, by employing response reduction factors. These factors are suggested heuristically in design codes, based on past experience. There is no theoretical basis in their calculation. Then seismic performance of the system comes indirectly where the designer has no direct control on seismic performance, or inelastic deformation distribution. On the other hand, calculation of member design forces are based on expected inelastic member

deformations, and their associated energy dissipation demands in the energy-based design. Response reduction factors are not considered. Linear elastic analysis is only employed for estimating inelastic deformations, but not for estimating internal forces. Equal displacement rule, or the improved version with damping spectra, is the only tool for relating linear elastic and inelastic dynamic response analysis.

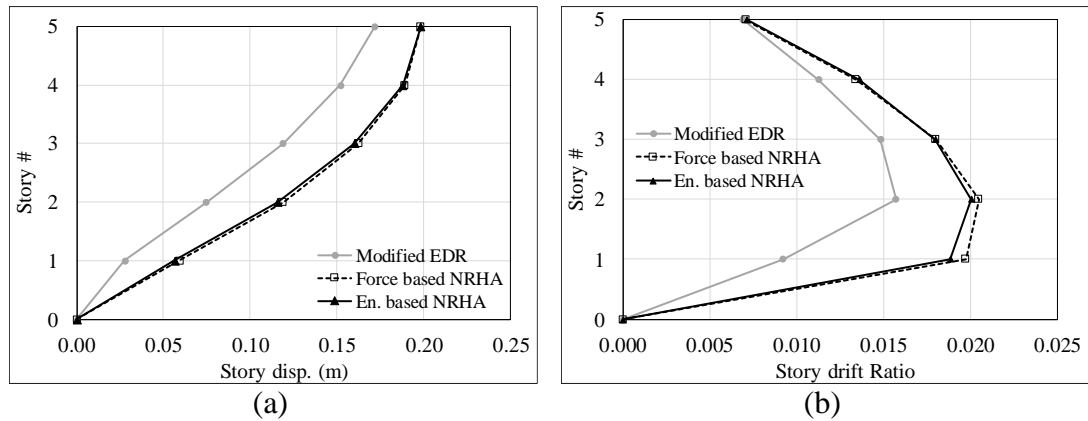


Figure 6.14. a) Comparison of maximum story displacements from NRHA of force-based design, NRHA of energy-based-based design and RSA with modified EDR under GM46, b) Comparison of maximum story drifts from NRHA of force-based design, NRHA of energy-based-based design and RSA with modified EDR under GM46

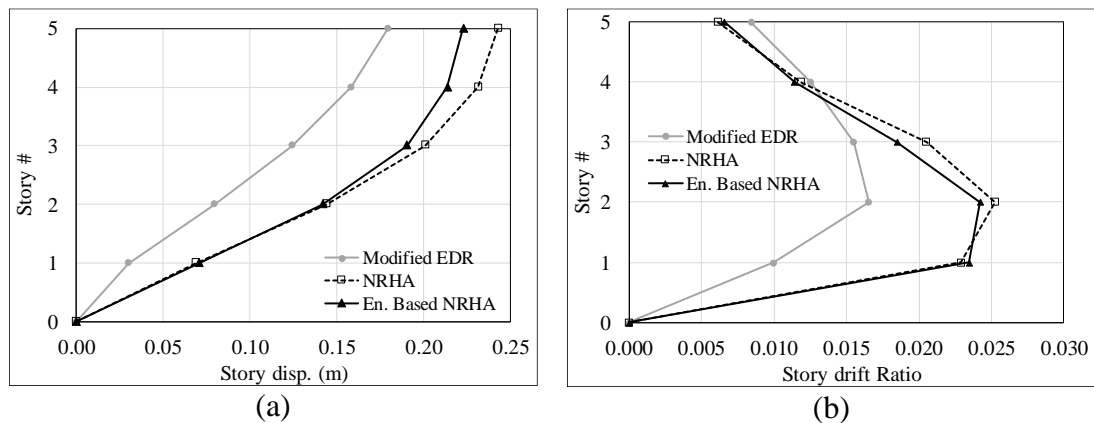


Figure 6.15. a) Comparison of maximum story displacements from NRHA of force-based design, NRHA of energy-based-based design and RSA with modified EDR under GM52, b) Comparison of maximum story drifts from NRHA of force-based design, NRHA of energy-based-based design and RSA with modified EDR under GM52

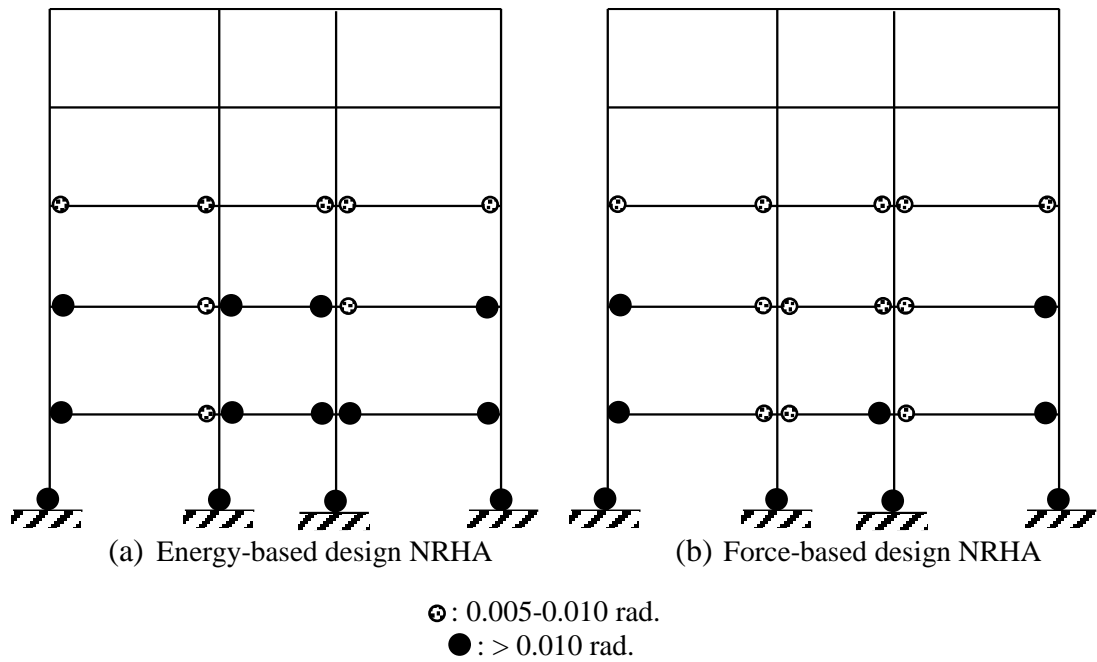


Figure 6.16. Plastic hinge distributions under GM46 record a) from NRHA of the frame with energy-based design, b) from NRHA of the frame with force-based design

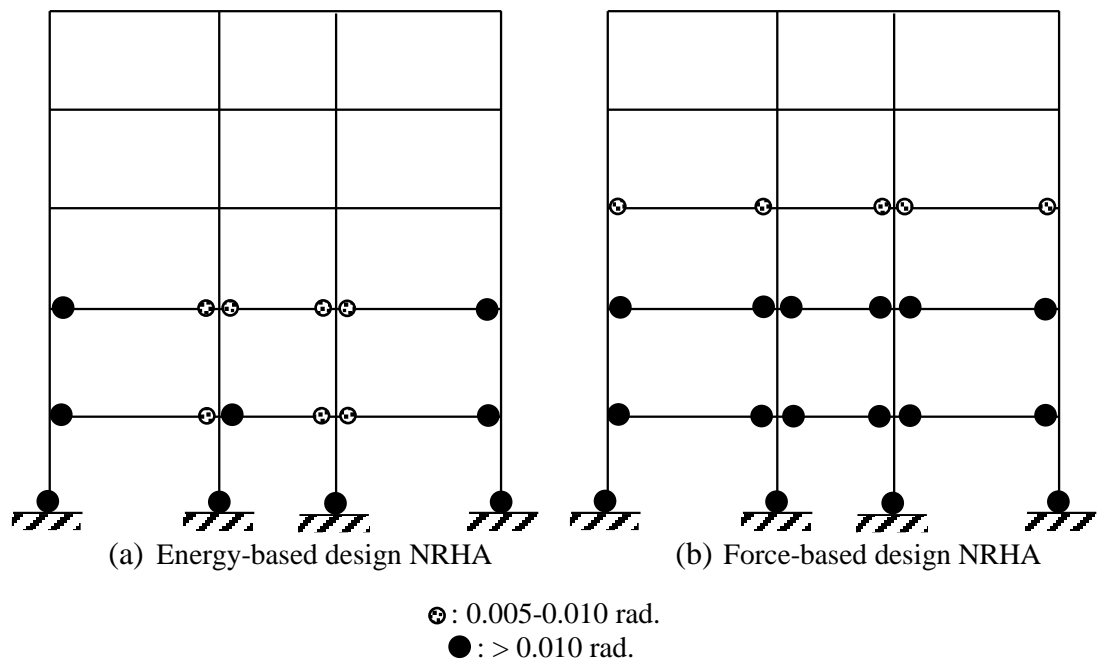


Figure 6.17. Plastic hinge distributions under GM52 record a) from NRHA of the frame with energy-based design, b) from NRHA of the frame with force-based design

CHAPTER 7

SUMMARY AND CONCLUSIONS

7.1. Summary

The purpose of this study is to develop energy-based seismic assessment and design procedures. The initial step in the energy-based approaches at a broader context is the prediction of total input energy imposed by ground shaking. A comprehensive study is presented in Chapter 3 on the prediction of input energy. In this sense, two approaches have been used. A prediction model has been developed through nonlinear regression analysis as the first approach considering M_w , R_{epi} , fault type and soil type as the basic seismological parameters. The second approach utilizes probabilistic seismic hazard maps. Input energy spectrum at a site can be directly obtained from the associated acceleration design spectrum by applying simple scaling relations developed in this study.

Then, prediction of input energy spectra has been extended to elastic and inelastic systems subjected to near-fault ground motions in Chapter 4. An inclusive evaluation of the effects of damping ratio ζ and lateral strength ratio R_μ on inelastic input energy spectra is presented. Significant observations were made about elastic and inelastic input energy spectra considering the effects of aforementioned parameters.

In the next chapter, the objective is to improve the maximum inelastic displacement predictions through linear elastic response analysis by introducing the R_μ - ζ - T spectra obtained from the modified equal displacement rule, or equivalent linearization with period shift, and to extend its implementation to MDOF systems. Due to the significant effect of damping on displacement response, a comprehensive investigation of

damping efficiency in reducing displacement response was conducted by considering ground motion related parameters including earthquake magnitude, distance to fault, fault type and soil type. Accordingly, the most effective parameters were identified.

Finally, in Chapter 6 the energy-based seismic assessment and design procedures are presented. In this context, input energy formulation for MDOF systems was derived and presented in detail. Then, the concept of energy dissipation at the maximum displacement cycle E_0 was introduced. Based on these concepts, the energy-based assessment procedure is developed and verified for a case study frame. Predicting the plastic hinge locations and rotations from an elastic model accurately brings significant practicality in evaluating the seismic performance of a structural system. Then a new energy-based design procedure is proposed, and implemented to a case study frame. The new procedure uses input energy as the input design parameter. This new method is based on the computation of plastic rotation demands, and using them to obtain the design moments for earthquake loads by employing the formulation of E_0 . These design moments are those which are required to achieve the plastic rotations, or the seismic performance estimated at the initial phase.

7.2. Conclusions

According to the results obtained in this study, the following conclusions are reached.

- Comparative result obtained by the prediction model in Chapter 3 revealed that earthquakes that occur on reverse and strike-slip faults impose larger energy demands than the earthquakes on normal faults. The effect of soil type on input energy is more significant for higher magnitude earthquakes, where ground motions on soft soil sites impose significantly larger energy demands compared with those on stiff sites. Input energy is generally largest at the short to medium period ranges under the ground motions from small to moderate magnitude earthquakes, whereas this period range includes long period structures under the ground motions from large magnitude earthquakes. The second approach

developed in Chapter 3 can be applied to an acceleration design spectrum obtained from seismic hazard maps by employing simple scaling relations only considering the effect of damping ratio. Based on the results from tests and verifications, input energy imposed on structures during strong earthquakes can be confidently obtained by using the models proposed in Chapter 3.

- Comparative results obtained in Chapter 4 revealed that near-fault ground motions have significantly larger energy dissipation demands, which are very sensitive to earthquake magnitude and soil type, and slightly sensitive to distance less than 15 km, but not sensitive to distances longer than 15 km.
- Based on further results obtained from Chapter 4, the effect of damping on input energy spectra for elastic and inelastic systems is found negligible. Near-fault input energy spectra for inelastic system has some dependency on R_μ for short period systems; however, there is no dependency on R_μ for intermediate and long period systems. Accordingly, elastic input energy spectra obtained for a reference 5% damped system can be practically used to predict the inelastic input energy spectra for intermediate and long period systems for all damping ratios with slight conservatism. This result recalls an equal energy rule, which can be considered as a significant advantage for an energy-based design approach. Therefore, the proposed prediction equation in Chapter 4 can be consistently employed for predicting the mean elastic and inelastic input energy spectra from near-fault earthquake source with a given magnitude, fault type, soil type at the site, and source to site distance.
- Comparative results obtained in Chapter 5 show that damping has a significant effect on the prediction of the maximum inelastic displacements through linear elastic response analysis. According to the investigation of the influence of earthquake magnitude, fault distance, soil type and fault type on damping efficiency, earthquake magnitude is evaluated as the most effective parameter for damping efficiency. It is observed that the proposed $R_\mu-\xi-T$ spectra improves the

displacement predictions of equivalent linear systems reasonably well. On the other hand, assuming 5% damping for equivalent linear systems in the implementation of equal displacement rule coincidentally gives correct damping values for several cases.

- Based on the findings from the energy-based assessment procedure developed in Chapter 6, the new assessment method predicts the required number of plastic hinges and locations, and the energy dissipation mechanism properly under a defined ground excitation by employing only RSA with the modified EDR. Therefore, application of the procedure brings practicality for seismic assessment by using only a linear elastic model instead of conducting nonlinear dynamic analysis. Moreover, seismic performance of a structural system can be evaluated quite accurately from the energy dissipation performance point of view.
- The energy-based design method developed in Chapter 6 is based mainly on adopting seismic input energy as the main design parameter to obtain earthquake design forces. Using input energy as a design parameter facilitates consideration of the effect of loading history. Furthermore, energy-based design relates maximum deformation response more efficiently to earthquake design forces by employing the formulation of E_0 developed in this study. Although the results from the implementation of the procedure on the case study are GM dependent, it can be stated that energy-based design method provides a solid relation between the intended inelastic deformations and design forces. Limiting plastic deformations by increasing member capacities or increasing the energy dissipation effectiveness of member ends by providing uniform plastic hinge distribution are the main contributions of this method. However, some points such as column design need more research, and extensive sensitivity analyses are required for establishing a robust energy-based seismic design methodology.

REFERENCES

- Acun, B. and Sucuoğlu, H. 2010. Performance of reinforced concrete columns designed for flexure under severe displacement cycles. *ACI Structural Journal*, 107(3), 364–371.
- Akiyama, H. 1985. *Earthquake Resistant Limit-State Design for Buildings*. University of Tokyo Press: Japan.
- Akiyama, H. 1988. *Earthquake Resistant Design Based On the Energy Concept*. Proceeding of the 9th World Conference on Earthquake Engineering, IAEE: Tokyo, Japan, 5, 905–910.
- Akkar, S. and Bommer, J. 2007a. Empirical prediction equations for peak ground velocity derived from strong-motion records from Europe and middle east. *Bulletin of Seismological Society of America*, 97(2), 511–530.
- Akkar, S. and Bommer, J. 2007b. Prediction of elastic displacement response spectra in Europe and the middle east. *Earthquake Engineering and Structural Dynamics*, 36, 1275–1301.
- Akkar, S. and Bommer, J. 2010. Empirical equations for the prediction of PGA, PGV and spectral accelerations in Europe the Mediterranean region, and the middle east. *Seismological Research Letters*, 81(2), 195–206.
- Alavi, B. and Krawinkler, H. 2004. Behavior of moment-resisting frame structures subjected to near-fault ground motions. *Earthquake Engineering and Structural Dynamics* 33, 687–706.
- Alıcı, F.S. and Sucuoğlu, H. 2016. Prediction of input energy spectrum: attenuation models and velocity spectrum scaling. *Earthquake Engineering and Structural Dynamics* 45, 2137–2161.
- Ambraseys, N.N. and Douglas, J. 2003. Near-field horizontal and vertical earthquake ground motions. *Soil Dynamics and Earthquake Engineering* 23, 1–18.
- Amiri, G.G., Darzi, G.A. and Amiri, J.V. 2008. Design elastic input energy spectra based on Iranian earthquakes. *Canadian Journal of Civil Engineering*, 35, 635–646.
- ASCE. 2010. *Minimum design loads for buildings and other structures*. ASCE/SEI Standart 7-10.
- Baker, W.B. 2007. Quantitative classification of near-fault ground motions using wavelet analysis. *Bulletin of Seismological Society of America* 97(5), 1486–1501.

- Benavent-Climent, A. 2007. An energy-based damage model for seismic response of steel structures. *Earthquake Engineering and Structural Dynamics* 36, 1049–1064.
- Benavent-Climent, A., Lopez-Almansa, F. and Bravo-Gonzales, D.A. 2010. Design energy input spectra for moderate-to-high seismicity regions based on Colombian earthquakes. *Soil Dynamics and Earthquake Engineering*, 30, 1129–1148.
- Benavent-Climent, A., Pujades, L.G. and Lopez-Almansa, F. 2002. Design energy input spectra for moderate seismicity regions. *Earthquake Engineering and Structural Dynamics*, 31, 1151–1172.
- Boore, D.M., Joyner, W.B. and Fumal, T.E. 1993. Estimation of response spectra and peak acceleration from western north American earthquakes. U.S. Geological Survey, Menlo Park: Open File Report No 93-509.
- Boore, D.M., Joyner, W.B. and Fumal, T.E. 1997. Equations for estimating horizontal response spectra and peak acceleration from western north American earthquakes: a summary of recent work. *Seismological Research Letters*, 68(1), 128–153.
- Bozorgnia, Y., Hachem, M.M. and Campbell, W. 2010. Deterministic and probabilistic predictions of yield strength and inelastic displacement spectra. *Earthquake Spectra* 26(1), 25–40.
- Bray, J.D. and Rodriguez-Marek, A., 2004. Characterization of forward-directivity ground motions in the near-fault region. *Soil Dynamics and Earthquake Engineering* 24, 815–828.
- Bruneau, M. and Wang, N. 1996. Normalized energy-based methods to predict the seismic ductile response of SDOF structures. *Engineering Structures*, 18(1), 13–28.
- CEN. Eurocode 8, Design Structures for Earthquake Resistance, European Prestandard ENV 1998-1: 2004. Comité Européen de Normalisation: Brussels, 1994.
- Chapman, M.C. 1999. On the use of elastic input energy for seismic hazard analysis. *Earthquake Spectra*, 15(4), 607–635.
- Cheng, Y., Lucchini, A. and Mollaioli, F. 2014. Proposal of new ground-motion prediction equations for elastic input energy spectra. *Earthquakes and Structures*, 7(4), 485–510.

- Chioccarelli, E. and Iervolino, I. 2010. Near-source seismic demand and pulse-like records: A discussion for L'Aquila earthquake. *Earthquake Engineering and Structural Dynamics* 39, 1039–1062.
- Chioccarelli, E. and Iervolino, I. 2013. Near-source seismic hazard and design scenarios. *Earthquake Engineering and Structural Dynamics* 42, 603–622.
- Chopra, A.K. and Chintanapakdee, C. 2001. Comparing response of SDOF systems to near-fault and far-fault earthquake motions in the context of spectral regions. *Earthquake Engineering and Structural Dynamics* 30, 1769–1789.
- Chopra, A.K. and Chintanapakdee, C. 2004. Inelastic deformation ratios for design and evaluation of structures: single degree of freedom bilinear systems. *ASCE Journal of Structural Engineering*, 130, 1309–1319.
- Chou, C.C. and Uang, C.M. 2000. Establishing absorbed energy spectra – an attenuation approach. *Earthquake Engineering and Structural Dynamics*, 29, 1441–1455.
- Chou, C.C. and Uang, C.M. 2003. A procedure for evaluating seismic energy demand of framed structures. *Earthquake Engineering and Structural Dynamics*, 32, 229–244.
- Decanini, L.D. and Mollaioli, F. 1998. Formulation of elastic earthquake input energy spectra. *Earthquake Engineering and Structural Dynamics*, 27, 1503–1522.
- Decanini, L.D. and Mollaioli, F. 2001. An energy-based methodology for the assessment of seismic demand. *Soil Dynamics and Earthquake Engineering*, 21(2), 113–137.
- Erberik, M.A. and Sucuoğlu, H. 2004. Seismic energy dissipation in deteriorating systems through low-cycle fatigue. *Earthquake Engineering and Structural Dynamics*, 33(1), 49–67.
- Fajfar, P. and Fischinger, M. 1990. A Seismic Design Procedure Including Energy Concept. *Proceedings of the 9th European Conference on Earthquake Engineering*, Moscow, Russia, September, 2, 312–321.
- Fajfar, P. and Vidic, T. 1994. Consistent inelastic design spectra: hysteretic and input energy. *Earthquake Engineering and Structural Dynamics*, 23, 523–537.
- Fajfar, P. and Vidic, T. 1994. Consistent inelastic design spectra: strength and displacement. *Earthquake Engineering and Structural Dynamics*, 23, 507–521.
- Fajfar, P., Vidic, T. and Fischinger, M. 1989. Seismic demand in medium- and long-period structures. *Earthquake Engineering and Structural Dynamics*, 18, 1133–1144.

- Fajfar, P., Vidic, T., and Fischinger, M. 1992. On Energy Demand and Supply in SDOF Systems. *Nonlinear Seismic Analysis of Reinforced Concrete Buildings*: Elsevier, London, 48–71 p.
- FEMA. Improvement of Nonlinear Static Seismic Procedures (FEMA 440). ATC-55: Washington, DC, 2005.
- FEMA. NEHRP Recommended Seismic Provisions for New Buildings and Other Structures (FEMA P-1050-1/2015). Building Seismic Safety Council. FEMA: Washington DC, 2015.
- Gülkan, P. and Sozen, M. 1974. Inelastic response of reinforced concrete structures to earthquake motions. *ACI Journal* 71, 604–610.
- Housner, G.W. 1956. Limit Design of Structures to Resist Earthquakes. *Proceedings of the 1st World Conference on Earthquake Engineering*, IAEE: Berkeley, California, 186–198.
- Housner, G.W. 1959. Behavior of structures during earthquake. *Journal of the Engineering Mechanics Division*, 85, 109–129.
- Housner, G.W. 1965. Intensity of earthquake ground shaking near the causative fault. *Proceedings, 3rd World Conference on Earthquake Engineering*, Auckland, New Zealand.
- Hudson, D.E. 1956. Response spectrum techniques in engineering seismology. *Proceedings of the 1st World Conference on Earthquake Engineering*, IAEE: Berkeley, California, 4, 1–12.
- Iervolino, I. and Cornell, C.A. 2008. Conditional pulse probability for near-source hazard analysis. *14th World Conference on Earthquake Engineering*, Beijing, China.
- Iervolino, I., Chioccarelli, E. and Baltzopoulos, G. 2012. Inelastic displacement ratio of near-source pulse-like ground motions. *Earthquake Engineering and Structural Dynamics* 41, 2351–2357.
- Iwan, W.D. and Gates, N.C. 1979. The effective period and damping of a class of hysteretic structures. *Earthquake Engineering and Structural Dynamics*, 7, 199-211.
- Jacobsen, L. S. 1930. Steady forced vibrations as influenced by damping. *ASME Trans.* 52(1), 169–81.
- Jacobsen, L.S. 1960. Damping in composite structures. *Proceedings of 2nd World Conference on Earthquake Engineering*, 2, 1029–1044.

- Jennings, P. 1968. Equivalent damping for yielding structures. *Journal of Engineering Mechanics Division ASCE* 94, 103–116. 13.
- Kalkan, E. and Kunnath, K. 2006. Effects of fling step and forward directivity on seismic response of buildings. *Earthquake Spectra* 22(2), 367–390.
- Kowalsky, M.J. 1994. Displacement-based design-a methodology for seismic design applied to RC bridge columns. Master's Thesis, University of California at San Diego, La Jolla, California.
- Kuwamura, H., Kirino, Y. and Akiyama, H. 1994. Prediction of earthquake energy input from smoothed Fourier amplitude spectrum. *Earthquake Engineering and Structural Dynamics*, 23, 1125–1137.
- Liossatos, E. and Fardis, M.N. 2016. Near-fault effects on residual displacement of RC structures. *Earthquake Engineering and Structural Dynamics* 45, 1391–1409.
- Manfredi, G. 2001. Evaluation of seismic energy demand. *Earthquake Engineering and Structural Dynamics*, 30, 485–499.
- Mavroeidis, G.P., Dong, G. and Papageorgiou, A.S. 2004. Near-fault ground motions, and the response of elastic and inelastic single-degree-of-freedom (SDOF) systems. *Earthquake Engineering and Structural Dynamics* 33, 1023–1049.
- McKevitt, W.E., Anderson, D.L. and Cherry, S. 1960. Hysteretic Energy Spectra in Seismic Design. *Proceedings of the 2nd World Conference on Earthquake Engineering*, IAEE: Tokyo and Kyoto, Japan, 7: 487–494.
- Miranda, E. 2000. Inelastic displacement ratios for structures on firm sites. *Journal of Structural Engineering* 126, 1150–1159.
- Miranda, E., and Ruiz-Garcia, J. 2002. Evaluation of approximate methods to estimate maximum inelastic displacement demands. *Earthquake Engineering and Structural Dynamics*, 31, 539–560.
- Mollaioli, F., Bruno, S., Decanini, L.D. and Panza, G.F. 2006. Characterization of the dynamic response of structures to damaging pulse-type near-fault ground motions. *Meccanica* 41, 23–46.
- Newmark, N.M. and Hall, W.J. 1982. *Earthquake Spectra and Design*. Earthquake Engineering Research Institute, Berkeley, CA.
- Nurtuğ, A. and Sucuoğlu, H. 1995. Prediction of seismic energy dissipation in SDOF systems. *Earthquake Engineering and Structural Dynamics*, 24, 1215–1223.

- Okur, A. and Erberik, M.A. 2012. Adaptation of Energy Principles in Seismic Design of Turkish RC Frame Structures Part I: Input Energy Spectrum. Proceedings of the 15th World Conference on Earthquake Engineering, IAEE: Lisbon, Portugal.
- Ordaz, M., Huerta, B. and Reinoso, E. 2003. Exact computation of input-energy spectra from Fourier amplitude spectra. *Earthquake Engineering and Structural Dynamics*, 32, 597–602.
- Quaranta, G. and Mollaioli, F. 2018. On the use of the equivalent linearization for bilinear oscillators under pulse-like ground motions. *Engineering Structures* 160, 395–407.
- Quinde, P., Reinoso, E. and Terán-Gilmore A. 2016. Inelastic seismic energy spectra for soft soils: Application to Mexico City. *Soil Dynamics and Earthquake Engineering* 89, 198–2017.
- Rosenblueth, E. and Herrera, I. 1964. On a kind of hysteretic damping. *Journal of Engineering Mechanics Division ASCE* 90, 37–48.
- Ruiz-García, J. 2011. Inelastic displacement ratios for seismic assessment of structures subjected to forward-directivity near-fault ground motions. *Journal of Earthquake Engineering* 15, 449–468.
- Shahi, S.K. and Baker, J.W. 2011. An empirically calibrated framework for including the effects of near-fault directivity in probabilistic seismic hazard analysis. *Bulletin of the Seismological Society of America* 101(2), 742–755.
- Shibata, A. and Sozen, M. 1976. Substitute structure method for seismic design in RC. *Journal of Structural Division ASCE*, 102, 1–18.
- Somerville, P.G., Smith, N.F. and Graves, R.W. 1997. Modification of empirical strong ground motion attenuation relations to include the amplitude and duration effects of rupture directivity. *Seismological Research Letters* 68(1), 199–222.
- Soong, T.T. and Spencer, Jr.B.F. 2002. Supplemental energy dissipation: State-of-the-art and state-of-the-practice. *Engineering Structures* 24(3), 243–259.
- Sucuoğlu, H. and Nurtuğ, A. 1995. Earthquake ground motion characteristics and seismic energy dissipation. *Earthquake Engineering and Structural Dynamics*, 24, 1195–1213.
- Symans, M.D., Charney, F.A., Whittaker, A.S., Constantinou, M.C., Kircher, C.A., Johnson, M.W. and McNamara, R.J. 2008. Energy Dissipation Systems for Seismic Applications: Current Practice and Recent Developments. *Journal of Structural Engineering*, 134(1), 3-21.

- TBI. 2017. Guidelines for performance-based design of tall buildings. Pacific Earthquake Engineering Center, Report No. 2017/06, version 2.03.
- Tothong, P. and Cornell, C.A. 2006. An empirical ground-motion attenuation relation for inelastic spectral displacement. *Bulletin of Seismological Society of America* 96(6), 2146–2164.
- Tothong, P., Cornell, C.A. and Baker, J.W. 2007. Explicit directivity-pulse inclusion in probabilistic seismic hazard analysis. *Earthquake Spectra* 23(4), 867–891.
- Uang, C.M. and Bertero, V.V. 1988. Implications of recorded earthquake ground motions on seismic design of building structures. Earthquake Engineering Research Center, University of California, Berkeley, Report No. UCB/EERC-88/13.
- Uang, C.M. and Bertero, V.V. 1990. Evaluation of seismic energy in structures. *Earthquake Engineering and Structural Dynamics*, 19, 77–90.
- Veletsos, A.S. and Newmark, N.M. 1960. Effect of inelastic behavior on the response of simple systems to earthquake motions. *Proceedings of 2nd World Conference on Earthquake Engineering*, 2, 895–912.
- Vidic, T., Fajfar, P. and Fischinger, M. 1994. Consistent inelastic design spectra: strength and displacement. *Earthquake Engineering and Structural Dynamics* 23, 507–521.
- Wang, G.-Q., Zhou, X.-Y., Zhang, P.-Z. and Igel, H. 2002. Characteristics of amplitude and duration for near fault strong ground motion from the 1999 Chi-Chi, Taiwan Earthquake. *Soil Dynamics and Earthquake Engineering* 22, 73–96.
- Zahrah, T.F. and Hall, W.J. 1984. Earthquake energy absorption in SDOF structures. *Journal of Structural Engineering*, 110(8), 1757–1772.
- Zhang, S. and Wang, G. 2013. Effects of near-fault and far-fault ground motions on nonlinear dynamic response and seismic damage of concrete gravity dams. *Soil Dynamics and Earthquake Engineering* 53, 217-229.

CURRICULUM VITAE

PERSONAL INFORMATION

Surname, Name : Alici, Firat Soner
Nationality : Turkish (TC)
Date and Place of Birth : 19 March 1987, Ankara
Marital Status : Married
Phone : +90 535 615 60 18
E-mail : fsonalici@gmail.com

EDUCATION

Degree	Institution	Year of Graduation
MS	METU, Civil Engineering	2012
BS	METU, Civil Engineering	2009
High School	Anittepe High School, Ankara	2004

WORK EXPERIENCE

Year	Place	Enrollment
2014-2018	METU, Department of Civil Engineering	Research Assistant
2013-2014	İller Bank Inc., Ankara	Assistant Technical Expert
2009-2013	METU, Department of Civil Engineering	Research Assistant

FOREIGN LANGUAGES

Advanced English

PUBLICATIONS

Journals

Alıcı F.S., Sucuoğlu H. “Elastic and Inelastic Near-Fault Input Energy Spectra”, *Earthquake Spectra*, 34(2), 611-637 (2018).

Alıcı F.S., Sucuoğlu H. “Prediction of Input Energy Spectrum: Attenuation Models and Velocity Spectrum Scaling”, *Earthquake Engineering and Structural Dynamics*, 45, 2137-2161 (2016).

Alıcı F.S., Sucuoğlu H. “Practical Implementation of Generalized Force Vectors for the Multimodal Pushover Analysis of Building Structures”, *Earthquake Spectra*, 31(2), 1043-1067 (2015).

Conference Proceedings

Alıcı F.S., Sucuoğlu H. “Prediction of input energy spectrum: prediction models and velocity spectrum scaling”, 16th European Conference on Earthquake Engineering, Thessaloniki, Greece, 2018.

Alıcı F.S., Sucuoğlu H. “Prediction of input energy spectrum: attenuation models and velocity spectrum scaling”, 4th International Earthquake Engineering and Seismology Conference, Eskişehir, Turkey, 2017.

Alıcı F.S., Sucuoğlu H. “Prediction of input energy spectrum: attenuation models and velocity spectrum scaling”, 16th World Conference on Earthquake Engineering, Santiago, Chile, January 2017.

Kaatsız K., Alıcı F.S., and Sucuoğlu H. “Generalized Pushover Analysis for Torsionally Coupled Systems”. 16th World Conference on Earthquake Engineering, Santiago, Chile, January 2017.

Alıcı F.S., Kaatsız K. and Sucuoğlu H. “Bina Yapılarının Çok Modlu İtme Analizi için Genel Yük Vektörlerinin Pratik Uygulaması”, 3rd National Earthquake Engineering and Seismology Conference, İzmir, Turkey, 2015.

Kaatsız K., Alıcı F.S. and Sucuoğlu H. “Burulmalı Sistemler için Genel Yük Vektörleri ile Çok Modlu İtme Analizi”, 3rd National Earthquake Engineering and Seismology Conference, İzmir, Turkey, 2015.

Alıcı F.S., Kaatsız K. and Sucuoğlu H. “Practical Implementation of Generalized Pushover Analysis for Multimodal Pushover Analysis”, 2015 World Congress on Advances in Structural Engineering and Mechanics (ASEM15), Incheon, South Korea, 2015.

Kaatsız K., Alıcı F.S. and Sucuođlu H. “Generalized Force vectors for Analysis of Torsionally Coupled Systems”, 2015 World Congress on Advances in Structural Engineering and Mechanics (ASEM15), Incheon, South Korea, 2015.

Alıcı F.S., Kaatsız K. and Sucuođlu H. “Genel İtme Analizinin Pratik Uygulaması”, 2nd National Earthquake Engineering and Seismology Conference, Hatay, Turkey, 2013.

Alıcı F.S., Kaatsız K. and Sucuođlu H. “Practical Implementation of Generalized Pushover Analysis”, 15th World Conference on Earthquake Engineering, Lisbon, Portugal, 2012.

Alıcı F.S., Kaatsız K. and Sucuođlu H. “Multi Modal Pushover Analysis with Generalized Force Vectors (Generalized Pushover Analysis)”, 1st National Earthquake Engineering and Seismology Conference, Ankara, Turkey, 2011.

HOBBIES

Chess, Computer Technologies, Motor Sports